# Exotic Meson Photoproduction at GlueX
## – Search for the hybrid candidate $Y(2175)$

Dissertation

zur Erlangung des Doktorgrades
der Naturwissenschaften

vorgelegt beim Fachbereich Physik

der Johann Wolfgang Goethe-Universität
in Frankfurt am Main

von

Abdennacer Hamdi
aus Hammam Guergour, Algerien

Frankfurt am Main, 2020

D(30)

vom Fachbereich Physik der

Johann Wolfgang Goethe-Universität als Dissertation angenommen.

**Dekan:** Prof. Dr. Michael Lang

**Gutachter:** Prof. Dr. Klaus Peters

Prof. Dr. Joachim Stroth

Datum der Disputation: 19.11.2020

# Abstract

Understanding the hadron spectrum is one of the primary goals of non-perturbative QCD. Many predictions have experimentally been confirmed, others still remain under experimental investigation. Of particular interest is how gluonic excitations give rise to states with constituent glue. One class of such states are hybrid mesons that are predicted by theoretical models and Lattice QCD calculations. Searching for and understanding the nature of these states is a primary physics goal of the GlueX experiment at the CEBAF accelerator at Jefferson Lab. A search for a $J^{PC} = 1^{--}$ hybrid meson candidate, the $Y(2175)$, in $\phi(1020)\pi^+\pi^+$ and $\phi(1020)f_0(980)$ channels in photoproduction on a proton target has been conducted. A first measurement of non-resonant $\phi(1020)\pi^+\pi^+$ and $\phi(1020)f_0(980)$ total cross sections in photoproduction has been performed. An upper limit on the resonance production cross section for the $Y(2175) \to \phi(1020)\pi^+\pi^+$ and $Y(2175) \to \phi(1020)f_0(980)$ channels are estimated. Since the analysis essentially depends on the quality of the charged kaon identification, also an optimization of particle identification through an improvement of the energy loss estimation in the CDC by a truncated mean method has been investigated.

# kurzfassung

Das Verständnis des Hadronenspektrums ist eines der Hauptziele der nichtperturbativen QCD. Viele Vorhersagen sind experimentell bestätigt worden, andere werden noch experimentell untersucht. Von besonderem Interesse ist, wie gluonische Anregungen zu Zuständen mit konstitutivem Kleber führen. Eine Klasse solcher Zustände sind hybride Mesonen, die durch theoretische Modelle und Gitter-QCD-Berechnungen vorhergesagt werden. Die Suche nach und das Verständnis der Natur dieser Zustände ist ein primäres physikalisches Ziel des GlueX-Experiments am CEBAF-Beschleuniger am Jefferson Lab. In $\phi(1020)\pi^+\pi^+$ und $\phi(1020)f_0(980)$ wurde eine Suche nach einem $J^{PC} = 1^{--}$ Hybridmeson-Kandidaten, dem $Y(2175)$, in den Kanälen $\phi(1020)\pi^+\pi^+$ und $\phi(1020)f_0(980)$ in der Photoproduktion auf einem Protonentarget durchgeführt. Eine erste Messung der nichtresonanten Gesamtwirkungsquerschnitte $\phi(1020)\pi^+\pi^+$ und $\phi(1020)f_0(980)$ bei der Photoproduktion wurde durchgeführt. Es wurde eine Obergrenze für den Wirkungsquerschnitt für die Resonanzproduktion für die Kanäle $Y(2175) \to \phi(1020)\pi^+\pi^+$ und $Y(2175) \to \phi(1020)f_0(980)$ geschätzt. Da die Analyse im Wesentlichen von der Qualität der Identifikation des geladenen Kaons abhängt, wurde auch eine Optimierung der Teilchenidentifikation durch eine Verbesserung der Energieverlustschätzung in der CDC durch eine Methode des abgeschnittenen Mittelwertes untersucht.

# Table of Contents

# List of Tables

# List of Figures

# Chapter 1

# Introduction

Our understanding of the fundamental building blocks of matter has advanced greatly in the last few decades Ref. [1, 2, 3, 4, 5]. It is nearly half a century ago that Quantum Chromodynamics (QCD) was developed, a revolutionary idea that protons, neutrons and all other strongly interacting particles, the so-called hadrons, are made of quarks interacting with each other via the exchange of gluons. Over the years, this proposal has become firmly established even though we have not observed free quarks directly, due to the phenomenon of confinement [6]. Despite decades of research, we still lack a detailed quantitative understanding of the way QCD generates the spectrum of hadrons [7]. A wide experimental research campaign is conducted to shed new light on the hadron excitation spectrum and the dynamics of hadrons [8], helping to improve and test the theoretical models. A key player to study these properties is the GlueX experiment, which aims to discover and study the properties of the gluonic field contribution to the quantum numbers of the quark-antiquark bound system, the hybrid mesons [9]. This chapter gives an overview of QCD, and looks at hadron spectroscopy from a point of view of a simple quark model and beyond. In addition it gives an experimental status of a hybrid meson candidate, the Y(2175) state [10].

## 1.1 Quantum Chromo-Dynamics

QCD is the framework that describes one of the three fundamental forces in the Standard Model of particle physics, the strong force. It acts on the quarks and gluons. Quarks are spin 1/2 particles, with six different flavors: up ($u$), down ($d$), strange ($s$), charm ($c$), bottom ($b$) and top ($t$). Apart from electric charge, they also carry a color charge: red, blue, or green, and each quark has an associated antiquark of the same mass and opposite color charge, anti-red, anti-blue, and anti-green. Gluons are spin-1 particles, appearing in eight different color-anticolor configurations. The dynamics of the strong interaction between quarks and gluons are contained in the QCD Lagrangian defined in Eq. 1.1

$$\mathcal{L}_{\mathcal{QCD}} = \sum_{flavors} \bar{q}_A (i\gamma^\mu D_\mu - m)_{AB} q_B - \frac{1}{4} F^A_{\alpha\beta} F_A^{\alpha\beta} \ , \tag{1.1}$$

where $q_A$ ($\bar{q}_A$) are the quark (antiquark) fields with color indices $A$, and $F_A$ are nonlinear terms in the field strength, that give rise to three- and four-gluon vertices in the theory so that gluons couple to themselves in addition to interacting with quarks as shown in Fig. 1.1.

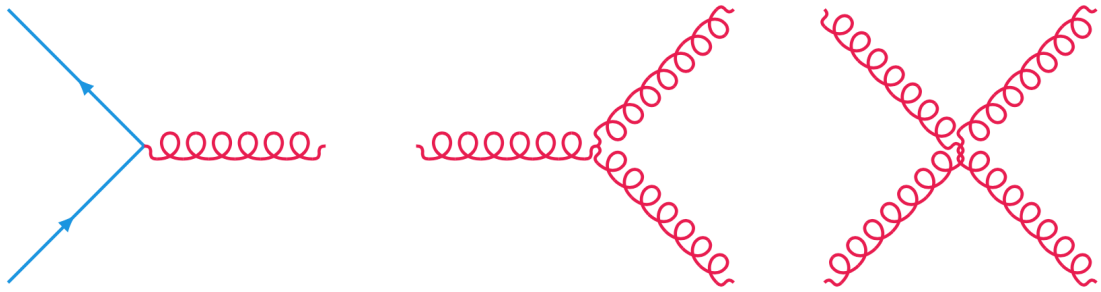

Figure 1.1: Interactions in QCD at the tree level. In the case of strong interaction, there are three fundamental vertices, representing particle creation or annihilation. The straight and curly lines represent the quarks (antiquarks) and gluon fields, respectively. The strength of the interaction between the particle and the force carrier at that vertex is called the coupling constant. These representations are called Feynman diagrams.

However, due to the gluon self-coupling, the vacuum will also be filled with virtual gluon pairs. Since gluons carry color charge, it turns out that the effective color charge becomes larger with larger distance. Whereas, in contrast, this anti-screening effect causes the strong coupling to become small at short distance (large momentum transfer). This leads the quarks inside hadrons to behave more or less as free particles, becoming evident when probed at large enough energies. This property of the strong interaction is called asymptotic freedom. Asymptotic freedom allows us to apply perturbation theory, resulting in quantitative predictions for hard scattering cross sections in hadronic interactions. On the other hand, at increasing distance, the coupling becomes so strong that it is impossible to isolate a single quark from a hadron. In other words, free quarks have never been observed, as a result of a long distance confining property of the strong QCD force, where all quarks hadronize (become part of a hadron). Only the top quark instead decays before it has time to hadronize. Therefore all observable strongly bound states are color singlets, conventionally appearing as formations of quark-antiquark pairs (carrying color and anticolor) called mesons, or groups of three quarks (carrying all three colors) called baryons. This mechanism is called confinement. The running of the strong coupling constant $\alpha_s$ as a function of the energy scale is shown in Fig. 1.2.

This self-interaction between gluons makes the QCD lagrangian nonlinear and very difficult to solve. Nevertheless in some special cases, approximate solutions can be found using some QCD-inspired models and by numerical calculations on a lattice (LQCD) [11]. LQCD is the only non-perturbative method based uniquely on the first principles of QCD. In LQCD, spacetime is discretized onto a four dimensional lattice grid. Quarks are placed on the grid points spaced by a distance, and Gluons lie on the links between these points, while quark masses and strong coupling constant are inputs to the model. The QCD continuum is reached,

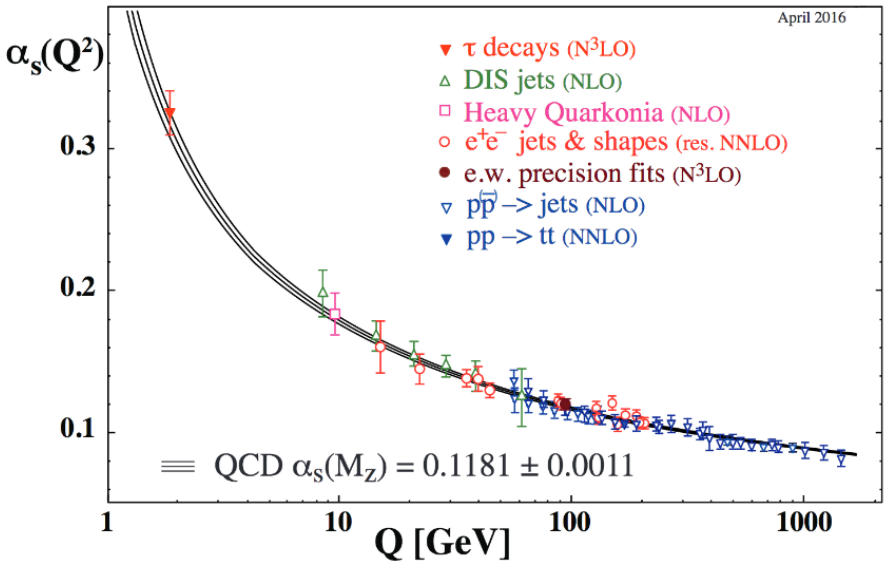


Figure 1.2: Summary of measurements of the strong coupling constant, $\alpha_s$, as a function of the energy scale, $Q$, from experimental data which agree closely with QCD predictions. The respective degree of QCD perturbation theory used in the extraction of $\alpha_s$ is indicated in brackets (NLO: next-to-leading order; NNLO: next-to-next-to leading order). Reproduced from Ref. [8].

when the lattice spacing goes to zero. In order to have a sufficiently fine granular lattice spacing, small realistic masses and a sufficiently large box size, one needs a massive amount of computing power, being the limiting factor for such numerical calculations. For QCD with realistic choices of the lattice spacing, volume and the quark masses, this is a serious computational challenge. To circumvent this problem, most numerical computations in LQCD have been realized in the quenched approximation, by ignoring all fermion loops. This introduces systematic errors, particularly for light quarks, due to the inverse proportionality between the effect of the fermion loop and the mass. QCD also suggests existence of new forms of hadronic matter with excited gluonic degrees of freedom, known as glueballs and hybrids [8]. Recent development in computational techniques and power have led to LQCD, making predictions of the mass and quantum numbers of the meson spectrum shown in Fig. 1.3.

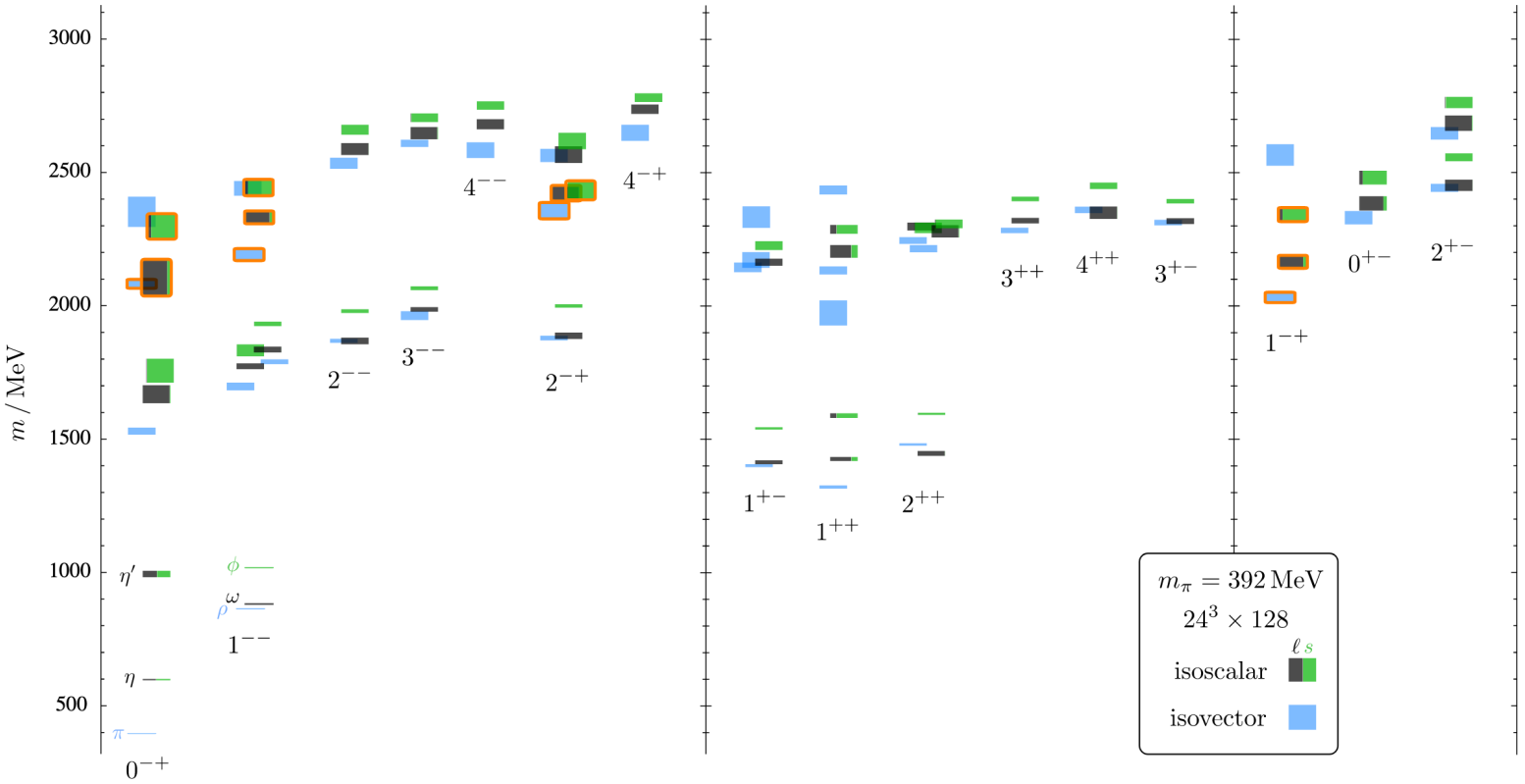


Figure 1.3: Spectrum of light mesons predicted using Lattice QCD. The height of the boxes indicates the errors in mass and states highlighted in orange correspond to the lightest hybrid mesons [11].

## 1.2 Mesons in the Constituent Quark Model and Beyond

In the quark model, mesons ($q\bar{q}$) are bound states of a quark ($q$) and an antiquark ($\bar{q}$), with $q$ and $\bar{q}$ being of the same or different quark flavors. Mesons are classified into $J^{PC}$ multiplets based on total angular momentum $J = L \oplus S$, orbital angular momentum $L$ between the quarks, parity $P = (-1)^{L+1}$, which specify the symmetry of the wave function under reflection through a point in space, and charge conjugation $C = (-1)^{L+S}$ that transforms a particle into its antiparticle. Following the SU(3) flavor symmetry, there are nine possible $q\bar{q}$ combinations containing the light $u$, $d$, and $s$ quarks, grouped into an octet and a singlet of light quark mesons defined in Eq. 1.2:

$$3 \otimes \bar{3} = 8 \oplus 1 \ . \tag{1.2}$$

The ground state ($L = 0$) nonets of mesons with spin 0 (pseudoscalar) and spin 1 (vector) are shown in diagrams Fig. 1.4a and Fig. 1.4b, respectively.

An exact symmetry under SU(3) would imply that the $u$, $d$ and $s$ quarks were mass degenerate. The SU(3) flavor symmetry is not an exact symmetry [5], due to the heavier $s$ quark mass of order 150 MeV/c$^2$ with respect to $u$ and $d$ quarks. Nevertheless, the SU(3) can still be considered as an approximate flavor symmetry, since this mass difference is very small on the hadronic mass scale of $\sim$ 1 GeV, and it still describes fairly well the observed pattern of hadron spectrum.

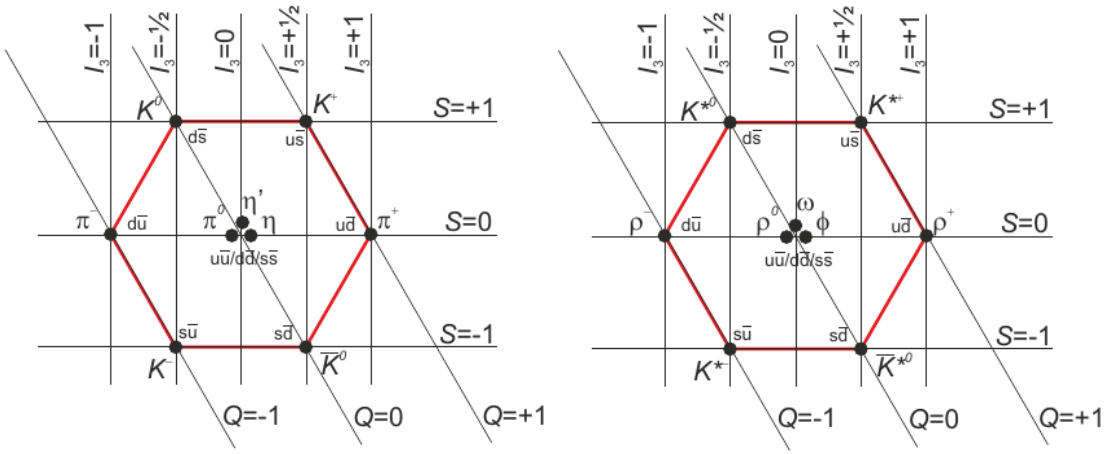


(a) (b)

Figure 1.4: Diagrams of light meson ground state nonets for pseudoscalars (a) and vectors (b), classified by the strong isospin $I_3$ and strangeness $S$ quantum numbers.

The lowest lying states of mesons built in the quark model are shown in Tab. 1.1. The above quantum numbers are repeated for the radial excitations, labelled with the radial number $n = 1, 2,$ *etc.*

Table 1.1: The light meson spectrum with the quantum numbers, reproduced from [8].

| $L$ | $S$ | $J$ | $n$ | $I=1$ | $I=1/2$ | $I=0$ | $I=0$ | $J^{PC}$ | $n^{2S+1}L_J$ |
|---|---|---|---|---|---|---|---|---|---|
| 0 | 0 | 0 | 1 | $\pi$ | K | $\eta$ | $\eta'(958)$ | $0^{-+}$ | $1^1S_0$ |
| 0 | 1 | 1 | 1 | $\rho(770)$ | $K^\star(892)$ | $\phi(1020)$ | $\omega(782)$ | $1^{--}$ | $1^3S_1$ |
| 0 | 0 | 0 | 2 | $\pi(1370)$ | $K(1460)$ | $\eta(1440)$ | $\eta(1295)$ | $0^{-+}$ | $2^1S_0$ |
| 0 | 1 | 1 | 2 | $\rho(1450)$ | $K^\star(1410)$ | $\phi(1680)$ | $\omega(1420)$ | $1^{--}$ | $2^3S_1$ |
| 1 | 0 | 1 | 1 | $b_1(1235)$ | $K_{1B}$ | $h_1(1380)$ | $h_1(1170)$ | $1^{+-}$ | $1^1P_1$ |
| 1 | 1 | 0 | 1 | $a_0(1450)$ | $K_0^\star(1430)$ | $f_0(1710)$ | $f_0(1370)$ | $0^{++}$ | $1^3P_0$ |
| 1 | 1 | 1 | 1 | $a_1(1260)$ | $K_{1A}$ | $f_1(1420)$ | $f_1(1285)$ | $1^{++}$ | $1^3P_1$ |
| 1 | 1 | 2 | 1 | $a_2(1320)$ | $K_2^\star(1430)$ | $f_2(1525)$ | $f_2(1270)$ | $2^{++}$ | $1^3P_2$ |
| 2 | 0 | 2 | 1 | $\pi_2(1670)$ | $K_2(1770)$ | $\eta_2(1870)$ | $\eta_2(1645)$ | $2^{-+}$ | $1^1D_2$ |
| 2 | 1 | 1 | 1 | $\rho(1700)$ | $K^\star(1680)$ | $\phi(2175)$ | $\omega(1650)$ | $1^{--}$ | $1^3D_1$ |
| 2 | 1 | 2 | 1 | $\rho_2(1940)$ | $K_2(1820)$ | | $\omega_2(1975)$ | $2^{--}$ | $1^3D_2$ |
| 2 | 1 | 3 | 1 | $\rho_3(1690)$ | $K_3^\star(1780)$ | $\phi_3(1850)$ | $\omega_3(1670)$ | $3^{--}$ | $1^3D_3$ |

From Tab. 1.1, we can see that some $J^{PC}$ quantum numbers are absent from the

list of the multiplets. For instance, a state with the quantum numbers $J^{PC} = 1^{-+}$, cannot be generated by a quark-antiquark state based on the rules specified above for $P$ and $C$. Therefore, it is called *(spin-)exotic*. Although, QCD allows any kind of color-neutral configurations, additional colorless states other than $q\bar{q}$ or $qqq$, are called exotic hadrons.

### 1.2.1 Multiquarks

Multiquark mesons are color-singlet state objects consisting of more than two or three (anti-)quarks, like, *tetraquarks* that are formed by a color-octet diquark and a color-octet anti-diquark bound by gluon exchanges (Fig. 1.5a), or *molecules*, which are configurations that include two color-singlet $q\bar{q}$ pairs bound by long-range meson exchanges (Fig. 1.5b). Another form is named *hadroquarkonium*, which is a compact, colorless quarkonium core, surrounded by a light quark cloud sticking together thanks to the QCD analogue of the van der Waals force (Fig. 1.5c). Several candidates for multiquark states exist, an extensively debated states are the $f_0(980)$ and $a_0(980)$, which were discussed to be a compact $q\bar{q}q\bar{q}$ object or an extended $K\bar{K}$ molecule. There are also speculations that the $Y(2175)$ may be a tetraquark candidate.

### 1.2.2 Glueballs

Due to the gluons self-interaction, color-singlet states composed entirely of multiple gluonic excitations without any valence quarks are possible, the so-called glueballs (Fig. 1.5d). Some of the supernumerary isoscalar $f_0$ states not fitting into the corresponding nonet are discussed to have a significant fraction of glueball nature. The lightest predicted glueballs have quantum numbers $J^{PC} = 0^{++}$ and $2^{++}$. Lattice calculations predict for the $0^{++}$ ground state a mass around 1600 – 1700 MeV, while the first excited $2^{++}$ state is predicted to have a mass of about 2300

MeV. Hence, the low-mass glueballs lie in the same mass region as ordinary isoscalar $q\bar{q}$ states.

### 1.2.3 Hybrids

QCD predicts also additional configurations, in which an excited gluonic field may contribute to the quantum numbers of the quarks in the meson, termed hybrids (Fig. 1.5e).

Arising from the gluonic contribution to the spin-parity $J^{PC}$ of the hybrid states, this quantum number is not anymore subject to the limitations holding for quark-antiquark systems. Such states are called spin-exotic hybrid mesons. In case of experimental evidence of a state with a 'forbidden' $J^{PC} = 0^{+-}$, $1^{-+}$ and $2^{+-}$ would prove unambiguously the existence of exotic (non-$q\bar{q}$) mesons [12]. The second case is all the states with $J^{PC}$ quantum numbers similar to the $q\bar{q}$, including the gluonic degrees of freedom, also named *cryptoexotic* mesons [9]. These latter should be observed as an overpopulation of states in the meson spectrum, and are hard to distinguish form the conventional $q\bar{q}$ states. The hybrid meson states with $J^{PC}$ quantum numbers are then formed:

$$J^{PC} = 0^{-+}, \mathbf{0^{+-}}, 1^{++}, 1^{--}, \mathbf{1^{-+}}, 1^{+-}, 2^{-+}, \mathbf{2^{+-}}, \dots \ . \tag{1.3}$$

Experiments have reported two different hybrid candidates with spin-exotic signature, $\pi_1(1400)$ and $\pi_1(1600)$, which couple separately to $\eta\pi$ and $\eta\prime\pi$. While the $\pi_1(1600)$ is close to the expectation for a hybrid, The $\pi_1(1400)$ candidate is not compatible with recent Lattice QCD estimates for hybrid states, which predicts that the lightest hybrid with exotic quantum numbers lies in the mass 1.7 - 1.9 GeV. For the $1^{--}$ Hybrid meson candidates, we find the $Y(2175)$, $Y(4260)$ and $\Upsilon(10860)$. The details of all these exotic mesons measurements mentioned above

are described in Ref [8]. The $Y(2175)$ meson is a strong candidate for a $1^{--}$ hybrid state [10], which will be the focus of this thesis. The experimental status and the search for this state in photoproduction are discussed in detail in Sec. 1.4 and Chap. 4, respectively.

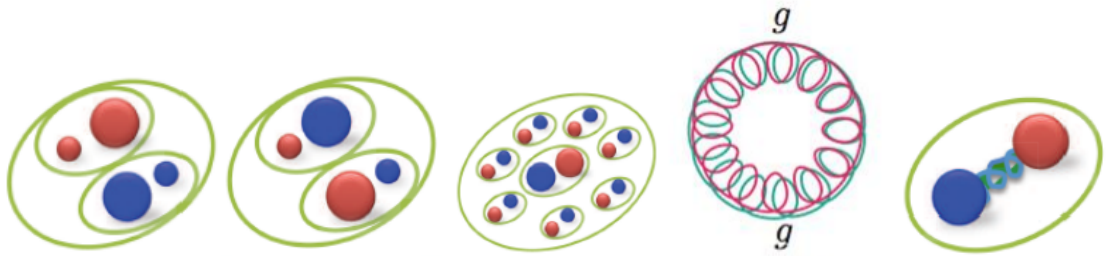


(a) (b) (c) (d) (e)

Figure 1.5: An illustration of the various exotic meson configurations. The blue and red colors represent the quarks and antiquarks, respectively, with the size of the spheres representing the light and heavy quarks.

## 1.3 Meson Production Mechanisms

Searching for and understanding the nature of the exotic states has been and still is a central goal of hadron spectroscopy. In recent years, many new and unexpected resonance-like signals have been observed in the heavy-quark sector [8]. Many of these so-called $XYZ$ states are candidates for exotic configurations of mesons. Similar studies are also performed in the light quark sector. Due to the short lifetime of light mesons, the resonances are broad, leading to states overlapping with each other, which hence made their detection challenging. In order to settle the fundamental question of the existence of states beyond the quark model and thus a strong confirmation of QCD or whether they are not realized in nature as expected, large data sets with high statistical precision are needed. The unambiguous identification of exotic states requires experiments with complementary production mechanisms and the analysis of different final states [13].

### 1.3.1 $e^+e^-$ Production

Since early $e^+e^-$ colliders were built, important measurements were conducted, including the discovery of the $J/\psi$ meson at SLAC. These colliders kept evolving to higher center-of-mass energies reaching $\sqrt{s} \sim 209$ GeV at the Large Electron Positron (LEP) collider. Along the way, the $e^+e^-$ colliders PETRA (at DESY) and PEP (at SLAC) saw the first three-jet events, which was the clear signature of a quark-antiquark pair accompanied by hard gluons. The presence of the gluon, the mediator of the strong interaction, had been discovered in 1979. Major discoveries also happened later on with the upcoming B-factories at KEK and SLAC, and at high-intensity colliders in Beijing, Cornell, Frascati and Novosibirsk. Experiments at the electron-positron colliders are particularly useful for studies of quarkonium physics and decays of open charm and bottom mesons.

The $e^+e^-$ annihilation process in the leading order is mediated by a single virtual photon with the quantum numbers $J^{PC} = 1^{--}$, with the possibility to produce hadrons via the Initial State Radiation (ISR) in the process $e^+e^- \to hadrons + n\gamma$. The photon $\gamma$ is emitted from one of the incoming particles, reducing the beam energy prior to the momentum transfer (Fig. 1.6). This technique allows to measure hadronic cross sections from threshold up to the maximum energy of the colliders running at fixed energy, which is a very fruitful source of data on meson spectroscopy. Varying the $e^{\pm}$ beam energy, experiments scan through the center of mass energy and trace out the resonance shape, modified by interferences with overlapping states. Large data continues to be acquired and analyzed at operating $e^+e^-$ storage ring facilities.

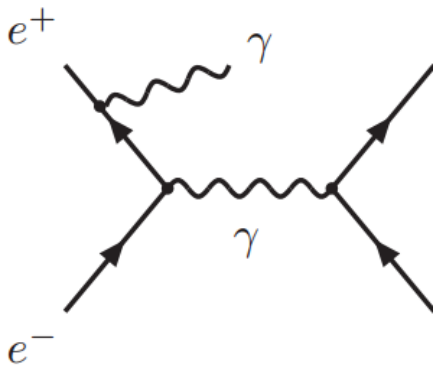


Figure 1.6: The tree level diagrams contributing to the leading order amplitude from initial state photon emission (ISR) in $e^+e^-$ collisions.

### 1.3.2 Hadronic Diffractive Production

Most of the data on light meson spectroscopy has come from pion beam on nuclear targets, where the beam particle is exchanging momentum and quantum numbers with a recoiling target nucleon and further moves forward. Meson-nucleon

scattering reactions at high energy are strongly forward peaked, in the direction of the incoming meson. Mostly, the diffractively produced meson state is moving forward, eventually decaying into more stable particles, and the baryon is recoiling under large angles. This mechanism is shown schematically in Fig. 1.7. The excited meson state $X$ has quantum numbers determined by the exchange, hence studying carefully the production mechanism for different reactions is important. Some examples of experiments using these techniques are: $K^- p \to Xp$ by the LASS collaboration, and $\pi^- p \to Xp$ by the COMPASS, E852 and VES experiments.

Diffractive reactions are characterized by the four-momentum exchange, $t = (p_{Beam} - p_X)^2 < 0$, with the typical cross section falling exponentially in $-t$, i.e. $e^{-bt}$ with the slope $b \sim 3$ - $8\ GeV^{-2}$. For example, in charge exchange reactions at small values of $-t$, one pion exchange (OPE) dominates and is fairly well understood. It provides access only to states with $P = (-1)^J$, the so called *natural* parity states. Other states such as $J^{PC} = 0^{-+}$ can be produced by neutral $J^{PC} = 0^{++}$ *Pomeron* exchange, or $\rho^+$ exchange but these are not as well understood. Often the analysis is performed independently for several ranges of $t$ in order to also investigate the nature of the production mechanism.

The generality of this production mechanism and the high statistics available result in several advantages, opening a large number of final states that can be studied, by comparing decay branches of these states, as well as searching for decay modes that were not previously accessible.

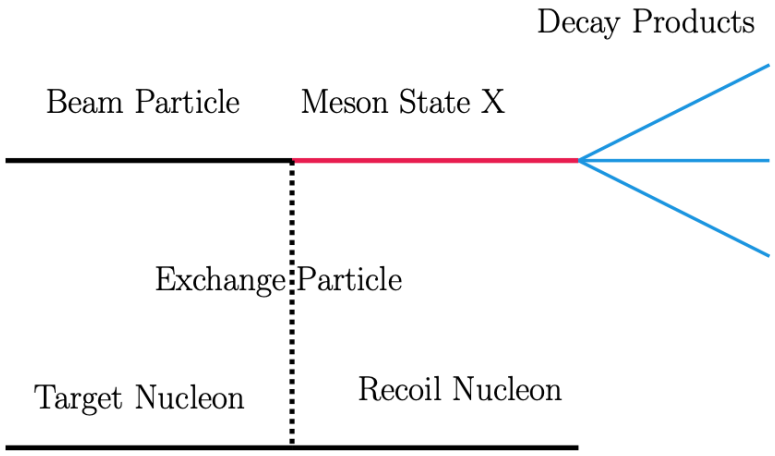


Figure 1.7: Schematic diagram of a hadronic diffractive production process. Momentum is exchanged through an off-mass-shell particle.

### 1.3.3 Photoproduction

A very promising mechanism to produce hybrid meson states is through a diffractive scattering with a photon beam. Since the photon according to the vector dominance model (VDM) [14] can be considered as a virtual $q\bar{q}$ with aligned spins ($S = 1$) (Fig. 1.8a), in contrast to diffractive hadroproduction with pions or kaons ($S$=0) (Fig. 1.8b), it is expected that the exotic quantum number states will be enhanced in photoproduction. In $\pi$ produced interactions, spin-flip and quantum-number exchange mechanisms are expected to suppress the production of hadrons with spin-exotic quantum numbers. [12, 13].

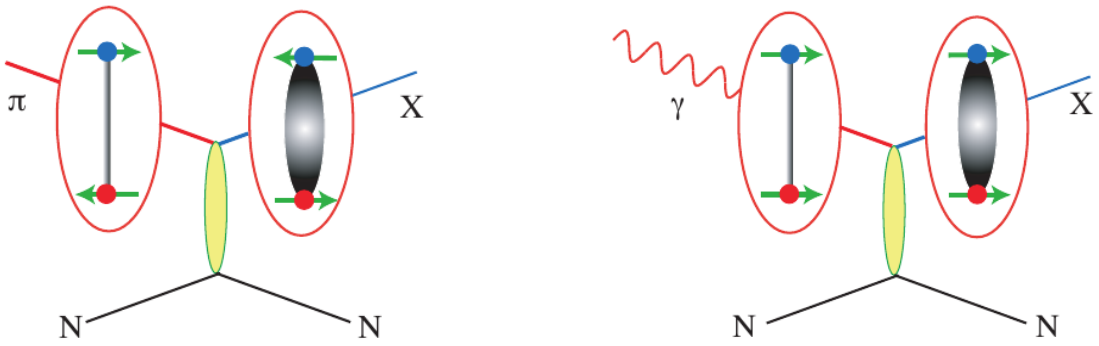


(a) (b)

Figure 1.8: (a) With a $\pi$ probe the incoming quarks have $L = 0$ and $S = 0$. According to the flux-tube model the resulting scattered hybrid mesons have no exotic quantum numbers. (b) With a photon probe the incoming photon behaves according to VDM as a meson, with $L = 0$ and $S = 1$. When the flux-tube is excited, hybrid mesons with exotic quantum numbers are possible.

Similar to hadron diffractive reactions, the photoproduction is also characterized by the four-momentum exchange, $-t$. Understanding the mechanisms of meson photoproduction is critical for disentangling the $J^{PC}$ quantum numbers of the observed states in the exotic hybrid mesons search. Theoretical models predict that the beam asymmetry, $\Sigma$ extracted from fitting the yield asymmetry in Fig. 1.9 with the Eq. 1.4, is sensitive to the relative contributions from vector $1^-$ (*e.g.* $\rho^0/\omega$) and axial-vector $1^+$ (*e.g.* $b_1^0/h_1$) exchanges in $\pi^0$ and $\eta$ photoproduction, see also [15]. The yield asymmetry is defined as

$$\frac{Y_\perp - F_R Y_\parallel}{Y_\perp + F_R Y_\parallel} = \frac{(P_\perp + P_\parallel)\Sigma \cos 2\phi_p}{2 + (P_\perp - P_\parallel)\Sigma \cos 2\phi_p}, \tag{1.4}$$

where $F_R = N_\perp/N_\parallel$ is the ratio of the integrated photon flux between the perpendicular and parallel beam polarizations. $P_\perp$ and $P_\parallel$ are the magnitudes of the two beam polarization and $\phi_p$ is the azimuthal angle of the production plane defined by the final-state proton. The yield asymmetry ratio between the two polarization configurations cancels out the $\phi$-dependent detector acceptance effects.

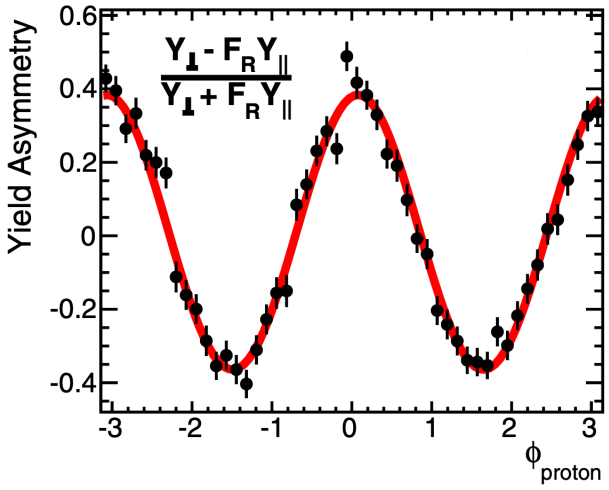


Figure 1.9: The yield asymmetry as measured for the process $\gamma p \to p\pi^0$ as a function of the azimuthal angle of the proton, shown together with the fit of Eq. 1.4 to extract $\Sigma$.

The GlueX experiment has studied two exclusive reactions, $\gamma p \to p\pi^0$ and $\gamma p \to p\eta$ with $\pi^0/\eta \to \gamma\gamma$. After extracting the $-t$ beam asymmetry dependence, the GlueX data strongly suggests the dominance of vector meson exchange at the beam energy range 8.4 - 9 GeV (Fig. 1.10).

Diffractive photoproduction has further advantages. The vector dominance model allows non-OZI suppressed excitation of heavy quark states, such as $s\bar{s}$ and $c\bar{c}$, through production of the associated vector meson(s), the $\phi$ and $J/\psi$ states, respectively. Unfortunately, there is only very limited data available from photoproduction. This is mainly due to the lack of high quality, high intensity photon beams, as well as associated experimental apparatus. This situation is starting to change since the GlueX experiment, using a high energy photon beam of $\sim$ 12 GeV, started taking data in 2016.

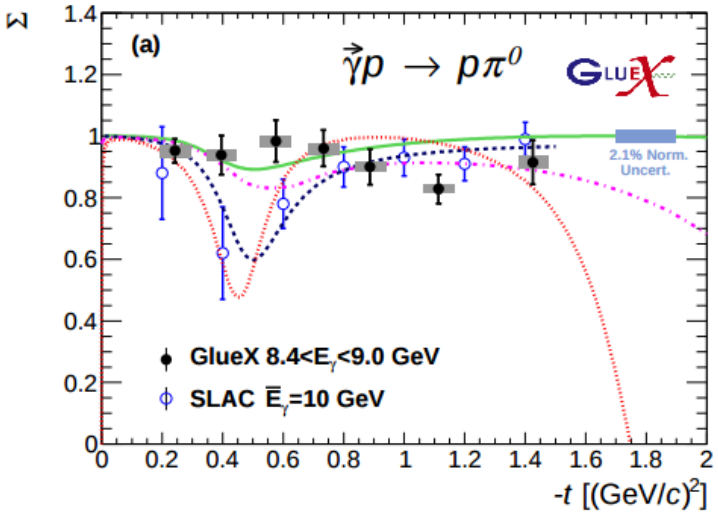


(a)

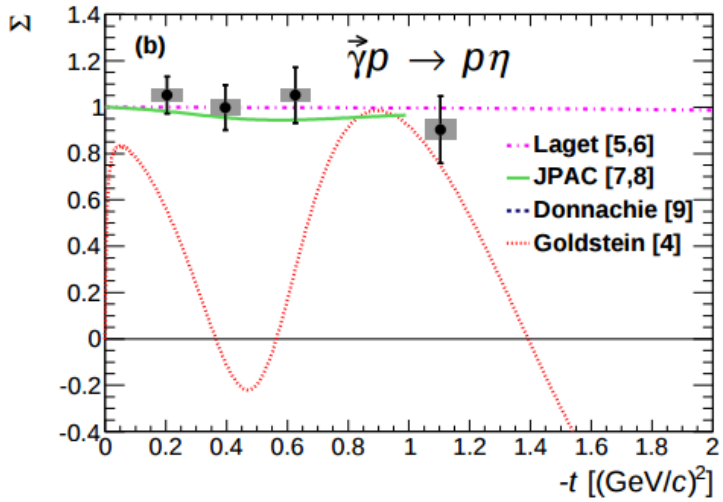


(b)

Figure 1.10: Beam asymmetry $\Sigma$ for (a) $\gamma p \rightarrow p\pi^0$ and (b) $\gamma p \rightarrow p\eta$ (black filled circles) determined in bins of momentum transfer $(-t)$. Uncorrelated systematic errors are indicated by the height of gray bars, whereas the combined statistical and systematic uncertainties are given by the black error bars. The previous SLAC results from data collected at $\overline{E}_\gamma = 10$ GeV (blue open circles) are also shown along with various Regge theory calculations (see ref. [15] and references therein).

Table 1.2: Some of particle physics experiments that have contributed significantly to the knowledge of exotic hadron spectrum. Future experiments that are expected to have a major impact are also included.

| Experiments | Laboratory | Accelerator facility | Production process | Centre-of-mass energy (GeV) | Operational period |
|---|---|---|---|---|---|
| CDF/D0 | Fermilab, USA | Tevatron | $p\bar{p} \to b\bar{b}X$ | 2000 | 1987 - 2011 |
| BaBar | SLAC, USA | PEP-II | $e^+e^- \to \Upsilon(4S) \to B\bar{B}$ | 10.6 | 1999 - 2008 |
| Belle | KEK, Japan | KEKB | $e^+e^- \to \Upsilon(4S) \to B\bar{B}$ | 10.6 | 1999 - 2010 |
| CLEO-c | Cornell, USA | CESR | $e^+e^- \to c\bar{c}$ | 3.7 - 4.2 | 2003 - 2008 |
| BESIII | IHEP, China | BEPC | $e^+e^- \to c\bar{c}$ | 3 - 4.6 | 2008 - ongoing |
| LHCb | CERN, Switzerland | LHC | $pp \to b\bar{b}X$ | 7000 - 13000 | 2010 - ongoing |
| Belle II | KEK, Japan | Super-KEKB | $e^+e^- \to \Upsilon(4S) \to B\bar{B}$ | 10.6 | 2018 - 2025 |
| GlueX | JLab, USA | CEBAF | $\gamma p \to c\bar{c}X$ | 3.5 | 2016 - ongoing |
| PANDA | GSI, Germany | FAIR | $p\bar{p} \to c\bar{c}X$ | 2.2 - 5.5 | 2025 - |

## 1.4 Experimental status of the Y(2175)

The $Y(2175)$, also denoted as $\phi(2170)$ by the Particle Data Group (PDG) [8], was first observed in 2006 by the BaBar collaboration [16] in the $e^+e^- \to \phi(1020)f_0(980)$ process. Later the analysis was updated [17] with twice the integrated luminosity. By fitting the observed cross section for both $e^+e^- \to \phi\pi^+\pi^-$ (Fig. 1.11a) and $e^+e^- \to \phi f_0(980)$ (Fig. 1.11b), they confirmed the presence of the $Y(2175)$ in the data, as well as the presence of the $\phi(1680)$ resonance.

It was subsequently confirmed by the Belle collaboration [18] in both, the reactions $e^+e^- \to \phi(1020)\pi^+\pi^-$ (Fig. 1.12a) and $e^+e^- \to \phi f_0(980)$ (Fig. 1.12b). The analysis is based on a data sample of 673 fb$^{-1}$ collected on and below the $\Upsilon(4S)$ resonance. In order to obtain the parameters of $Y(2175)$ and $\phi(1680)$ resonances, a least squares fit is applied to the measured cross section distribution. An incoherent Breit-Wigner fit for the $Y(2175)$ and $\phi(1680)$ was performed, with an additional function centered near 2.4 GeV/c$^2$, where the statistical significance were $10\sigma$ for the first two resonances, and only $1.5\sigma$ for the structure around 2.4 GeV/c$^2$. The cross section were measured from threshold to $\sqrt{s} = 3$ GeV using initial-state radiation.

The $Y(2175)$ was also confirmed by the BESII [19] and BESIII [20], both in $J/\psi$ hadronic decays (Fig. 1.13), based on samples of 5.8 x $10^7$ and 2.25 x $10^8$ $J/\psi$ events, respectively. The fit yields 471$\pm$54 $Y(2175)$ events with a statistical significance of greater than $10\sigma$. The fit results show that the significance of the structure around 2.35 GeV/c$^2$ is only $3.8\sigma$. The resonance was recently also measured for the first time in $e^+e^- \to \eta Y(2175)$ process with BESIII [21]. The mass and width of the Y(2175) resonance, in different experiments, are summarized in Tab. 1.3.

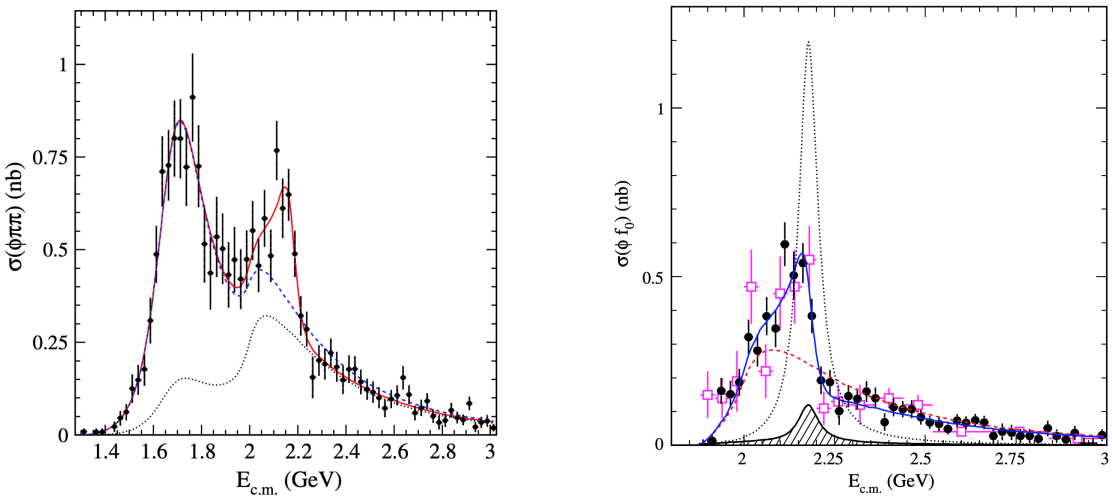


(a) (b)

Figure 1.11: (a) The fit to the $e^+e^- \to \phi\pi^+\pi^-$ cross section using the model described in Ref. [17], the entire contribution due to the $\phi(1680)$ is shown by the dashed curve. The dotted curve shows the contribution for only the $\phi f_0$ decay. (b) The $e^+e^- \to \phi f_0(980)$ cross section measured in the $K^+K^-\pi^+\pi^-$ (solid dots) and $K^+K^-\pi^0\pi^0$ (open squares) final states. The solid and dashed curve represents the result of $Y(2175)$ and $\phi(1680)$ resonance fits, respectively. The hatched area and dotted curve show the $Y(2175)$ contribution for two solutions described in Ref. [17].

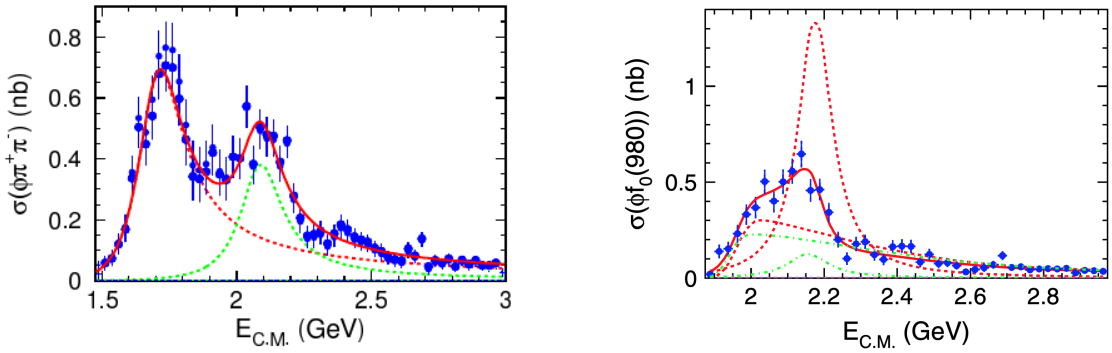


(a) (b)

Figure 1.12: (a) The fit to $e^+e^- \to \phi\pi^+\pi^-$ cross section with two incoherent Breit-Wigner functions, one for the $\phi(1680)$ (red dashed line) and the other for the $Y(2175)$ (green dashed line). (b) $e^+e^- \to \phi f_0(980)$ cross section with a single Breit-Wigner function that interferes with a nonresonant component. In (b), the dashed and dot-dashed curves are for the destructive and constructive interference solutions described in [18], respectively.

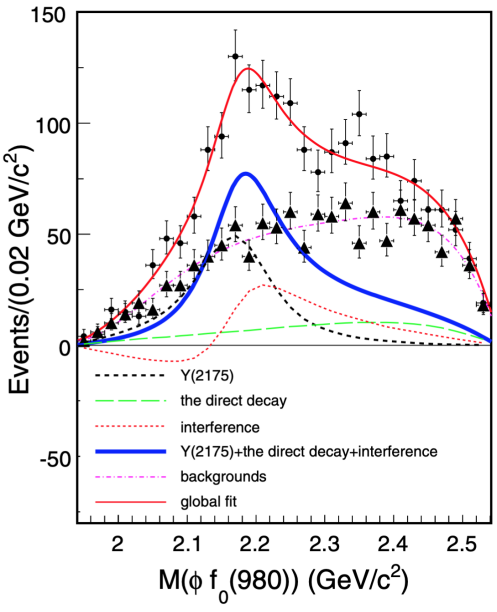


Figure 1.13: $\phi f_0(980)$ invariant mass spectrum, with an unbinned maximum likelihood fit. The circular and triangular dots show the distribution in the signal and background region, with the backgrounds estimated using sideband regions. The green dashed line represents the direct decay of $J/\psi \to \eta\phi f_0(980)$. Ref. [20].

Since it is produced in $e^+e^-$ annihilation, the quantum numbers are $J^{PC} = 1^{--}$. The observation of the $Y(2175)$ stimulated many theoretical interpretations of its nature. There are very few known meson resonances with $I = 0$ near this mass, and therefore it is likely not a standard meson but rather an exotic state. Since the similarity in production mechanism and decay patterns to the $Y(4260)$ in the charm sector and the $\Upsilon(10860)$ in the bottom sector, the $Y(2175)$ is discussed to be a candidate of a strangeonium hybrid ($s\bar{s}g$) [10], a tetraquark ($s\bar{s}s\bar{s}$) [22], a $\Lambda\bar{\Lambda}$ bound state [23], an excited $\phi$ [24], or an ordinary $\phi f_0(980)$ resonance produced by interactions between the final state particles [25]. The quark model predicts two conventional $s\bar{s}$ states near 2175 MeV/$c^2$, the $3^3S_1$ and $2^3D_1$ [26, 27], however, both of them are predicted to be significantly broader than the $Y(2175)$ [28, 29].

Despite all previous experimental and theoretical efforts, our knowledge of the $Y(2175)$ is still limited. This state has so far been observed only in direct $e^+e^-$

annihilation and in $J/\psi \to \eta Y(2175)$ decays. Nevertheless, the characteristic decay modes of the $Y(2175)$ as either a $s\bar{s}g$ or $s\bar{s}$ state are quite different [10, 12], which may be used to distinguish the hybrid from conventional quarkonium configurations. Decay modes and rates will be crucial to determine the nature of the $Y(2175)$. A first search for this state in photoproduction data has been performed for the first time in the GlueX experiment (Chap. 4).

Table 1.3: Mass and width of the $Y(2175)$ resonance in different experiments, reproduced from [16, 17, 18, 19, 20, 21]

| Experiments | Reactions | $Y(2175)$ mass ($\mathrm{GeV/c^2}$) | $Y(2175)$ width ($\mathrm{GeV/c^2}$) |
|---|---|---|---|
| BaBar | $e^+e^- \to \phi(1020)f_0(980)$ | $2.175 \pm 0.010 \pm 0.015$ | $0.058 \pm 0.016 \pm 0.020$ |
| | $e^+e^- \to \phi(1020)f_0(980)$ | $2.180 \pm 0.008 \pm 0.008$ | $0.077 \pm 0.015 \pm 0.010$ |
| | $e^+e^- \to \phi(1020)\pi^+\pi^-$ | $2.176 \pm 0.014 \pm 0.004$ | $0.090 \pm 0.022 \pm 0.010$ |
| Belle | $e^+e^- \to \phi(1020)f_0(980)$ | $2.163 \pm 0.032$ | $0.125 \pm 0.040$ |
| | $e^+e^- \to \phi(1020)\pi^+\pi^-$ | $2.079 \pm 0.013$ | $0.192 \pm 0.023$ |
| BESII/BESIII | $J/\psi \to \eta\phi f_0(980)$ | $2.186 \pm 0.010 \pm 0.006$ | $0.065 \pm 0.023 \pm 0.017$ |
| | $J/\psi \to \eta\phi\pi^+\pi^-$ | $2.200 \pm 0.006 \pm 0.005$ | $0.104 \pm 0.015 \pm 0.015$ |
| | $e^+e^- \to \eta Y(2175)$ | $2.135 \pm 0.008 \pm 0.009$ | $0.104 \pm 0.024 \pm 0.012$ |

# Chapter 2

# The GlueX Experiment

The GlueX experiment is installed at Jefferson Lab in Newport News, Virginia. The experiment is located at the end of the new beamline of the Continuous Electron Beam Accelerator Facility (CEBAF) (Fig. 2.1). At CEBAF, electron beam bunches are produced and accelerated by cryomodules containing superconducting radio frequency cavities. One pass corresponds to about a 2.2 GeV energy increase to the electron beam. The electron beam is extracted for three experimental halls (A,B and C), after 1-5 passes through the accelerator. The GlueX experimental hall, hall D, receives a 249.5 MHz electron beam at 5.5 passes in order to reach high enough energy to produce mesons of masses close to 3.5 GeV [30]. The 12 GeV electron beam is used to produce linearly polarized photons for the experimental hall D. These high energy photons will allow GlueX for accessing different kinematics to produce the lightest hybrid spectrum. An overview of the GlueX photon beamline and the detector is described in the following sections.

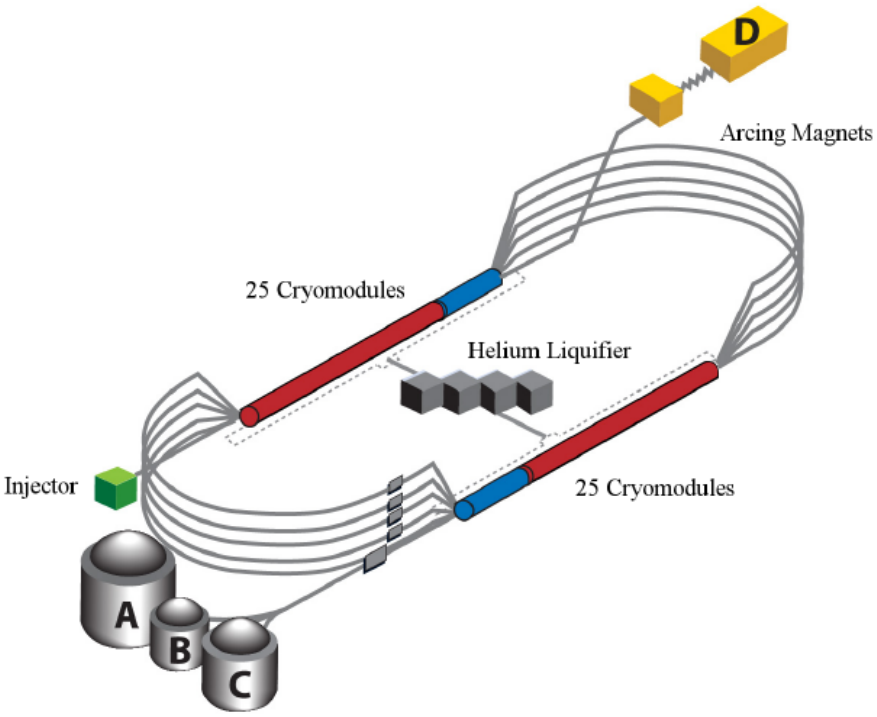


Figure 2.1: The Jefferson Lab CEBAF accelerator. The electron beam begins its first orbit at the injector. The linear accelerator, using the cryomodules, drive electrons to higher energies. The arcing magnets in both sides steer the electron beam from one straight section of the tunnel to the next for up to five orbits. In the middle the Helium liquifier provides liquid helium for ultra low temperature, during the superconducting operation. The beam is delivered to the 4 experimental halls A, B, C and D [30]

## 2.1 Photon Beamline

In the photon beamline, the linearly polarized photon beam is produced, that will be then impinged on the hydrogen target. Measuring the energy, polarization and the flux of the incident photon beam is performed by the beamline components. A schematic illustration of the beamline is shown in Fig. 2.2.

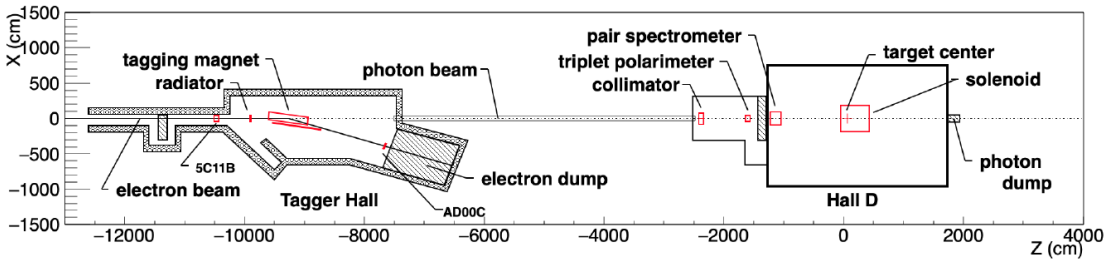


Figure 2.2: Schematic layout of the Hall D complex, showing the Tagger Hall, Hall D, and several of the key beamline devices. Also indicated are the locations of the 5C11B and AD00C beam position monitors [30].

### 2.1.1 Diamond Radiator and Collimator

The electron beam provided by the CEBAF accelerator is converted on a thin (50, 58, 47, and 17 $\mu$m) diamond radiator to a 9 GeV photon beam via the Bremsstrahlung process. Conservation of four-momenta in the reaction allows the determination of the outgoing photon energy. The lattice structure of the diamond radiator was aligned with the beam to produce coherent bremsstrahlung, with the coherent photon intensity peaking in specific energy ranges where the photons are linearly polarized relative to the crystal axis in the diamond as shown in Fig. 2.3. Two different diamond orientations are used, with the electric field vector parallel (PARA) or perpendicular (PERP) to the floor of the experimental hall. This process produces also secondary enhancements in the radiated photon energy spectrum due to integer multiples of the reciprocal lattice vector.

For a 12 GeV electron beam, the GlueX experiment reaches more than 40%

intensity of the emitted coherent photons, with a maximum at about 9 GeV photon energy. The emitted bremsstrahlung radiation is found within the characteristic angle $\theta_{CB}$ defined as

$$\theta_{CB} = \frac{m_e}{E} \ , \tag{2.1}$$

where $m_e$ is the electron rest mass, and $E$ are the energy of the incident electron.

The photons traverse a 75 m long lead-block collimator, with two diameters configurations: 3.4 mm or 5.0 mm diameter, to suppress the wider angular spread of the incoherent photons, and keep the coherent component of the beam. The effect of collimation on the beam energy spectrum is shown in Fig. 2.3.

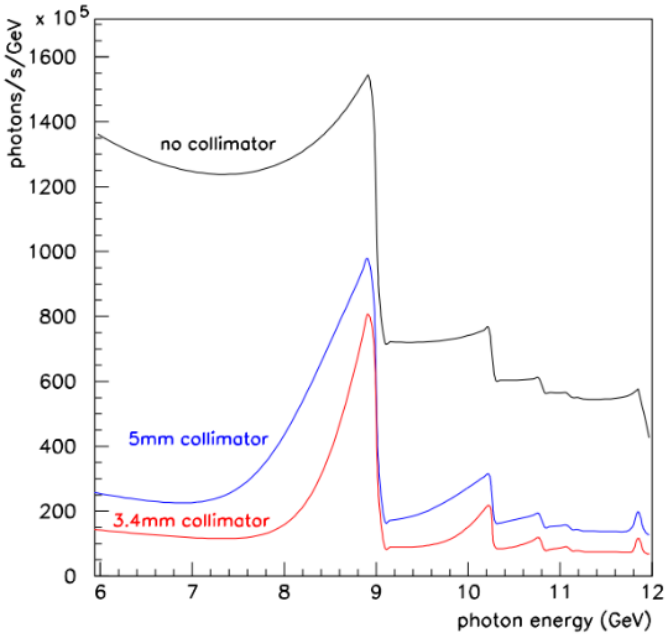


Figure 2.3: The beam profile in different collimation conditions. Three configurations are shown, with the absence of the collimator (black), with a 5 mm diameter collimator (blue), and a 3.4 mm collimator (red). The peak between 8.4 - 9 GeV is representing the coherent photon beam component [31].

### 2.1.2 Photon Tagging System

After hitting the radiator, the scattered electron is bent by a dipole magnet of 1.8 T into the tagging spectrometer. The radius of the curvature and thus the deflection angle determines the recoiled electron momentum, and by knowing the initial energy of the incident electron beam, this allows to measure the photon energies. The tagging spectrometer is composed of two scintillation detectors, The Tagger Hodoscope (TAGH) and Tagger Microscope (TAGM) that measures the energy of photons in the incoherent and coherent energy region, respectively. The electrons not interacting with the diamond are stopped in the beam dump. More information on the photon tagger can be found in Ref. [31].

### 2.1.3 Photon Beam Flux and Polarization

A thin beryllium (Be) foil is placed downstream of the collimator, where the beam photons interact with the electrons of the Be atom through the reaction $\gamma e^- \rightarrow e^- e^+ e^-$.

The beam flux is measured by detection of the produced $e^+e^-$ pairs in the Pair Spectrometer (PS). It consists of a dipole magnet to separate the electron pair paths into two scintillating detector arms, and a hodoscope to measure the energy and time using Silicon Photo Multipliers (SiPM).

The beam polarization is determined by the Triplet Polarimeter (TPOL), using the recoiled electron ($e^-$) from the Be foil. It is a silicon strip detector consisting of 32 azimuthal components and 24 concentric circles. The angular distribution of the recoil electron ($\phi_{e^-}$) provides information about the beam polarization. For linearly polarized photons, the cross-section ($\sigma$) is defined as

$$\sigma = \sigma_0[1 + P\Sigma \cos(2\phi_{e^-})] \ , \tag{2.2}$$

where $P$ is the linear polarization, $\sigma_0$ is the unpolarized cross section, and $\Sigma$ is the analyzing power [32].

The photon spectrum and its polarization with a 12 GeV electron beam are shown in Fig. 2.4, where $\sim 40\%$ of linear polarization after collimation is expected in the energy range of 8.4 – 9 GeV.

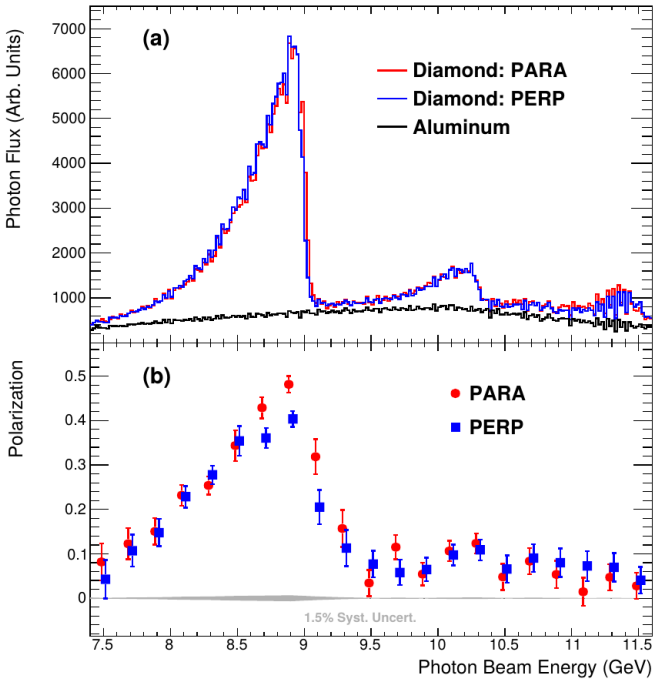


Figure 2.4: (a) Photon beam intensity versus energy as measured by the pair spectrometer (not corrected for instrumental acceptance). (b) Photon beam polarization as a function of beam energy, as measured by the triplet polarimeter, with data points offset horizontally by $\pm 0.015$ GeV for clarity [31].

## 2.2 The GlueX Spectrometer

The linearly polarized photon beam is then delivered to the main spectrometer. The GlueX spectrometer is a multilayer detector, composed of a barrel shaped central spectrometer and further sub-detectors in forward direction. Surrounding a 30 cm long liquid hydrogen target in the center, with a decreasing diameter from 2.42

upstream to 1.56 cm downstream, a set of devices for particle identification with the Start Counter (SC) and Time of Flight (TOF) detectors are installed. Another set of devices for charged particle tracking is performed by the Central (CDC) and Forward (FDC) Drift Chambers. And finally, the detection of neutral particles is performed by the barrel (BCAL) and the forward (FCAL) calorimeters. For charged particle momenta measurements, a solenoid magnet is installed, delivering a magnetic field of 2.08 T. A schematic overview of the detector elements is shown in Fig. 2.5

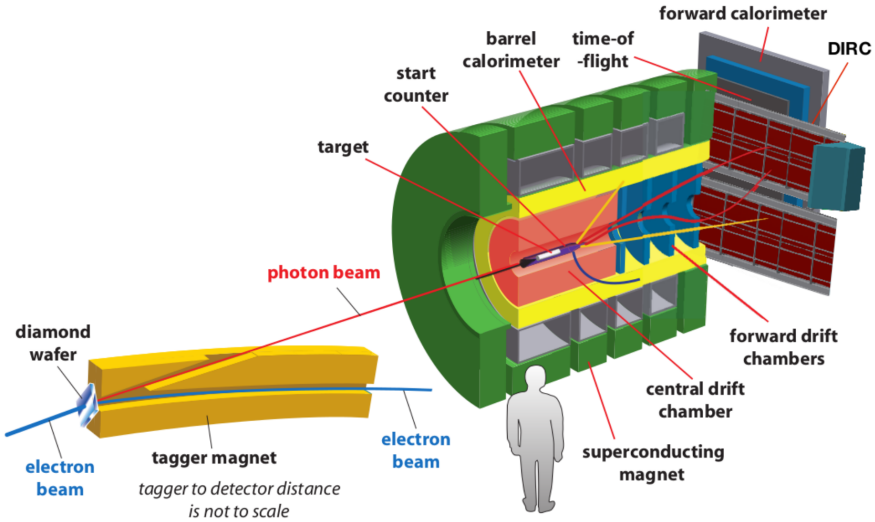


Figure 2.5: The GlueX beamline and spectrometer. The photon beam extracted from the tagger hall, left side of the figure, is imping on the iquid hydrogen ($LH_2$) target in the center of the main detector. A 2.08 T solenoidal magnet surrounds the tracking system (green) [31].

## 2.2.1 Particle Identification Detectors

### 2.2.1.1 Start Counter (SC)

The SC covers about 90% of $4\pi$ solid angle coverage for particles originating from the center of the target. It provides timing information about the outgoing particles,

to select the beam bunch of the photon that initiated the event. The detector with a timing resolution of roughly 300 ps [31] is made of segmented plastic scintillator that is bent to taper around the target cell (see Fig. 2.6).

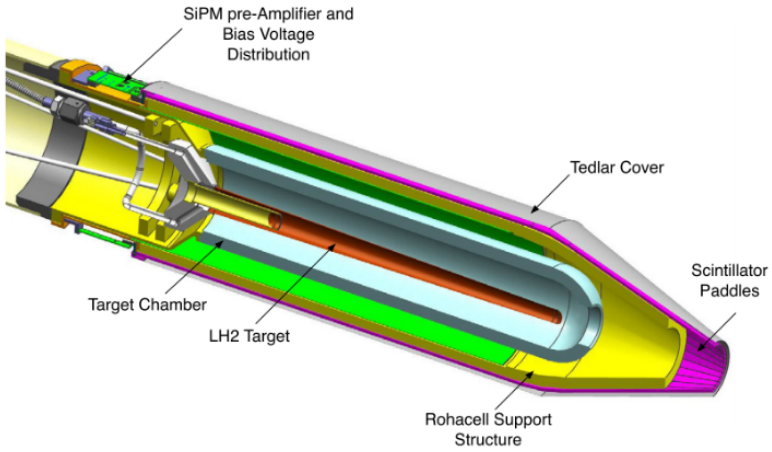


Figure 2.6: The GlueX Start Counter mounted to the liquid H2 target assembly. The beam goes from left to right down the central axis. [31].

#### 2.2.1.2 Time of flight Detector (TOF)

The TOF detector is a wall of scintillators located about 5.5 m downstream from the target and covers an angular region from 0.6° to 13° in polar angle [31], shown in Fig. 2.7a. By combining the path length of the particle from tracking with the timing information from the TOF, we can compare the measured with the expected flight time for a given particle species. The measured velocity $\beta$ as function of momentum for different particles based on their mass hypothesis is shown in Fig. 2.7b.

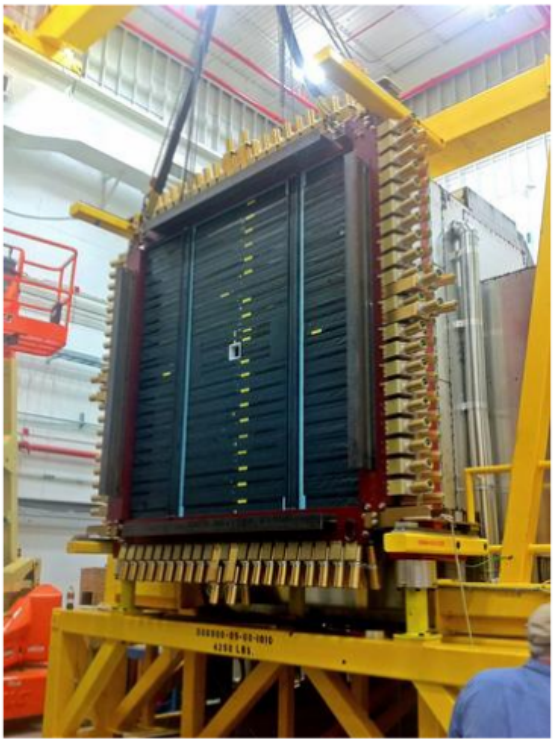

(a)

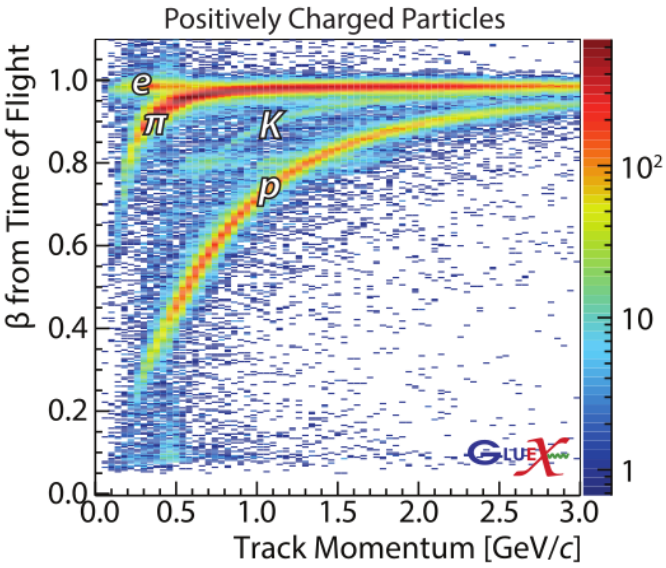


(b)

Figure 2.7: TOF detector mounted in Hall D (a), and velocity ($\beta$) versus particle momenta for positively charged particles to demonstrate the PID capability in the TOF detector (b) [33].

### 2.2.2 Charged Particle Tracking

Charged particle tracking is achieved by two detectors contained inside the solenoid magnet, the Central Drift Chamber (CDC) and Forward Drift Chamber (FDC) detectors, as shown in Fig. 2.8. These measure the position and time information of charged particles to reconstruct their trajectories and momenta. Both are ionization gas chambers filled with a mixture of $CO_2$ and Ar gas. They are comprised of high voltage electrodes that create an electric field between a cathode and anode, the CDC uses straw tubes and the FDC uses planes of wire packages to serve as their anodes. The charged particles will ionize the gas and the free electrons drift towards the anode at a well-defined velocity. The high field gradient near the anode causes an amplification of the initial free electron, this avalanche of electrons is converted to an electrical signal and used to detect the position of the charged particle track. Layers with skewed straw tubes (stereo layers) in the CDC allow the reconstruction of z-coordinates. Using the radius of the track curvature in the magnetic field, the particles momentum is determined. The CDC provides polar angle coverage from 6° to 128° and the FDC covers angles up to 20° [31]. The CDC also plays an important role in PID by measuring the energy lost per unit length using flash ADCs, (cf. Sec. 3).

(a)

(b)

Figure 2.8: (a) The Central Drift Chamber layer of stereo straw tubes is shown, surrounding a layer of straw tubes at the opposite stereo angle. Part of the carbon fiber endplate, two temporary tension rods and some of the 12 permanent support rods linking the two endplates can also be seen. (b) The Forward Drift Chamber, consisting of 24 disk-shaped planar drift chambers of 1m diameter. They are grouped into four packages.

### 2.2.3 Calorimeters

Neutral particles energy and direction are measured by the Barrel Calorimeter (BCAL) and Forward Calorimeter (FCAL), shown in Fig. 2.9. The particles interacting with these detectors create electromagnetic showers which are used to reconstruct the reaction decay products. The BCAL is a lead-scintillating fiber calorimeter with readout on both the upstream and downstream ends. The FCAL is located 6 m downstream of the target and consists of 2800 lead-glass blocks oriented such that the FCAL acceptance is azimuthal symmetric for polar angles less than 11.5°. The BCAL covers polar angles spanning from 11° to 126° [31]. The GlueX detector readout and data acquisition is triggered by a significant energy deposit in the BCAL or FCAL.

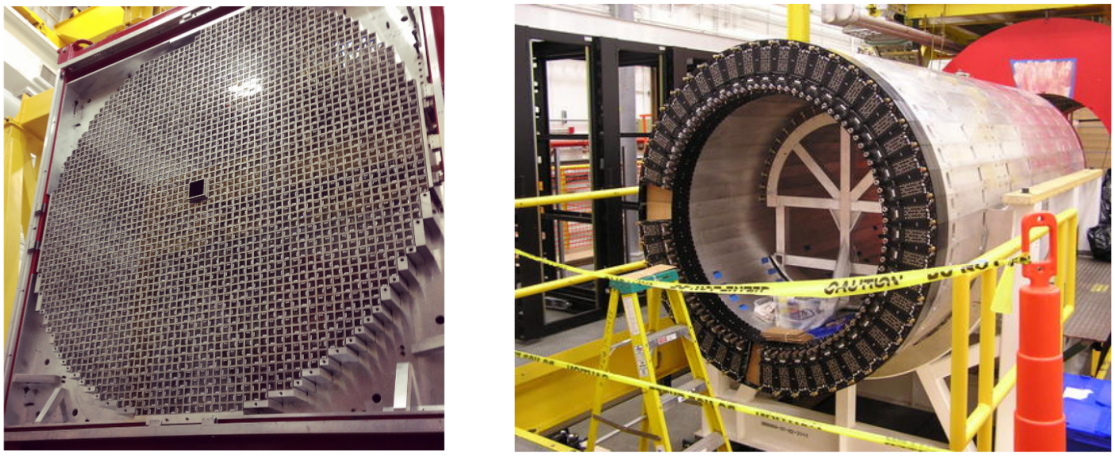

(a) (b)

Figure 2.9: (a) Picture of the FCAL detector showing the individual lead-glass blocks. (b) View of the upstream face of the BCAL before being inserted into the solenoid bore.

# Chapter 3

# Estimation of the Mean Energy Loss in the Central Drift Chamber

Reconstructing the final state charged and neutral particles is essential for the physics analysis. Searching for hybrid candidates, *e.g.* the $Y(2175)$, in the exclusive reaction $\gamma p \to Y(2175)p \to K^+K^-\pi^+\pi^-p$ demands a good kaon, pion and proton separation. One of the crucial GlueX spectrometer subsystems for providing the PID information is the CDC detector, through the measurement of the energy loss, $dE/dx$.

## 3.1 Particle Identification in the CDC

The Central Drift chamber is a gas detector for the detection of charged particles. It is filled with a mixture of 50% argon and 50% $CO_2$ at atmospheric pressure. Charged particle traversing the gas volume ionizes some of the gas atoms, so that electron-ion pairs are produced. Due to the electric field introduced by the high voltage applied to the straw cathode and anode, the electrons and ions in the gas start drifting in opposite directions: the negatively charged electrons to the anode

and the positively charged ions to the cathode. For the anode, a thin wire of 20 $\mu$m diameter is used in order to obtain a high electric field nearby. Electrons reaching the vicinity of the anode wire after the drift time are accelerated by this strong field so that they can ionize other gas molecules. The electrons form an avalanche that can be measured as a negative electric pulse. The sum of the integrated charges for each hit in the wires can be used to calculate the energy loss [34].

In the CDC, the energy loss is obtained from the height of the first peak of each pulse instead of its integral, as this was found to give better resolution. The energy loss and track length in the straws traversed are used finally to compute the $dE/dx$ [35]. The $dE/dx$ in the material is described by the Bethe-Bloch formula [36] defined as

$$-\frac{dE}{dx} = 2\pi N_A r_e^2 m_e c^2 \rho \frac{Z}{A}\frac{z^2}{\beta^2}\left[\ln\left(\frac{2m_e\gamma^2\beta^2 W_{max}}{I^2}\right) - 2\beta^2 - \delta - 2\frac{C}{Z}\right] , \qquad (3.1)$$

with $2\pi N_A r_e^2 m_e c^2 = 0.1535$ MeV cm$^2$/g. The terms in this expression are defined in Tab. 3.1. The maximum energy transfer that can be provided in a head-on collision from the incident particle of mass $M$ to an atomic electron in the medium, $W_{max}$, can be computed as:

$$W_{max} = \frac{2m_e c^2 \eta}{1 + 2s\sqrt{1+\eta^2} + s^2} , \qquad (3.2)$$

Table 3.1: Terms in the Bethe-Bloch formula for the energy loss.

| | |
|---|---|
| $r_e$ : classical electron radius ($2.817\times10^{-13}$ cm) | $\rho$ : density of medium |
| $m_e$ : electron mass | $ze$ : charge of incident particle |
| $N_A$ : Avogadro's number | $\beta$ : $v/c$ of incident particle |
| $I$ : Mean excitation potential | $\gamma$ : $1/\sqrt{1-\beta^2}$ |
| $Z$ : Atomic number of medium | $\delta$ : density correction |
| $A$ : Atomic weight of medium | $C$ : shell correction |
| | $W_{max}$ : max. energy transfer |

where $s = m_e/M$ and $\eta = \beta\gamma$.

It is a universal function of $\beta\gamma$ for all particle masses. The energy loss as function of momentum shows a characteristic decrease with $1/\beta^2$. It reaches a minimum around $\beta\gamma = 4$, and continues with a logarithmic rise, the so-called "relativistic rise region", until it saturates in form of the "Fermi plateau". In practice two corrections are made to this expression to account for density effects ($\delta$) and shell corrections ($C$). The notion of density effects, which are important as the energy of the incident charged particle increases, arises from the fact that the electric field of a charged particle tends to polarize the atoms along its path. Due to this effect, electrons far from the path of the particle are shielded from the full electric field intensity. The notion of shell effects, which are most important at low energies, is needed to account for effects that arise when the velocity of the incident particle is comparable to the orbital velocity of the atomic electrons in the medium. In this case the atomic electrons cannot be assumed as stationary, and capture process is possible.

The momentum of the charged particles emerging from the interaction point are reconstructed in the CDC, which is defined by

$$p_{total} \;=\; p_{\perp}\ \sec\,(\lambda) \quad \text{and} \quad \lambda \;=\; \frac{\pi}{2} - \theta, \tag{3.3}$$

where the transverse momentum, $p_{\perp}$, and the angle, $\lambda$, are measured from the curvature of the tracks in the magnetic field, with the polar angle, $\theta$, covering a range between 29° and 123° in the CDC.

By measuring the momentum of the particle as well as the energy loss, the mass of the particle can be determined. The Figure 3.1 shows the energy loss as a function of reconstructed particle momentum. We see two distinguished bands, one for protons at higher $dE/dx$ values, and one horizontal band for other lighter particles, namely pions and kaons. These two bands are clearly separated in Fig. 3.1

for momenta of up to $\sim 1$ GeV/$c$. At higher momenta the bands overlap and the PID capabilities for hadrons get rather limited.

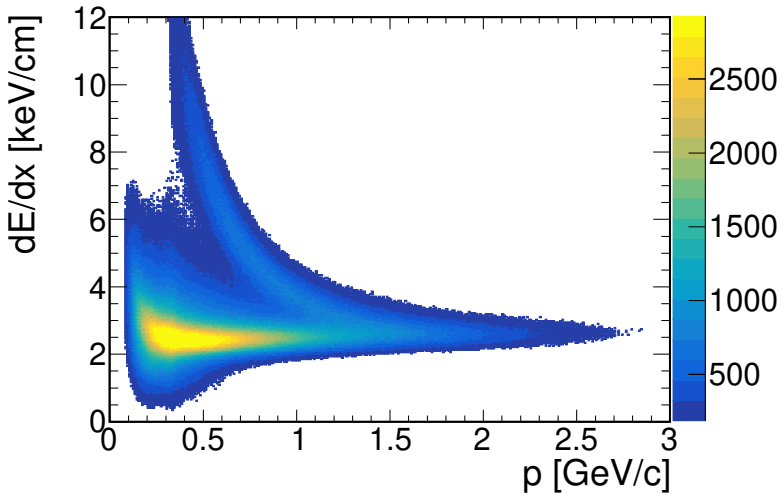


Figure 3.1: Measured specific energy loss $dE/dx$ of reconstructed tracks as a function of particle momentum as obtained from experimental data in the CDC . At values of $p \leq 1$ GeV/$c$, the protons are in the upper $dE/dx$ band, and the kaons and pions are at the lower $dE/dx$ band.

## 3.2 Mean Energy Loss Estimation

A precise and accurate $dE/dx$ measurement is crucial for the quality of particle identification. A study of the $\gamma p \to \pi^+\pi^- p$ phase space shows that the recoiled proton mostly hits the CDC, see Fig. 3.2. Measuring the $dE/dx$ will be the main information to identify these recoiled proton.

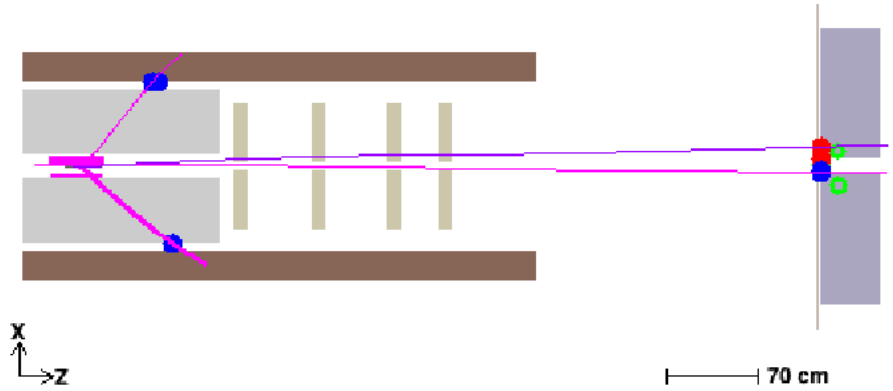


Figure 3.2: Top view of the detector, with reconstructed tracks of final state particles in the $\gamma p \rightarrow \pi^+\pi^- p$ reaction. The tracks at higher polar angles are protons that hit mostly the CDC, while the pions are moving forward, ending at the TOF wall.

Before the mean energy loss of a track can be calculated, many corrections were required due to the variations in temperature, atmospheric pressure and other environmental conditions which will affect the $dE/dx$ measurements. Furthermore, the geometric structure of the CDC, the charge-particle trajectory and non-uniformity of the electric and magnetic fields, also cause biases in the $dE/dx$ measurement [37, 38, 39].

The $dE/dx$ distribution compiled from all straw tube signals along the trajectory has a long tail that follows a Landau-like distribution. The high energy losses are mainly caused by particles having direct collisions with electrons [36]. Due to the high-energy tail, the arithmetic mean moves towards higher energy loss, and the mean energy loss value is higher than the most probable value see (Fig. 3.3, left). This makes it necessary to measure many samples along each track in order to determine the mean energy loss with sufficient accuracy. Reduction of the fluctuations of the energy loss can also be achieved by using thicker samples, for example by increasing the gas pressure. However, increasing the thickness results in a lower Fermi plateau and a different slope of the relativistic rise, and therefore

resulting in a smaller differences in the energy loss of different particle species.

For a better estimate of the mean Energy loss, we use the truncated mean method, due to its simplicity and very good accuracy [37, 38, 39]. This method rejects a certain percentage of the lowest and highest $dE/dx$ measurements from the calculation of the mean energy loss. Fig. 3.3 shows the energy loss for one track in the CDC. We observe that the $dE/dx$ distribution before the truncation (Fig. 3.3a) has a mean of about 6 keV/cm, while the most probable $dE/dx$ value is around 4 keV/cm. After a 40% truncation at high $dE/dx$ (Fig. 3.3b), a better mean energy loss accuracy is achieved.

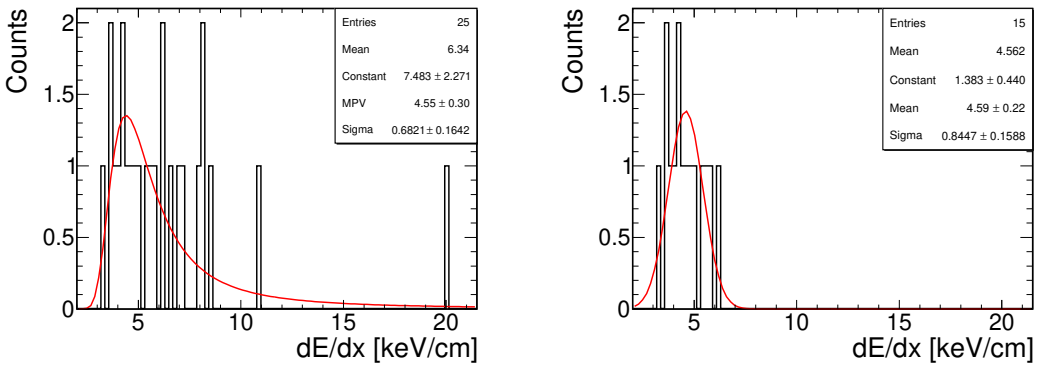


(a) (b)

Figure 3.3: Energy loss for one track in the CDC before truncation (left) and after 40% truncation (right). An average of 25 hits per track is seen before the truncation. The $dE/dx$ distributions are fitted with Landau and Gauss functions, before and after truncation, respectively.

The fraction of hits to be rejected is determined by optimizing three figures of merit: the mean energy loss resolution of both the proton and pions, the separation power between particle species, defined in Eq. 3.4, and the mis-identification fraction (mis-PID) between particles, given by Eq. 3.8. These figures of merit assuming gaussian distributions are illustrated in Fig. 3.4. The mis-PID is the fraction of

hits, from all the reconstructed tracks, in the $dE/dx$ distribution, that is mixed between particle species. The latter was introduced due to the fact that in some cases, where even with a good resolution and separation power, there is still a significant overlap between the tails of the energy loss distributions of the different particles.

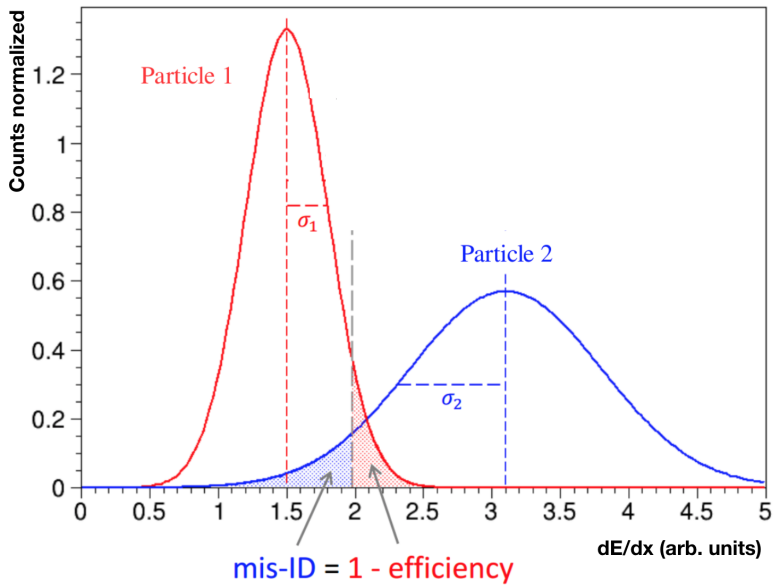


Figure 3.4: Illustration of the three figure of merits: $dE/dx$ resolution of particle 1 ($\sigma_1$) and particle 2 ($\sigma_2$), separation power ($Z$), and finally the mis-PID, as shown by the blue hatched area.

$$Z = \frac{\text{separation}}{\text{resolution}} = \frac{dE/dx_1 - dE/dx_2}{\sqrt{\sigma_1^2 + \sigma_2^2}} \ , \tag{3.4}$$

where $Z$ is separation power, $(dE/dx)_{1(2)}$ and $\sigma_{1(2)}$ are the average energy loss and the resolution for particles 1(2), respectively. In general case, where the $dE/dx$ is randomly distributed (non-gauss), the separation power could be defined as

$$Z = 2\Phi^{-1}(1 - \text{mis-PID}) \ , \tag{3.5}$$

where the Gaussian quantile $\Phi^{-1}$ is defined by

$$\Phi(x) = \frac{1}{\sqrt{2\pi}} \int_{-\infty}^{x} e^{-x^2/2}\, dx, \tag{3.6}$$

Considering two $dE/dx$ Likelihood PDF's, $L_1(dE/dx)$ and $L_2(dE/dx)$, of the particle 1 and 2, respectively, the reconstruction efficiency, $\epsilon$, of particle 1 is defined as

$$\epsilon = \int_{-\infty}^{x_0} L_1(dE/dx)\, dx\ , \tag{3.7}$$

where $x_0$ is the $dE/dx$ value at which we can reach a certain level of reconstruction efficiency of particle 1, as shown in Fig. 3.4, represented by the dashed vertical line around $\sim 2$. The corresponding mis-PID is then the fraction of particle 2 that is incorrectly identified as the particle 1, due to the overlap of the two particle species $dE/dx$ distributions in this region.

$$\text{mis-PID} = \int_{-\infty}^{x_0} L_2(dE/dx)\, dx\ . \tag{3.8}$$

## 3.3 Simulation

In the following section, we will focus on optimizing the truncation based on the mis-PID, and finally compare to the other two figure of merits mentioned in Sec. 3.2.

We generate protons and pions isotropically across the phase-space in momentum and polar angle of the tracks, and we measure their energy loss in the CDC. The $dE/dx$ distributions for the proton and pions versus the track momentum are shown in Fig. 3.5a and Fig. 3.5b, respectively.

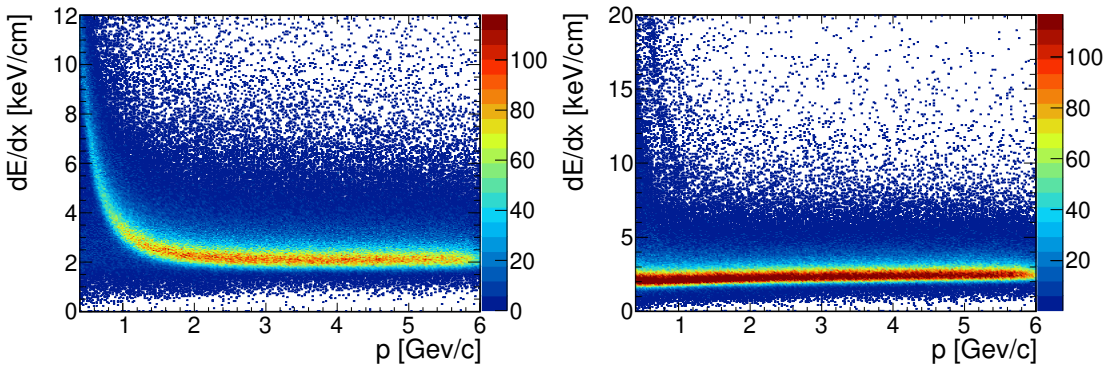


(a) (b)

Figure 3.5: Energy loss versus track momentum for protons (left) and pions (right). At low momentum, the protons, due to their heavier mass compared to pions, have a stronger $dE/dx$ loss. We also notice a stronger relativistic rise at high momentum for pions.

The average energy loss for reconstructed tracks of protons and pions are shown in Fig. 3.6, where the mis-PID fractions of pions for proton identification is shown in yellow. The latter is defined as the fraction of pions wrongly identified as protons, requiring a reconstruction efficiency of proton of 95%. In the following we will search for the optimal combinations of low and high tail truncation of the average $dE/dx$ distributions, that delivers the smallest mis-PID.

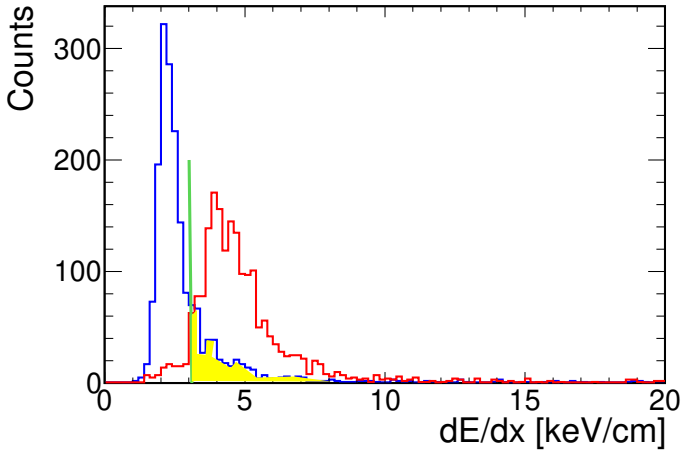


Figure 3.6: Average energy loss in the CDC for protons (Red) and Pions (blue), mis-PID (yellow). The vertical green line represent the minimum $dE/dx$ value at which the reconstruction efficiency of protons selected above is 95%.

Computing mis-PID fractions for different truncation combinations in every momentum and polar angle bin, seen in Fig. 3.7, shows that the mis-PID is largely reduced in the case of removing only 20% hits at high $dE/dx$, without removing hits at low $dE/dx$ (0%,20%). For tracks with momentum $\sim$ 5 GeV/$c$ and polar angle of $\sim$ 100°, the mis-PID is smaller in (0%,20%) than (20%,20%) truncation combination. After extracting the best truncation combination for every momentum and polar angle, a similar conclusion was deduced from studying the correlation between these optimal truncations between protons and pions, as seen in Fig. 3.8, showing a concentration of the optimal combination of truncations between 20% - 40% on the high tail of $dE/dx$. We also notice that a truncation on one side of the $dE/dx$ distribution, at high $dE/dx$ values, is efficient to deliver an optimal mean energy loss.

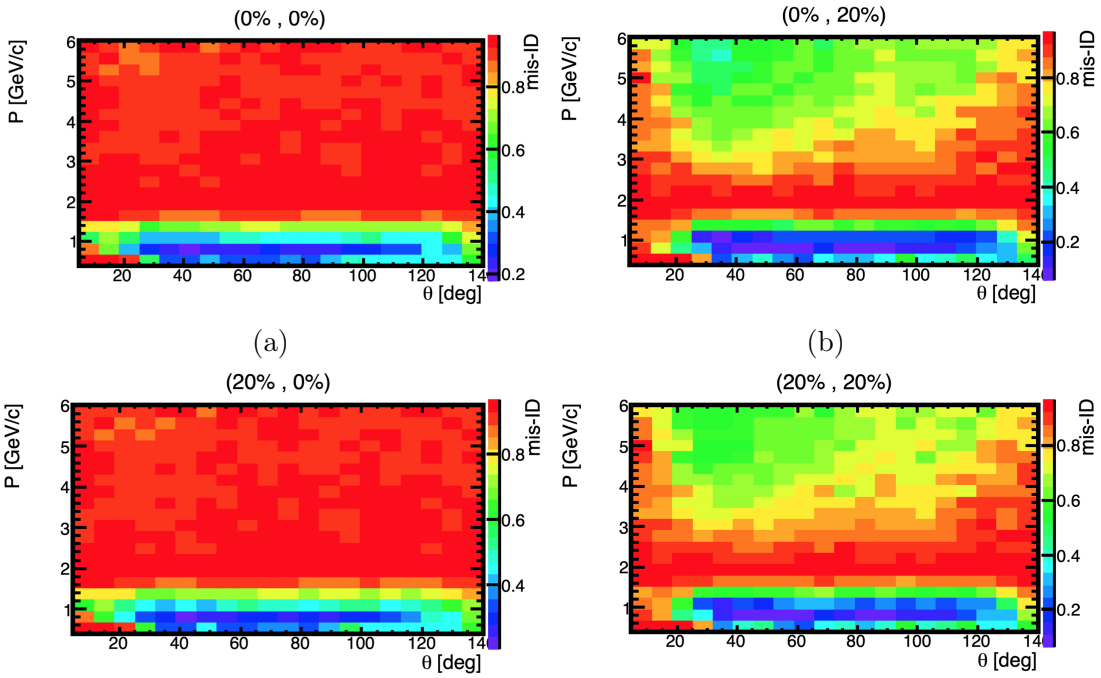


Figure 3.7: Mis-PID fraction in bins of momentum and polar angle between protons and pions. The different truncations, (a) (0%,0%), (b) (0%,20%), (c) (20%,0%), and (d) (20%,20%) are shown, with variations of mis-PID from low (blue) to high (red), in different momentum and polar angle bins.

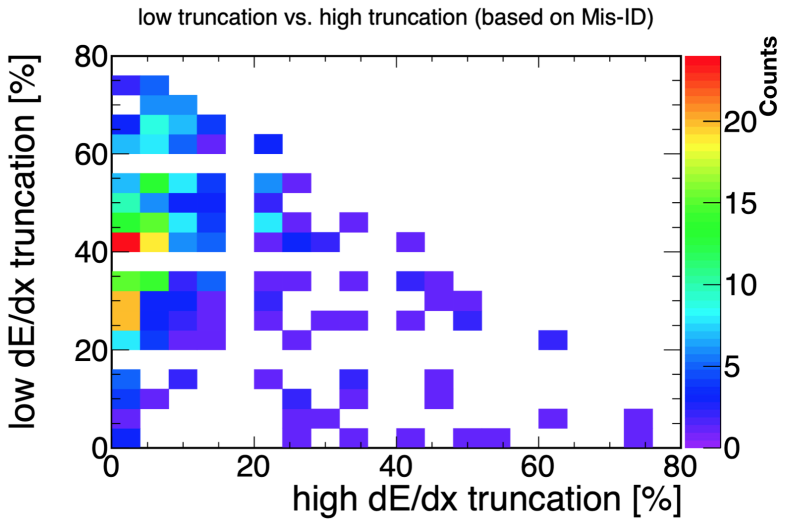


Figure 3.8: Performance of combinations of low and high tail truncation for proton identification vs. pions. An optimal truncation (low $dE/dx$, high $dE/dx$) is realized between (0%,20%) - (0%,40%), where the concentration of the optimal truncation is represented between the red and orange region.

Averaging over all the polar angles of the tracks, which are represented by the error bars in Fig. 3.9, we show the mis-PID (Fig. 3.9a), separation power (Fig. 3.9b), $dE/dx$ resolution of protons (Fig. 3.9c) and of pions (Fig. 3.9d), in track momentum dependence for four different truncation combinations. In the three different figures of merit, the optimal truncation is $\sim$ 20% on the high tail of energy loss distribution. The increase in mis-ID and the corresponding dip in separation power as a function of the track momentum, could be understood as an effect of the good distinction between the proton and pion $dE/dx$ bands, at low and high momenta, while in the region of intermediate momenta between 1 - 2 GeV/$c$ the intersection of the two bands leads to a weak and high separation power and mis-PID, respectively.

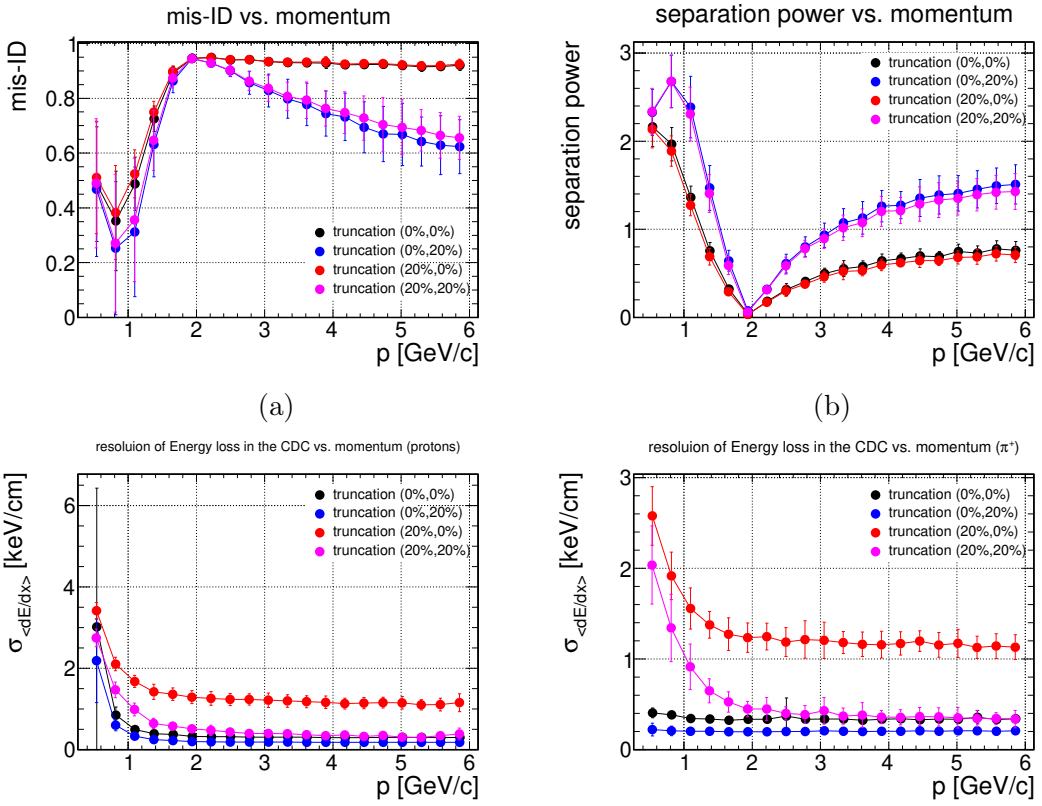


Figure 3.9: mis-PID (a), separation power (b), $dE/dx$ resolution of protons (c) and of pions (d) versus the track momentum, the error bars are the averaging over polar angles. Four truncations: (0%,0%), (0%,20%),(20%,0%), (20%,20%), are shown.

## 3.4 Summary and outlook

For a better mean energy loss estimation in the CDC, an optimal truncation of the average $dE/dx$ for pions and protons has been studied. By optimizing the mis-PID, separation power and the $dE/dx$ resolution, an optimal truncation is achieved, and estimated to be between 20% and 40% on the high $dE/dx$ values. A more conservative truncation of 20% is now included in the GlueX reconstruction software.

Next to the double truncated mean method used in this study, various other methods exist to calculate the average $dE/dx$ of a track, that treat the Landau tail differently. The most commonly used method is the truncated mean method in one side only of the $dE/dx$ distribution, where a percentage of hits are discarded at the highest or lowest $dE/dx$ values before the mean is calculated. With the increasing computing power, another method tries to fit the $dE/dx$ spectrum for each track. A classification that uses the information contained in the individual measurement, by building a likelihood function for each particle type hypothesis. Here, the challenge is to find the correct description of the distribution.

# Chapter 4

# Search For the Y(2175) in Photoproduction at GlueX

## 4.1 Introduction

The discovered structure at 2175 MeV in $e^+e^-$ collider experiments is claimed as an isospin singlet, and its spin-parity is determined to be $J^{PC} = 1^{--}$. While the PDG meanwhile introduced the notation $\phi(2170)$, within this work the state will still be denoted $Y(2175)$. The observation of this resonance, with its peculiar width and mass, besides a seemingly preferential decay modes, has triggered many theoretical interpretations, most of which propose exotic solutions.

Despite all previous experimental efforts, our knowledge of the $Y(2175)$ is not sufficient to confirm or suppress one of the theoretical interpretations. So far, all the experimental information about the $Y(2175)$ are limited to the $e^+e^-$ annihilation and $J/\psi$ hadronic decay. The $Y(2175)$ production in other processes will help to understand its nature.

Hadron production induced by photons has been largely studied since it provides an excellent tool to probe the hadron spectrum [40, 41, 42, 43]. The strong affinity

of photons for $s\bar{s}$ allows to use photon beams to study the strangeonium-like states, like the observation of the $\phi(1020)$ [44] and $\phi(1680)$ [45] in $\gamma p \to K^+K^-p$ reaction. Since the $Y(2175)$ was observed in the $\phi\pi^+\pi^-$ and $\phi f_0(980)$ channels, indicating a substantial $s\bar{s}$ component in the $Y(2175)$, it would be straightforward to search for the resonance $Y(2175)$ in the reaction of $\gamma p \to \phi f_0(980)p$ and $\gamma p \to \phi\pi^+\pi^-p$.

In this chapter, we will search for the $Y(2175)$ resonance in photoproduction, in both $\phi\pi^+\pi^-$ and $\phi f_0(980)$ decay modes, while studying the $\gamma p \to K^+K^-\pi^+\pi^-p$ final state. Thus, we measure cross sections for the $\gamma p \to Y(2175)p \to \phi\pi^+\pi^-p$ and $\gamma p \to Y(2175)p \to \phi f_0(980)p$ resonant and non-resonant (without the $Y(2175)$ state) modes. To achieve that, we start by an event selection to reduce the background, that is followed by a description of the Monte Carlo samples and the real data used in the analysis. We finally report the cross section measurements for the different channels, and discuss the systematic uncertainties associated with theses measurements.

## 4.2 Data and Simulation

### 4.2.1 Data

The first phase running of the GlueX experiment, GlueX Phase-I, was completed at the end of 2018. It has started collecting data since 2016, with four run periods. Theses data sets are used in this study.

#### 4.2.1.1 Data Samples

The data are organized into a number of "runs" that correspond to $\sim$ 2 hours of data collection. In 2016, most of the runs were spent on studying hardware performance, thus only a subset of runs (from 11366 to 11555) are selected, which was the optimal running conditions of the detector.

During the selected set of runs, the polarized photon beam was produced on a thin diamond radiator and passed through the collimator. The diamond was rotated between two perpendicular orientations, parallel and perpendicular polarizations, with respect to the floor. A small set of the selected runs are produced with unpolarized photon beam, using an aluminum radiator instead of the diamond radiator. Since the importance of having a large data sample to increase the probability of finding the $Y(2175)$ in photoproduction, all the different polarizations are combined in a dataset.

The CEBAF accelerator delivers a 250 MHz electron beam, corresponding to a beam bunch spacing of 4.008 ns, with different average intensities in the datasets. Due to large quantity of data collection, and to efficiently store and process these data, a set of conditions were implemented to save only events of potential physics interest. These events that pass the trigger conditions are referred as triggers. For instance, a minimum energy deposition in the FCAL and/or BCAL is used to determine a good event, which is used in the 2017 dataset triggers. A summary of the luminosity in the coherent peak region, the number of triggers, and the running conditions for the different datasets is presented in Tab. 4.1.

Table 4.1: Summary of GlueX Phase-I selected dataset

| Run Period | Coherent Peak Luminosity ($pb^{-}1$) | Number of Triggers (x $10^9$) | Running Conditions | | |
|---|---|---|---|---|---|
| | | | Beam Intensity (nA) | Radiator Thickness ($\mu$m) | Collimator Diameter (mm) |
| 2016 | 2.0 | 6.1 | 160, 200 | 50 | 3.4 |
| 2017 | 21.8 | 49.6 | 100, 150 | 58 | 5.0 |
| Spring 2018 | 58.4 | 146.0 | 50 - 250 | 17, 58 | 3.4, 5.0 |
| Fall 2018 | 39.2 | 80.14 | 450, 200 | 17, 47 | 5.0 |

#### 4.2.1.2 Data Processing

The triggered events are stored in a raw format, which is then processed and used to reconstruct the four-momentum vectors, positions of the tracks and showers, and many other important quantities, like particle identification information. After every improvement in reconstruction and calibration the data is processed again to produce the above quantities with a better precision. The latest reconstruction versions are used in this analysis.

#### 4.2.1.3 Tagged Photon Flux

The tagged photon flux for a data run period is determined using the hit coincidence between the PS and the TAGM or TAGH, including the PS acceptance correction. The tagged flux integrated over the run periods of the different datasets used in this study is shown in Fig. 4.1. The data collected during the running experiment is not always recorded, due to detector and data acquisition limitations. Thus the measured photon flux has to account for the live time, the time that the data acquisition was ready to record events in the experiment, and correct the measured photon flux.

The increase in the number of triggers from 2016 to 2018 spring datasets, is reflected in the flux yields seen in Fig. 4.1. As expected, the coherent photons region is produced between 8 - 9.2 GeV, with a shift in the 2016 dataset energy peak towards a higher energy, due to the decrease in the electron beam energy delivered to the GlueX experiment from $\sim$ 12 GeV in 2016 data to 11.6 GeV in the rest datasets.

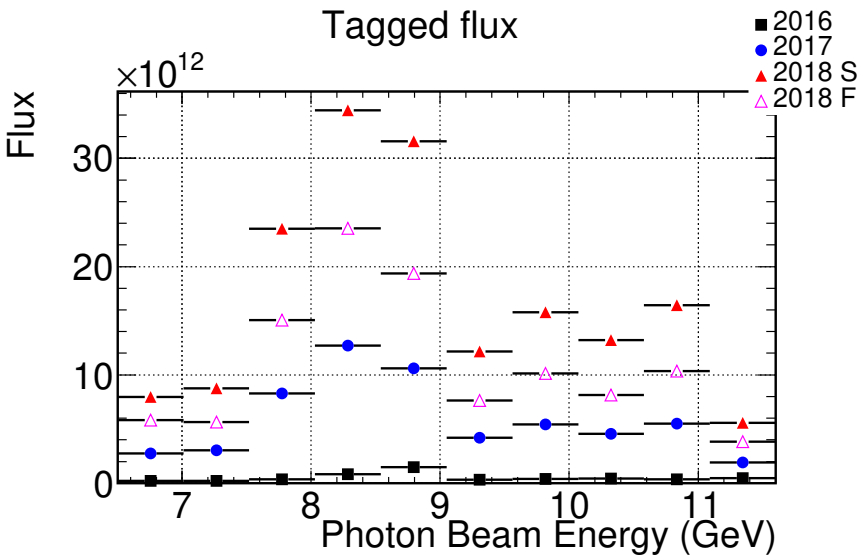


Figure 4.1: The tagged photon flux versus the photon beam energy distributions for 2016 (black), 2017 (blue), Spring 2018 (red), and Fall 2018 (magenta) datasets.

### 4.2.2 Monte Carlo Simulation

To understand our experimental data and obtain the event reconstruction efficiency, a Monte Carlo simulation (MC) is used. The MC samples are generated based on an isobar model, where a meson decays into two particles. The widths and masses of the generated particles are extracted from PDG data [8], with the $Y(2175)$ parameters taken from a weighted data average over multiple experimental measurements. The generator produces four-vectors for a given topology, where the generated final state particles did not include any spin information. The generated beam energy distribution and the momentum transfer are based on the beam properties and t-slope from each datasets, respectively. Four samples for each reaction matching the corresponding year of data taking are generated, and a set of random triggers are included to simulate the detector noise during data collection for every run. The generated events were then passed through the modeled GlueX detectors based on Geant4, to simulate their response. In addition, the results

were then smeared to model the detector resolution and efficiency. Finally, the simulated events were then reconstructed and analyzed in the same way as real data. A summary of theses samples with the number of generated events are shown in Tab. 4.2

Table 4.2: Monte Carlo samples

| MC samples | 2016 | 2017 | Spring 2018 | Fall 2018 |
|---|---|---|---|---|
| $\gamma p \to \phi\pi^+\pi^- p$ | 2 M | 10 M | 9.7 M | 10 M |
| $\gamma p \to Y(2175)p \to \phi\pi^+\pi^- p$ | 2 M | 10 M | 9.7 M | 10 M |
| $\gamma p \to \phi f_0 p$ | 2 M | 10 M | 9.7 M | 10 M |
| $\gamma p \to Y(2175)p \to \phi f_0 p$ | 2 M | 10 M | 9.7 M | 10 M |

The phase space kinematics of the final state particles in the $\gamma p \to \phi\pi^+\pi^- p$, $\phi \to K^+K^-$ process is represented in the Fig. 4.2, where momentum and polar angle for these particles are provided. The pions and kaons receiving a higher momentum will preferentially travel towards the FDC, FCAL and TOF, while the recoiled protons with lower momentum will move with a higher open angle $\sim$ [40° - 60°] relative to the beam direction, to hit mostly the CDC and BCAL.

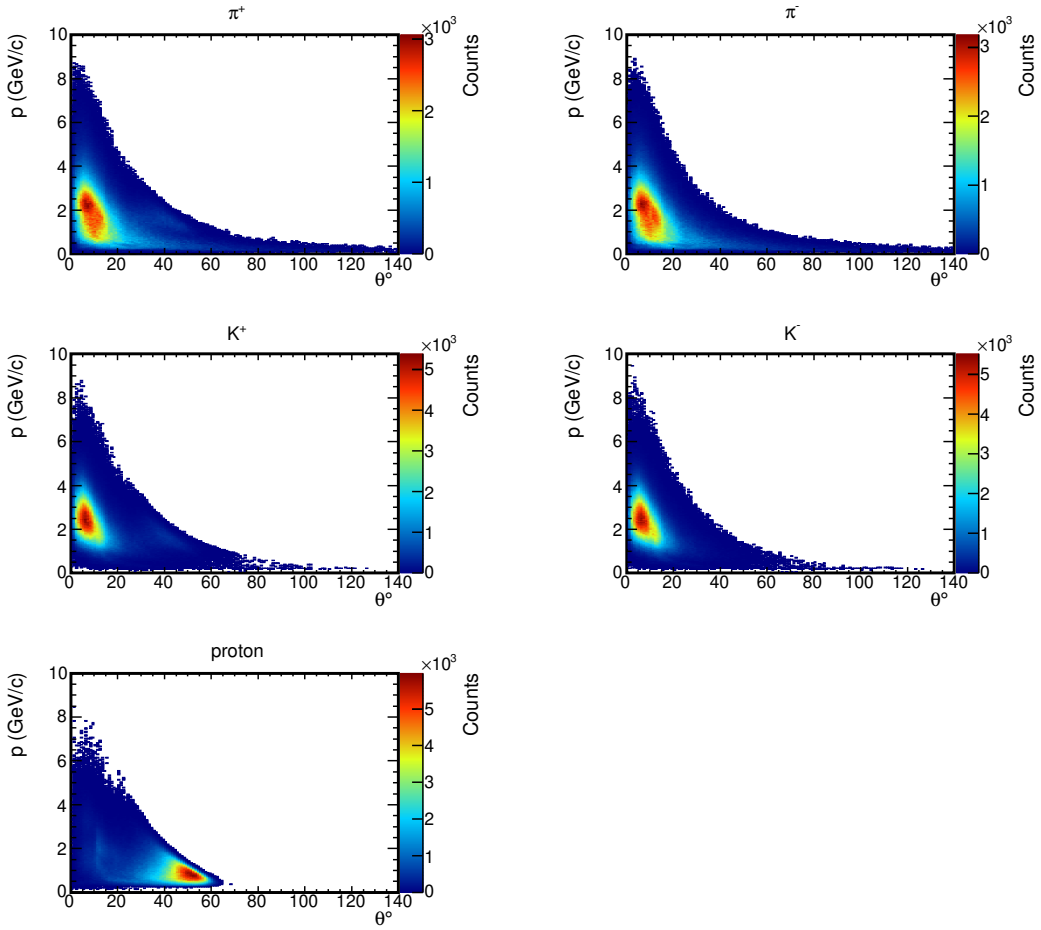


Figure 4.2: Momentum versus polar angle for the $\gamma p \to \phi\pi^+\pi^- p$, $\phi \to K^+K^-$ topology, with the $K^+$, $K^-$, $\pi^+$, $\pi^-$, and proton final state particles after reconstruction in the GlueX detector.

## 4.3 Event Selection

In order to search for $Y(2175)$ in the decay modes $\phi\pi^+\pi^-$ and $\phi f_0(980)$, with $\phi \to K^+K^-$ and $f_0 \to \pi^+\pi^-$, we study the reactions of the form $\gamma p \to K^+K^-\pi^+\pi^-p$. The purpose of the event selection procedure is to subtract as much as possible the background events that mimics our signal, as well as keeping as much as possible the signal events. This is realized by cutting on different variables, then followed by selecting the exclusive $\phi\pi^+\pi^-$ events, since the $\phi f_0(980)$ is a subsample of the $\phi\pi^+\pi^-$.

### 4.3.1 Particle Combinations

We start selecting the candidates for the reaction $\gamma p \to K^+K^-\pi^+\pi^-p$ by requiring one tagged photon beam, three reconstructed positively charged tracks, and two reconstructed negatively charged track, which altogether create a single combination matching to the desired decay. Multiple combinations of the reconstructed particles lead to the possibility of multiple hypotheses for a single event. To prevent double counting of events, we keep track of the particles used in a combination.

### 4.3.2 Beam Photon Accidentals Subtraction

In an event, one or more tagged photons could arrive in the same time window of 4.008 ns to the target. Using one of these wrong photons 'accidentally' arriving in the current time window to constrain momentum and energy for exclusive event reconstruction leads to indistinguishable peaking background in quantities of interest. Since the primary photon and the accidentals arrive in the same time, a selection of the beam bunch time alone will not be sufficient. For this reason, a statistical method is used to remove the contribution from the accidental photons. We estimate the number of events generated from photons outside the beam bunch

time, since the behavior of these photons is similar to the accidental photons but that are for certain not part of the current reaction. This is achieved by estimating the accidental contribution as an average over 8 adjacent time windows (4 before and 4 after the current signal time window) and assigning a weight of 1.0 and $-1/8$ to all the combinations inside and outside the main beam bunch time, respectively. Finally, these weights are used in the analysis to subtract the contribution from the accidental photons. The time difference between the time of the reconstructed tagged photons, and the Radio Frequency (RF) time, which is coming from the accelerator clock corresponding to the incoming beam photon time at the center of the target, is shown in Fig. 4.3. The primary photon beam bunch appear centered near $\Delta t_{Beam-RF} = 0$. In addition to this main peak, four beam bunches in each side equally spaced in time period of 4.008 ns, since the accelerator delivers micro-pulses at 249.5 MHz. These eight peaks are mainly caused by real electron hits in other tagger channels near to the primary photon energy.

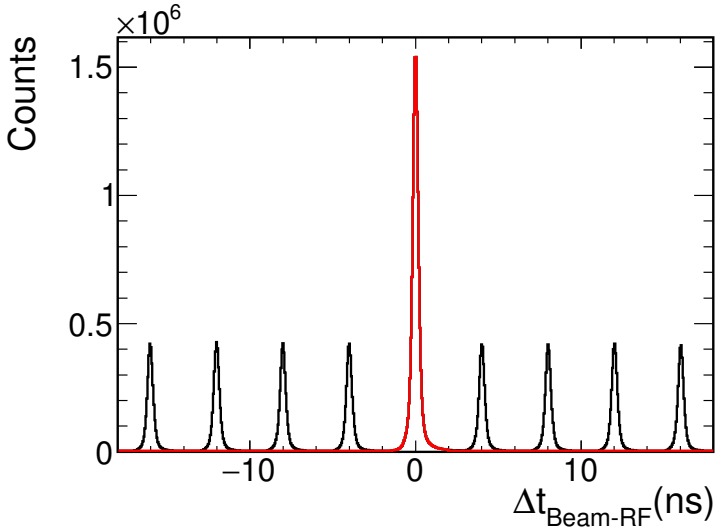


Figure 4.3: Time difference between the tagged photons and the RF clock time. The primary photon beam is shown in the middle peak after accidental subtraction (red), and the near beam bunches are shown in each side of the main peak, separated by 4.008 ns.

### 4.3.3 Track Energy Loss Selection

As discussed in chapter 3, we isolate the recoiled protons from the pions and kaons detected in the CDC, by applying a cut on the dE/dx. To select between the different mass hypotheses for charged tracks, we use an exponential function to select proton candidates as described by Eq. 4.1 and lighter particle candidates (pions and kaons) as given by Eq. 4.2:

$$\frac{dE}{dx} > e^{(-4.0\ p+2.25)} + 1.0\ ,\ \text{and} \tag{4.1}$$

$$\frac{dE}{dx} < e^{(-7.0\ p+3.0)} + 6.2\ , \tag{4.2}$$

where $p$ is the momentum of the particles. Fig. 4.4 shows the energy loss of positively charged particles as a function of their momentum. According to the Bethe-Bloch formula, lower momentum protons deposit more energy (curved band in Fig. 4.4) than lighter particles (horizontal band in Fig. 4.4) for the same momentum. A good separation between the particles is seen up to $\sim 1$ GeV/$c^2$ momentum. A more conservative cut is applied on the $dE/dx$ to avoid throwing potential good events that are closer to the region where the two bands merge.

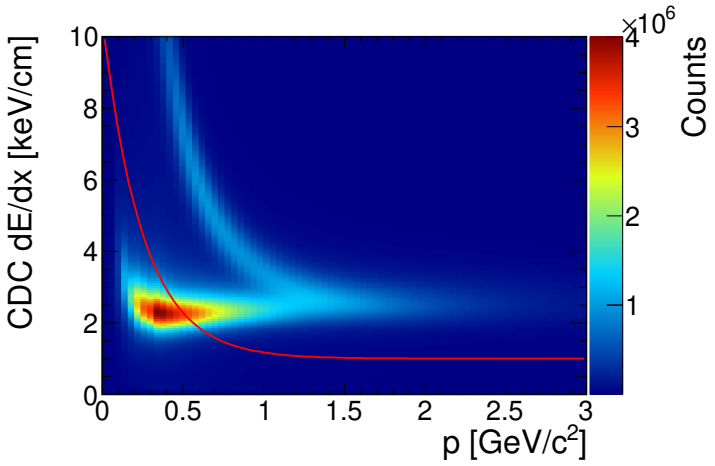


Figure 4.4: dE/dx of positively charged particle as a function of their momentum in the CDC. The curved and horizontal bands represent protons and lighter particles (kaons and pions) candidates, respectively. The proton candidates above the red curve (Eq. 4.1) are kept.

### 4.3.4 Timing Selection

Comparing the RF beam bunch time and the track vertex time for every final state particle candidate $K^+$, $K^-$, $\pi^+$, $\pi^-$ and proton candidates, provides a good PID, and a timing cut was made in each subdetector. The vertex time is the time of the matched hit, propagated to the point of closest approach to the beamline. Since the reference plane for timing is chosen to be at the center of the liquid hydrogen target, a correction is made to the vertex time to account for the distance between the vertex location and the reference plane. Fig. 4.5 shows this timing difference for the TOF detector for proton candidates both in data (fig. 4.5a) and MC simulation (fig. 4.5b), as a function of particle momentum. The protons appear in the range [-0.3,+0.3] (ns), corresponding to a $3\sigma$ cut around the mean, where $\sigma \sim 100$ ps is the TOF detector time resolution. The other entries outside this time window are pions and/or kaons, which is the reason for their strong suppression in MC simulation. A loose selection is also applied on the rest af the particle candidates,

due to the non trivial particle bands distinction. A summary of the timing cuts are listed in tab. 4.3.

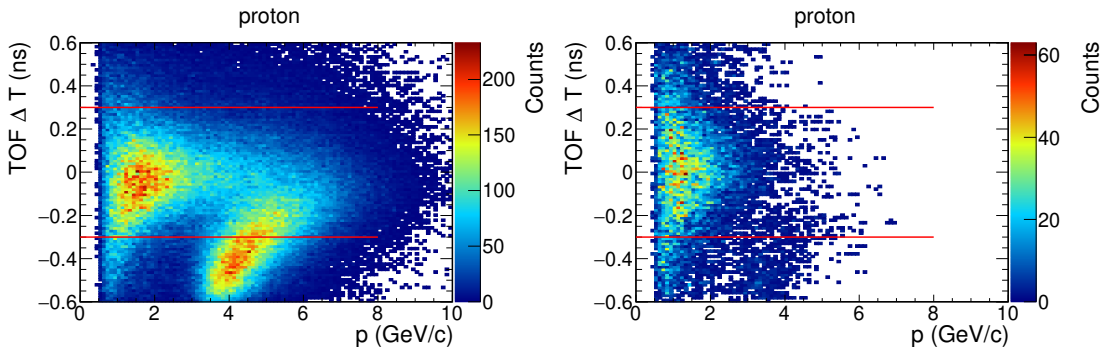


(a) (b)

Figure 4.5: The difference between the time measured by TOF after propagation to interaction vertex and the time delivered by the RF clock for protons as a function of particle momentum in (a) data and (b) MC simulation. The time window selected is shown between the two red lines, corresponding to the proton candidates. The curved time band is due to mis-identified protons with lighter particle (pions and kaons) arriving earlier in time to the TOF detector.

Table 4.3: Events selection using the difference between the RF and vertex time at each detector system.

| Candidate | Detector System | $\Delta T_{detector-RF}$ Cut (ns) |
|---|---|---|
| $\pi^{\pm}$ | TOF | $\pm$ 0.5 |
| $\pi^{\pm}$ | BCAL | $\pm$ 1.0 |
| $\pi^{\pm}$ | FCAL | $\pm$ 2.0 |
| $\pi^{\pm}$ | SC | $\pm$ 2.5 |
| $K^{\pm}$ | TOF | $\pm$ 0.3 |
| $K^{\pm}$ | BCAL | $\pm$ 0.75 |
| $K^{\pm}$ | FCAL | $\pm$ 2.5 |
| $K^{\pm}$ | SC | $\pm$ 2.5 |
| proton | TOF | $\pm$ 0.3 |
| proton | BCAL | $\pm$ 1.0 |
| proton | FCAL | $\pm$ 2.0 |
| proton | SC | $\pm$ 2.5 |

### 4.3.5 Kinematic Fitting

Kinematic fitting is a mathematical procedure in which we rely on physics principles governing the particles in the reaction or decay process to improve the measured quantities, *e.g.*: energy, momentum, position,..., *etc.* For instance, considering the reaction, $\gamma p \to K^+K^-\pi^+\pi^-p$. The fact that the five final state particles are coming from a common vertex position can be used to improve the measured position and momentum vectors. The total four-momentum of the final states must equal to the initial beam four-momentum, thus improving the energy and momentum resolution measured of these particles. The fit takes a fully specified reaction 4-momenta and covariance matrices for all initial and final state particles, and the results of this fit can be used to provide criteria for rejecting background events that does not satisfy the fit constrains and to improve measured quantities.

The kinematic fitting is performed on the measured parameters $y$ (4-momenta, position), together with the errors and correlations among each other, represented by the covariance matrix $V_y^{-1}$. The estimated fit quantities are obtained after minimizing the $\chi^2$ of the overall kinematic fit, satisfying each of the different constrains. The $\chi^2$ is defined as

$$\chi^2 = (y-\eta)^T V_y^{-1}(y-\eta) \ , \tag{4.3}$$

If the formulated hypothesis matches the true reaction then the kinematic fit $\chi^2/ndf \sim 1$ corresponding to $\chi^2 \sim 11$ in our case, where the number of degrees of freedom, $ndf$ = number of observables - number of constrains = 11. In data, mainly the non-matching hypotheses (*i.e.* no $K^+K^-\pi^+\pi^-$ event) make the distribution differ from MC, leading to higher tales in the kinematic fit $\chi^2$ distribution. The normalized distributions of kinematic fit $\chi^2$ for the different datasets in data and MC

simulation are shown in Fig. 4.6a and Fig. 4.6b, respectively. The $\chi^2$ distributions are consistent between the different datasets, except for the 2018 Spring dataset, which shows a less converging $\chi^2$ in data, and is still under investigation. To insure the minimization of the $\chi^2$, the kinematic fit is required to converge. The $\chi^2$ cut is selected based on the optimal significance ($Z$) defined by

$$Z = \frac{S}{\sqrt{S+B}} \ , \tag{4.4}$$

Where $S$ and $B$ are the number of $\phi\pi^+\pi^-$ data signal and background events, respectively.

The signal and background events are extracted by fitting the $K^+K^-$ invariant mass and integrating in the [1, 1.05 GeV/c$^2$] mass region. The $S$ and $B$ are obtained after different kinematic fit $\chi^2$ cuts, from a $\chi^2 < 100$ to $\chi^2 < 5$ in 20 steps, a subset is seen in Fig. 4.7. The signal shape is described by a Voigtian model ($V$), which is a convolution of a Breit-Wigner ($BW$) and a Gaussian ($G$) functions, defined as

$$\begin{aligned} V(x;\sigma,\Gamma) &= \int_{-\infty}^{+\infty} G(x';\sigma)BW(x-x';\Gamma)dx' \ , \\ BW(x;\Gamma) &= \frac{A}{2\pi}\frac{\Gamma}{(x-\mu)^2+(\frac{\Gamma}{2})^2} \ , \\ G(x;\sigma) &= \frac{1}{\sigma\sqrt{2\pi}}e^{-\frac{1}{2}(\frac{x-\mu}{\sigma})^2} \end{aligned} \tag{4.5}$$

Here, $\Gamma$ is the Full-width at half-maximum (FWHM) of the Breit-Wigner profile and $\sigma$ is the standard deviation of the Gaussian profile. The amplitude ($A$), mean ($\mu$), $\sigma$, and $\Gamma$ are the fit parameters. The background shape is described by the Chebyshev polynomial $T_n(x)$ of second degree. For any degree $n$ the Chebyshev polynomial is defined as

$$T_n(x) = \frac{(-2)^n n!}{(2n)!}\sqrt{1-x^2}\frac{d^n}{dx^n}(1-x^2)^{n-1/2} \ , \tag{4.6}$$

After extracting the signal and background events, the significance is calculated for each $\chi^2$ cut using Eq. 4.4. The resulting significance as a function of the selection variable is displayed in Fig. 4.8. The optimal significance is realized by a cut of $\sim \chi^2 < 55$, and this selection is used through all the following analysis. The optimal $\chi^2$ cut is indicated by the vertical red line in Fig. 4.6.

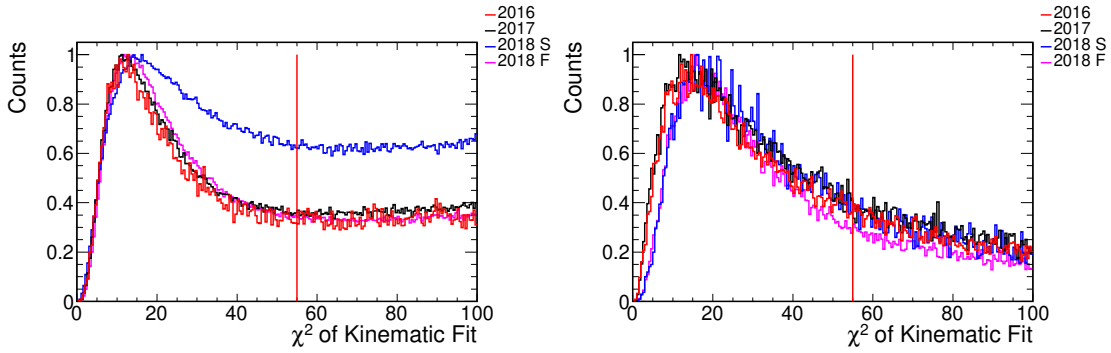


(a) (b)

Figure 4.6: Kinematic fit $\chi^2$ normalized distributions in (a) data and (b) MC simulation, for the different datasets.

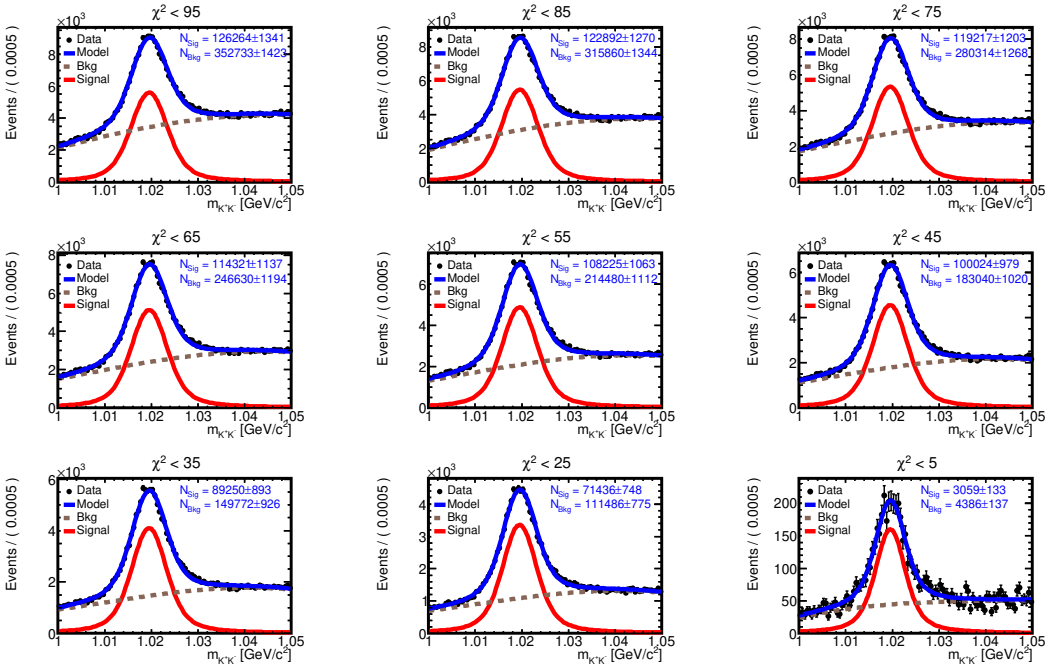


Figure 4.7: $K^+K^-$ invariant mass after each kinematic fit $\chi^2$ cut, as shown on the top of the histograms. The signal (red) and background (dashed line) fits are described by Eq. 4.5 and Eq. 4.6, respectively. The total fit is shown in blue. The number of signal ($N_{Sig}$) and background ($N_{Bkg}$) events are displayed for every cut.

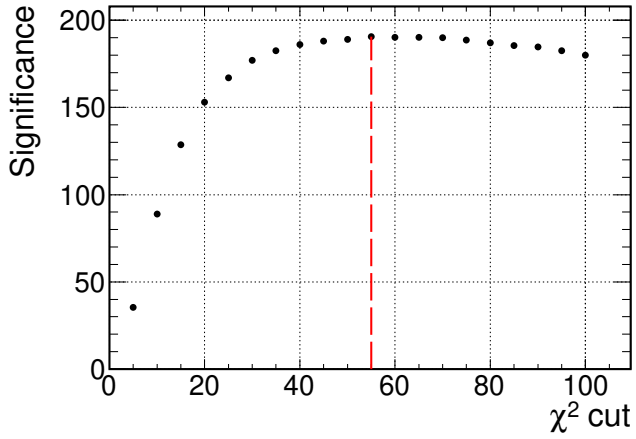


Figure 4.8: Significance as a function of the kinematic fit $\chi^2$ cuts. The red vertical line shows the optimal significance and the corresponding best cut.

### 4.3.6 Missing Mass Squared

The conservation of the four-momentum in the exclusive reaction is required, and since all the final state particles were reconstructed, the missing mass, defined in Eq. 4.7, should be negligible. However, the missing mass is not vanishing due to the detection uncertainty in identification of the particle masses, which represents a source of background. The normalized missing mass squared distributions for the different datasets, both in data and MC simulation are shown in Fig. 4.9a and Fig. 4.9b, respectively. The distributions are very consistent between the datasets in data, with a small variations in the missing mass resolution in MC. To reduce this background, we select events with a missing mass squared ($MM$) close to 0, and the $MM^2$ cut will be determined again based on the optimal significance defined previously in Eq. 4.4. The significance is calculated after every $MM^2$ symmetric cut, from $\pm 0.1$ (GeV/$c^2$)$^2$ down to 0 in 20 steps of 0.005 (GeV/$c^2$)$^2$, a subset is shown in Fig. 4.10. The maximum significance is reached for a $MM^2$ cut in the range [-0.035,+0.035] (GeV/$c^2$)$^2$, indicated by the vertical red dashed line both, in Fig.4.11 and Fig.4.9.

$$\begin{aligned} MM^2 &= \left(\sum P_i - \sum P_f\right)^2 \\ &= \left[(P_\gamma + P_{proton}) - (P_{k^+} + P_{k^-} + P_{\pi^+} + P_{\pi^-} + P_{p'})\right]^2 , \end{aligned} \tag{4.7}$$

the $P_i$ and $P_f$ are the four-momenta of the initial and final particles, respectively. The $P_{p'}$ is the four-momentum of the recoiling proton.

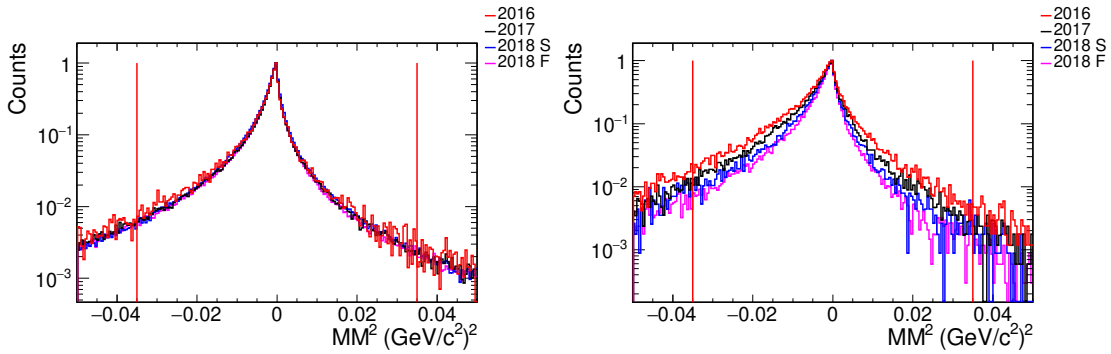


(a) (b)

Figure 4.9: The missing mass squared normalized distributions in (a) data and (b) MC simulation, for the different datasets.

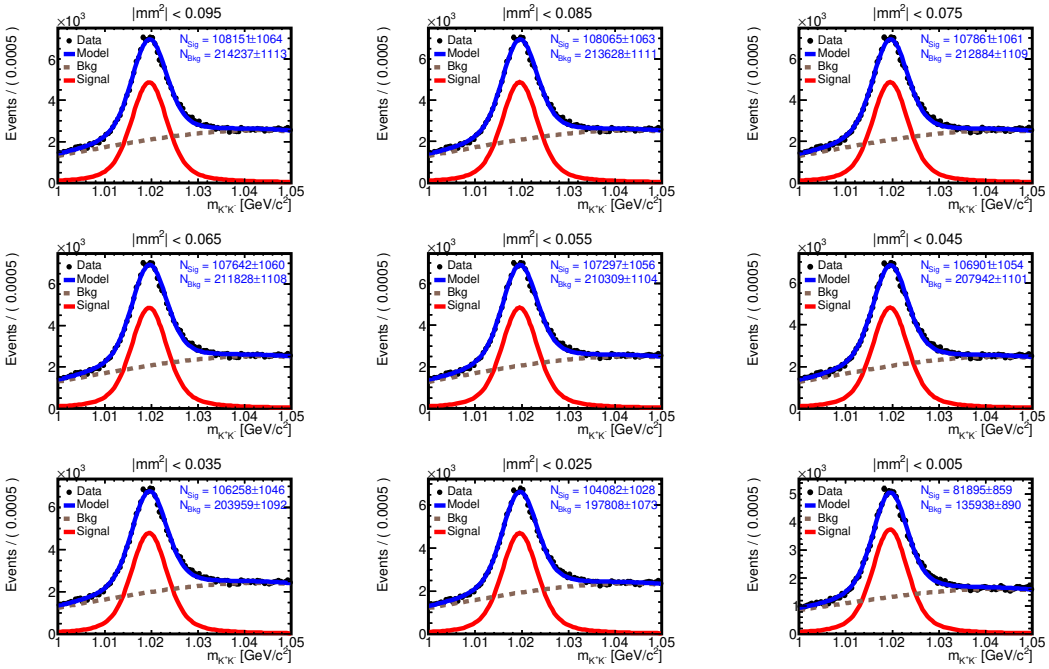


Figure 4.10: $K^+K^-$ invariant mass after each $MM^2$ cut, as shown on the top of the histograms. The signal (red) and background (dashed line) fits are described by Eq. 4.5 and Eq. 4.6, respectively. The total fit is shown in blue. The number of signal ($N_{Sig}$) and background ($N_{Bkg}$) events are displayed for every cut.

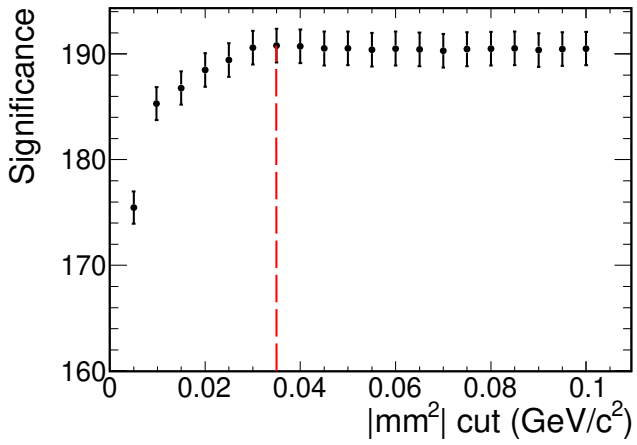


Figure 4.11: Significance as a function of cuts on the missing mass squared. The red vertical line shows the optimal significance and the corresponding best cut.

## 4.4 Cross Section and Upper Limit

In this section, the measurement of the cross sections for the exclusive $\gamma p \to \phi\pi^+\pi^- p$ and $\gamma p \to \phi f_0 p$ reactions is discussed, as well as the determination of an upper limit on the production cross section of the $Y(2175)$ in $\gamma p \to Y(2175)p \to \phi\pi^+\pi^- p$ and $\gamma p \to Y(2175)p \to \phi f_0 p$ reactions.

### 4.4.1 Cross Section for $\gamma p \to \phi\pi^+\pi^- p$

To study the effect of the photon beam energy ($E_\gamma$) in both, the coherent and incoherent region, as well as the momentum transfer (-$t$) dependence on the cross section, the total hadronic cross section for $\gamma p \to \phi\pi^+\pi^- p$ reaction in $t$-channel is studied as a function of both $E_\gamma$ and -$t$. The cross section is measured in the $E_\gamma$ region of 6.5 - 11.6 GeV, distributed equally into 10 bins of 0.51 GeV width, and in the 0 - 4 GeV$^2$ region of -$t$, divided into 10 intervals of 0.4 GeV$^2$ width. The total cross section for the $\gamma p \to \phi\pi^+\pi^- p$ reaction is defined as

$$\sigma_{\gamma p \to \phi\pi^+\pi^- p} = \frac{N^{Data}_{\phi\pi^+\pi^-}}{\varepsilon \; \mathcal{L} \; BR(\phi \to K^+K^-)}, \tag{4.8}$$

The numerator is the number of $\phi\pi^+\pi^-$ signal events observed in real data. The reconstruction efficiency ($\varepsilon$) is ratio of the number of $\phi\pi^+\pi^-$ reconstructed signal events in MC simulation and the total number of generated events. The luminosity ($\mathcal{L}$) is the product of the integrated flux extracted from Fig. 4.1 and the target thickness of 1.273 $b^{-1}$. The last term is the branching ratio of $\phi \to K^+K^-$ taken from [8], with $BR(\phi \to K^+K^-) = 0.492 \pm 0.005$.

The number of generated events are extracted in bins of $E_\gamma$ and -$t$, from the total generated events in the MC samples. The total generated events are distributed over the selected region of $E_\gamma$ and -$t$, as shown in Fig. 4.12.

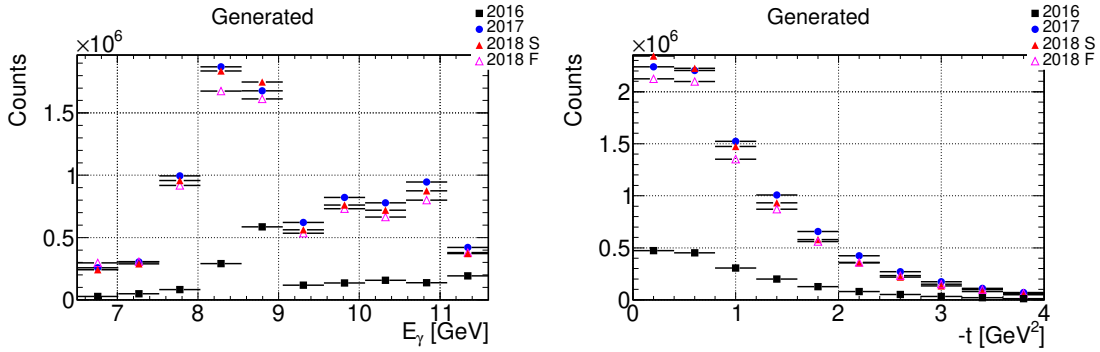


(a) (b)

Figure 4.12: The total generated $\phi\pi^+\pi^- p$ MC samples distributed in (a) $E_\gamma$ and (b) -$t$ bins. The low number of the 2016 MC sample (black squares) reflects the number of events generated for this sample of only 2 M events compared to the other samples of 10 M events each.

The number of $\phi\pi^+\pi^-$ signal events in both MC and data are extracted from fitting the $K^+K^-$ invariant mass in every $E_\gamma$ and -$t$ bin. The correlations between the $K^+K^-$ invariant mass and both $E_\gamma$ and -$t$ are shown in Fig. 4.13. A clear $\phi(1020)$ resonance is seen around the mass of 1.020 GeV/$c^2$, corresponding to the

horizontal band in Fig. 4.13. The signal shape is described by a Voigtian model (Eq. 4.5) and the background by a $4^{th}$ degree Chebyshev polynomial (Eq. 4.6). The $\phi\pi^+\pi^-$ yields obtained for each $E_\gamma$ and -$t$ bin are shown in Fig. 4.18 and Fig. 4.19, respectively. As expected, the yield is more important in the coherent beam region and at low momentum transfer. The small yield drop in the first -$t$ bin, could be due to the detection loss of the recoiled protons at low momentum.

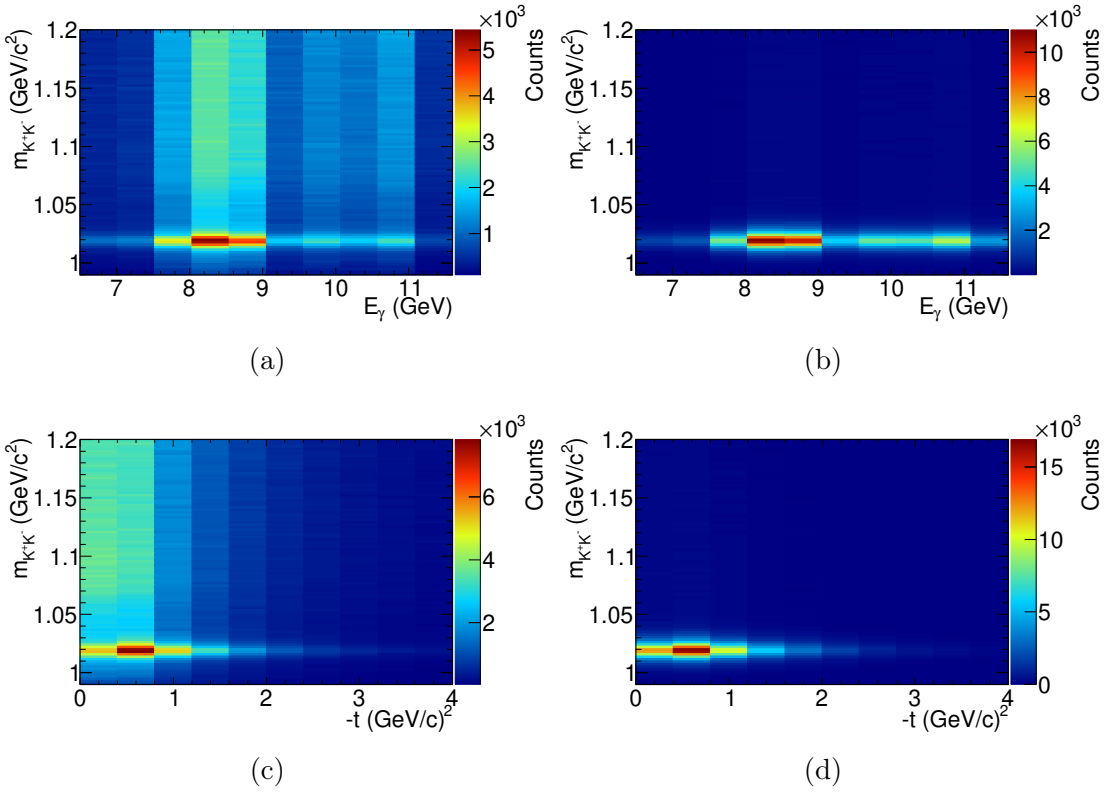


Figure 4.13: $K^+K^-$ invariant mass versus $E_\gamma$ in (a) MC and (b) data, as well as versus -$t$ in (c) MC and (d) data, for the 2017 sample. The horizontal narrow band $\sim$ 1.020 GeV/$c^2$ is the $\phi(1020)$ resonance.

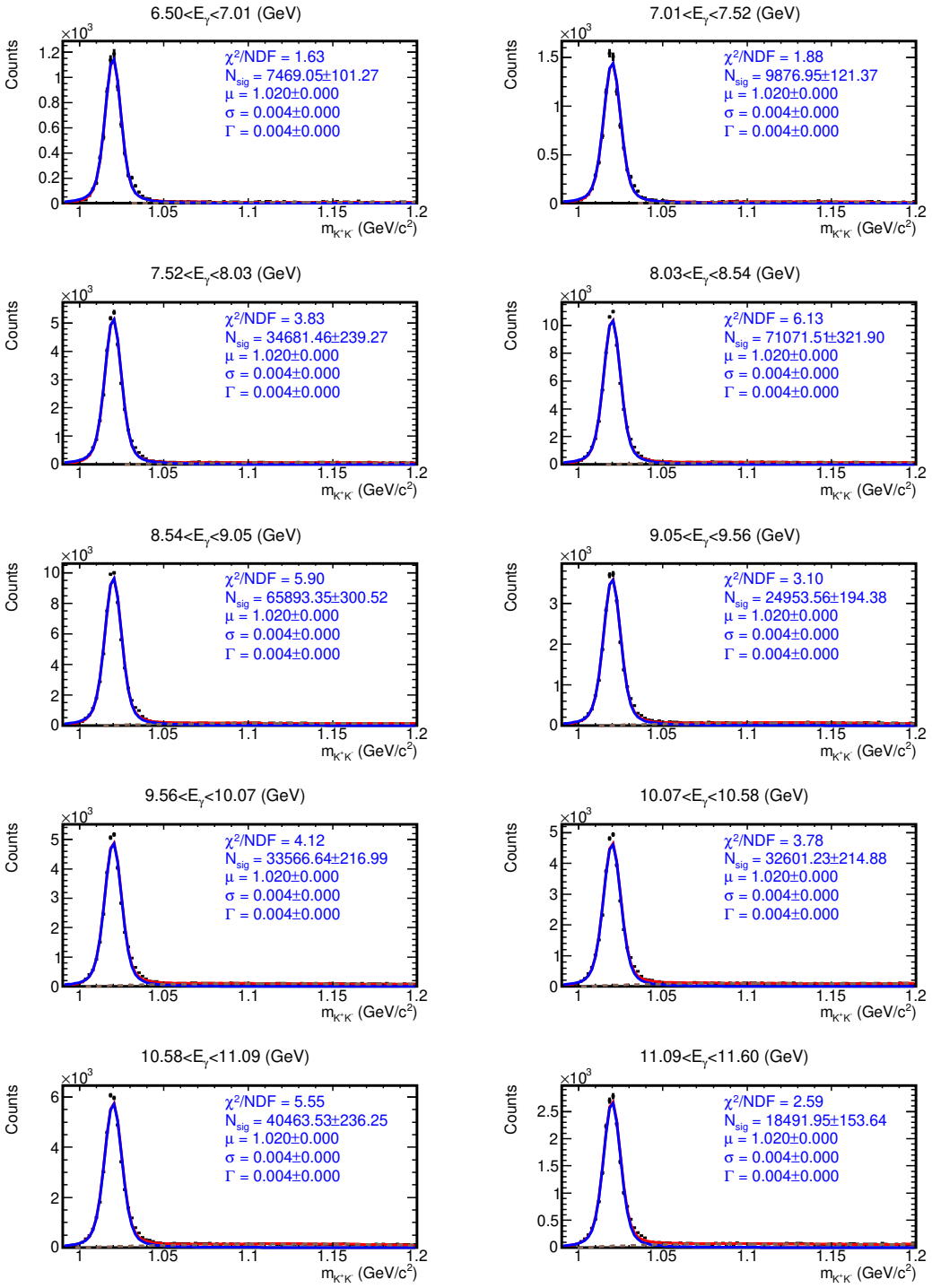


Figure 4.14: $K^+K^-$ invariant mass in $E_\gamma$ bins for 2017 MC sample. The $E_\gamma$ bin ranges and the fit parameters for the total (red), signal (blue), and background (dashed) fits are shown.

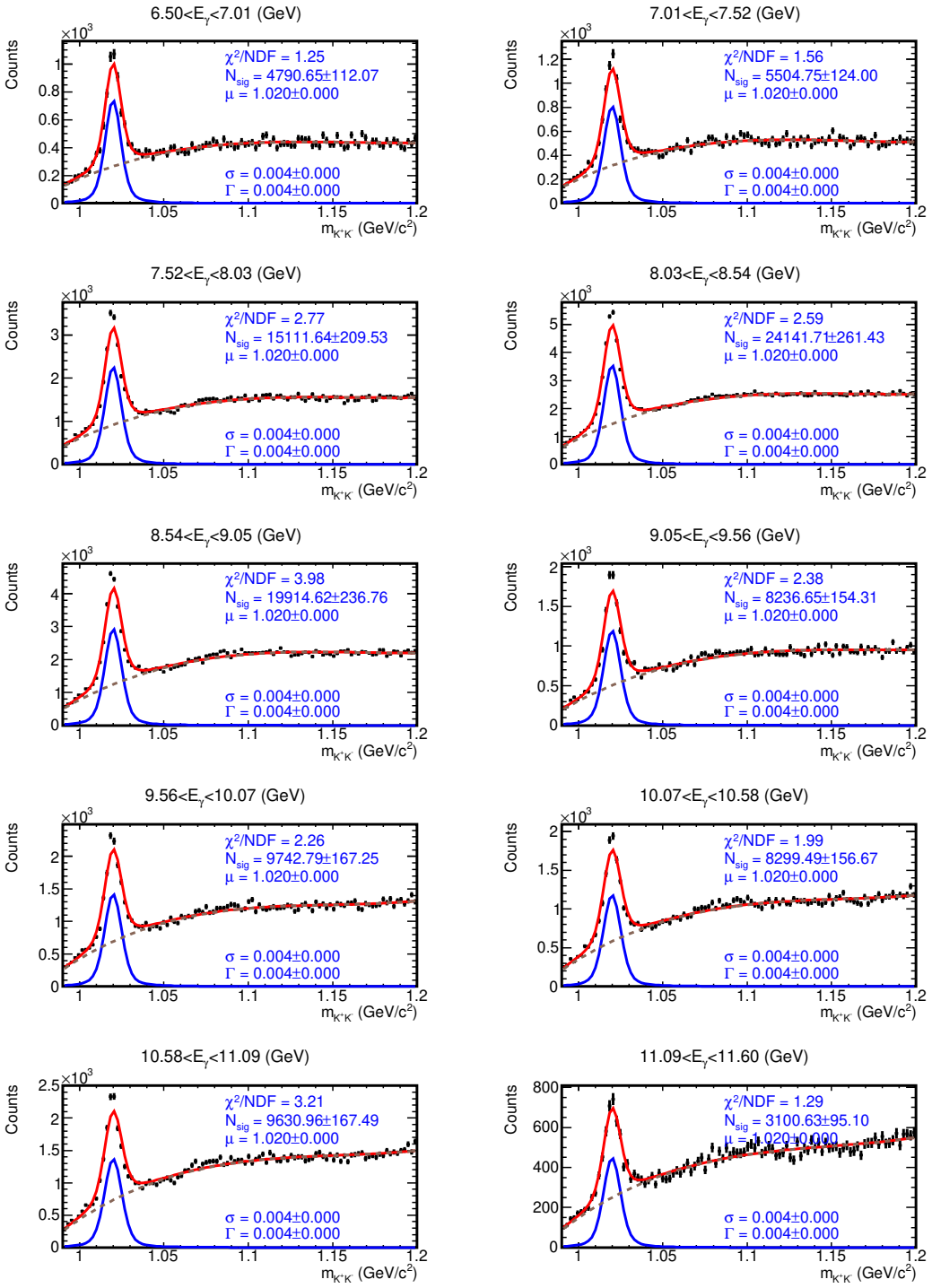


Figure 4.15: $K^+K^-$ invariant mass in $E_\gamma$ bins for 2017 dataset. The $E_\gamma$ bin ranges and the fit parameters for the total (red), signal (blue), and background (dashed) fits are shown.

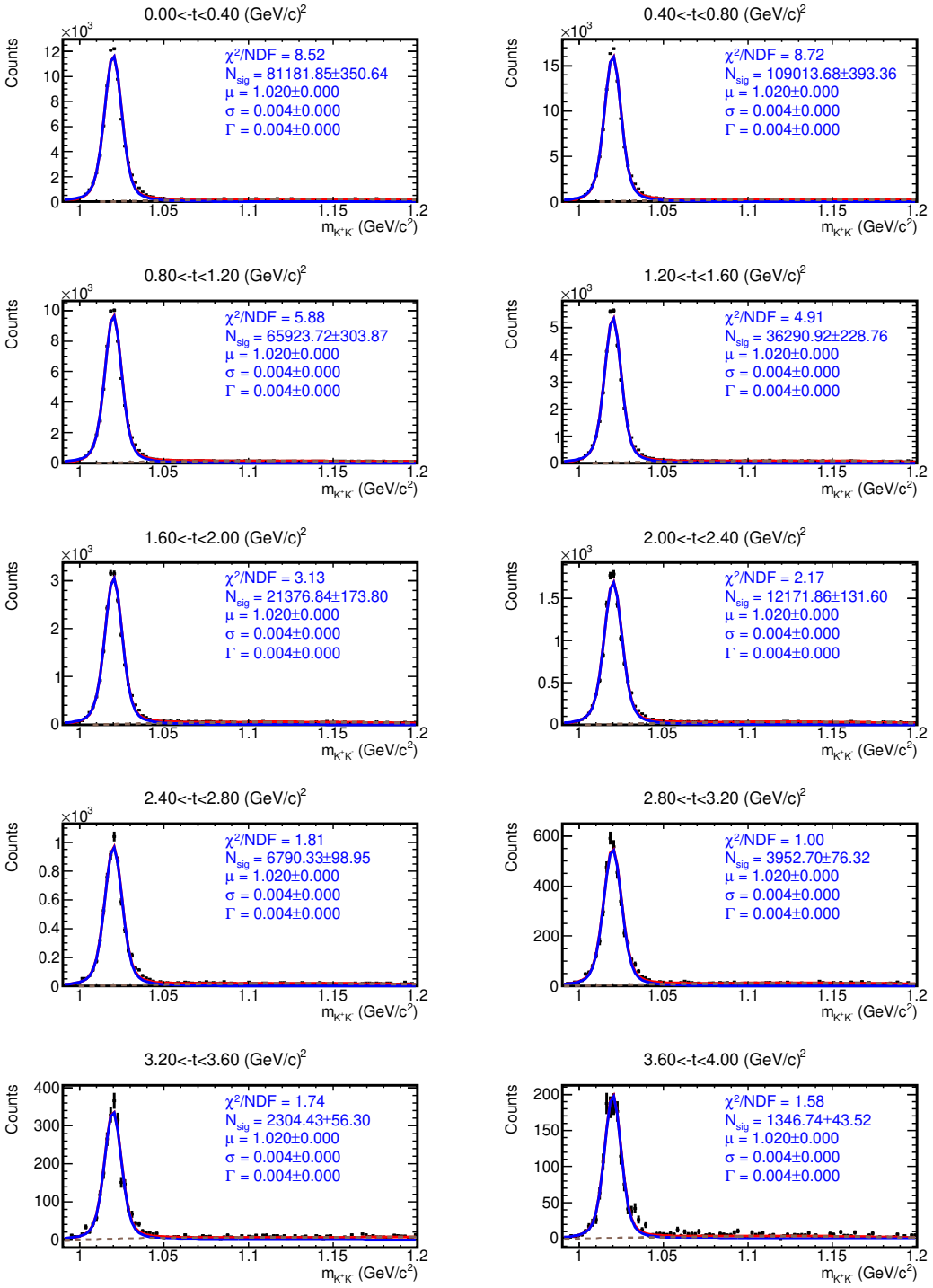


Figure 4.16: $K^+K^-$ invariant mass in -$t$ bins for 2017 MC sample. The -$t$ bin ranges and the fit parameters for the total (red), signal (blue), and background (dashed) fits are shown.

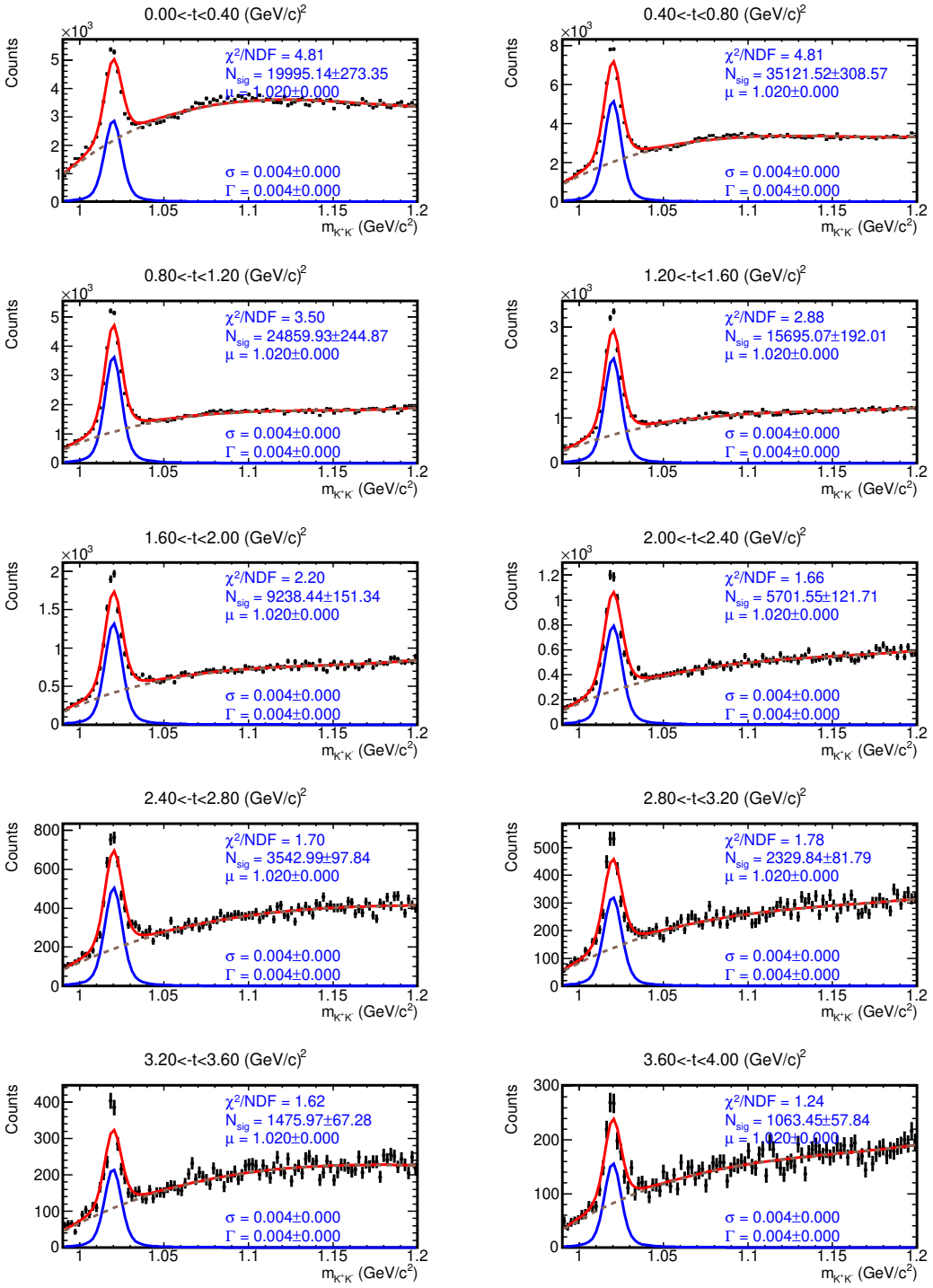


Figure 4.17: $K^+K^-$ invariant mass in -$t$ bins for 2017 data sample. The -$t$ bin ranges and the fit parameters for the total (red), signal (blue), and background (dashed) fits are shown.

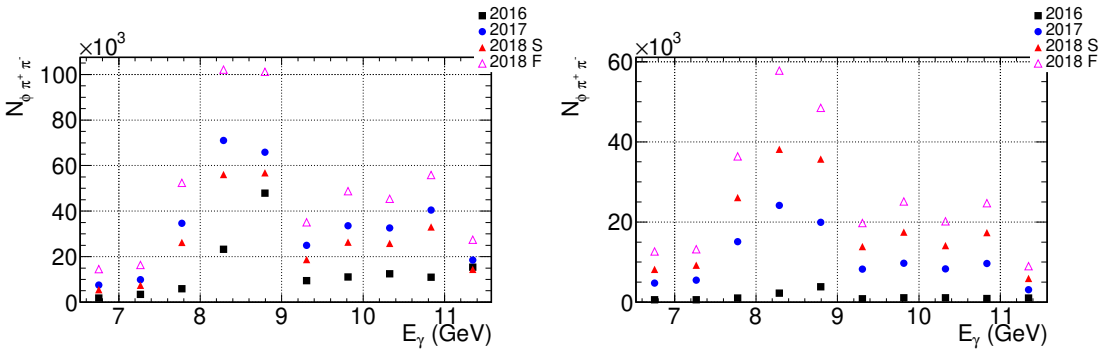


(a) (b)

Figure 4.18: $\phi\pi^+\pi^-$ yields versus $E_\gamma$ in (a) MC and (b) data. The yield for the 2016 (black), 2017 (blue), Spring 2018 (red), and Fall 2018 (magenta) are displayed. The low yields in 2016 reflects the low number of events generated and the low number of triggers in MC and data, respectively.

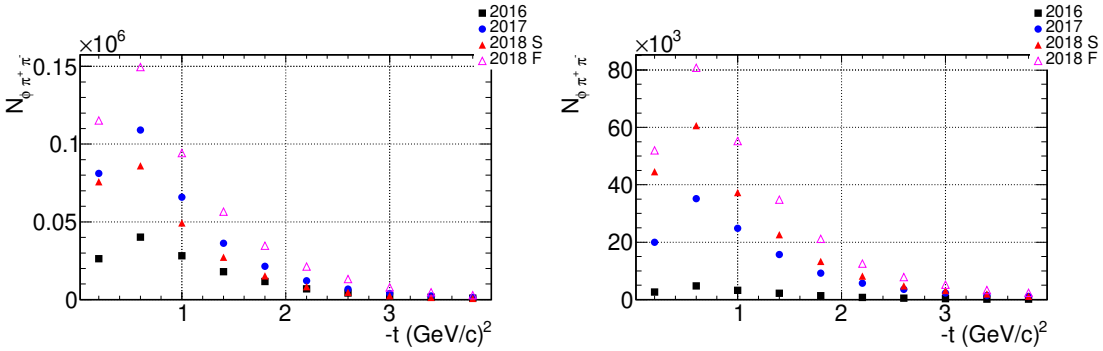


(a) (b)

Figure 4.19: $\phi\pi^+\pi^-$ yields versus -$t$ in (a) MC and (b) data. The yield for the 2016 (black), 2017 (blue), Spring 2018 (red), and Fall 2018 (magenta) are displayed. The low yields in 2016 reflects the low number of events generated and the low number of triggers in MC and data, respectively.

The efficiency is then calculated as the ratio of the $\phi\pi^+\pi^-$ reconstructed MC yields and the total number of generated MC events. The results are plotted in Fig. 4.18, showing the efficiencies versus $E_\gamma$ and -$t$ for the different MC samples. The 2017 and Spring 2018 efficiencies are very comparable to each other, and almost $\sim 50\%$ lower then for the 2016 and Fall 2018 datasets. This is mainly due to the

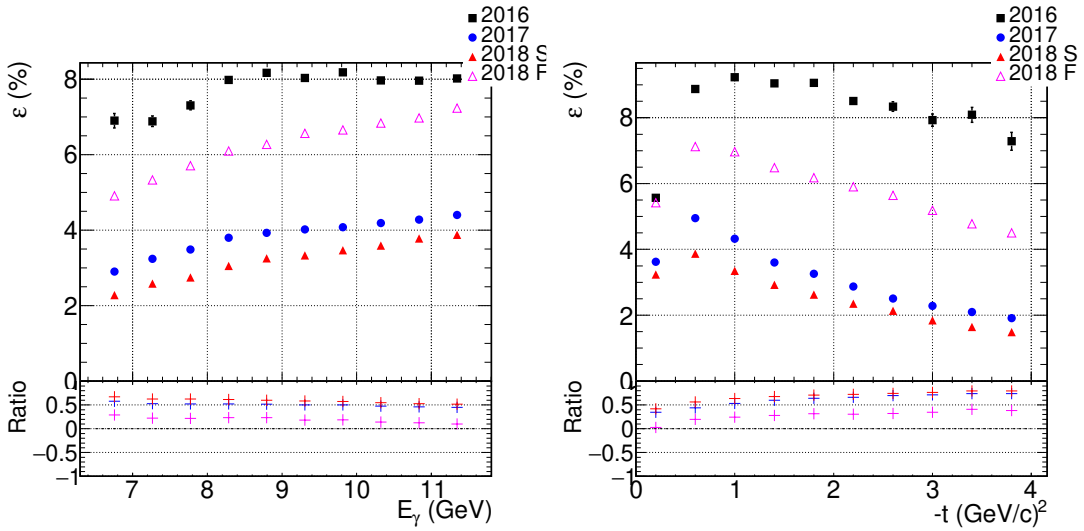


(a) (b)

Figure 4.20: The reconstruction efficiency versus (a) $E_\gamma$ and (b) -$t$, for $\phi\pi^+\pi^-$ MC samples of 2016 (black), 2017 (blue), Spring 2018 (red), and Fall 2018 (magenta). The relative ratio of 2017 (blue), Spring 2018 (red), and Fall 2018 (magenta), w.r.t to 2016 datasets are shown in the bottom plot.

different running conditions and random trigger rates included in the different MC sets.

Finally, having gathered all the ingredients, the cross section is then calculated using Eq. 4.8. The yields, efficiencies and cross sections for the datasets are summarized in Tab. 4.4 - 4.11. The resultant cross sections versus $E_\gamma$ and -$t$ for the different datasets are shown in Fig. 4.21. The total cross section for the different datasets are very close and in some points are consistent within errors, except for the 2107 data that is systematically higher then the other datasets. This effect is still under investigation. The total errors are a quadratic sum of the statistical and systematic uncertainties, the estimation of systematic errors will be discussed in Sec. 4.5.

In order to check the consistency of the cross section shape also for 2017 data, the cross section measurements for the 2016, Spring and Fall 2018 are used to

produce an average total cross section for every $E_\gamma$ and -$t$. The method used to average the cross sections is a standard weighted least-squares procedure [8]. Since the datasets are independent, the cross section measurements are uncorrelated, and the weighted average and error are then calculated by

$$\bar{\sigma} \pm \delta\bar{\sigma} = \frac{\sum_i w_i \sigma_i}{\sum_i w_i} \pm \left( \sum_i w_i \right)^{-1/2} , \tag{4.9}$$

with

$$w_i = 1/(\delta\sigma_i)^2$$

Here $\sigma_i$ and $\delta\sigma_i$ are the values and errors of the measured cross sections, with $i = 1, 2, 3$ for the three different datasets, and the sum run over $N = 3$ measurements. We then have two main cases depending on the $\chi^2/(N-1)$ ratio, with

$$\chi^2 = \sum w_i (\bar{\sigma} - \sigma_i)^2 \tag{4.10}$$

If this ratio is smaller or equal to 1, then the final average cross section is as defined in Eq. 4.9. But if the ratio is slightly larger then 1, then we increase our average errors $\delta\bar{\sigma}$ in Eq. 4.9, by a scale factor $S$ defined as

$$S = [\chi^2/(N-1)]^{1/2} \tag{4.11}$$

The idea here is that large value of the $\chi^2$ is likely due to underestimation of errors in at least one of the cross section measurements. Since the measurement with the underestimated error is not known, we assume they are all underestimated by the same factor $S$. Scaling up all the cross section errors by this factor, the ratio gets closer to unity, and consequently the average error $\delta\bar{\sigma}$ scales up by the same factor.

After the calculations of the average cross section for the 2016, Spring and Fall

2018 data, as seen in Fig. 4.22, the 2017 cross section is scaled by an empirical constant factor of 0.76 and 0.63 in $E_\gamma$ and -$t$, respectively. The resultant 2017 corrected cross sections are now consistent within errors with the average cross sections, except at low -$t$, where the difference between the measurements have increased. These scaling factors will help to quantify the sources of the cross section measurement discrepancies between the different datasets.

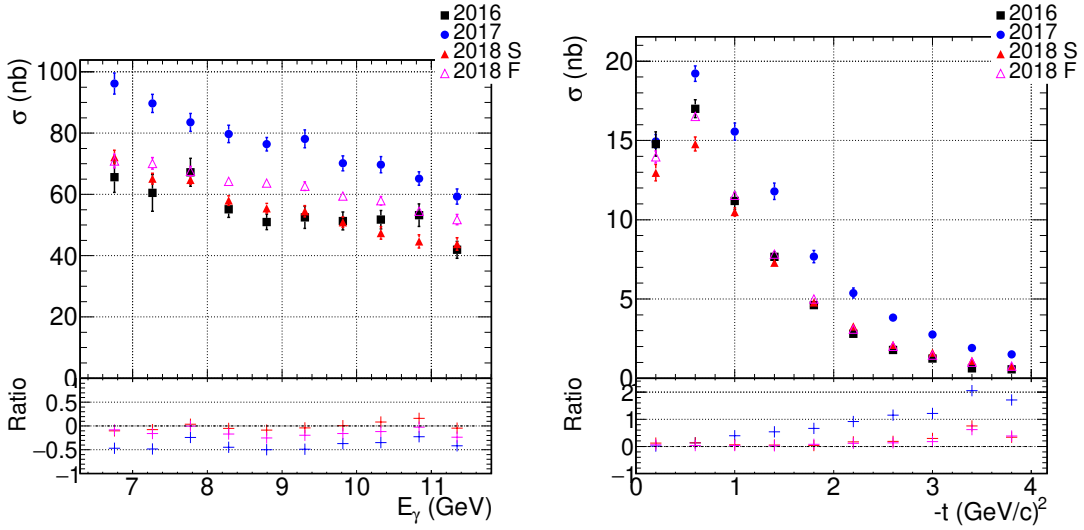


(a) (b)

Figure 4.21: $\gamma p \to \phi\pi^+\pi^- p$ total cross section versus (a) $E_\gamma$ and (b) -$t$, for 2016 (black), 2017 (blue), Spring 2018 (red), and Fall 2018 (magenta). The relative ratio of 2017 (blue), Spring 2018 (red), and Fall 2018 (magenta), w.r.t to 2016 are shown in the bottom plot.

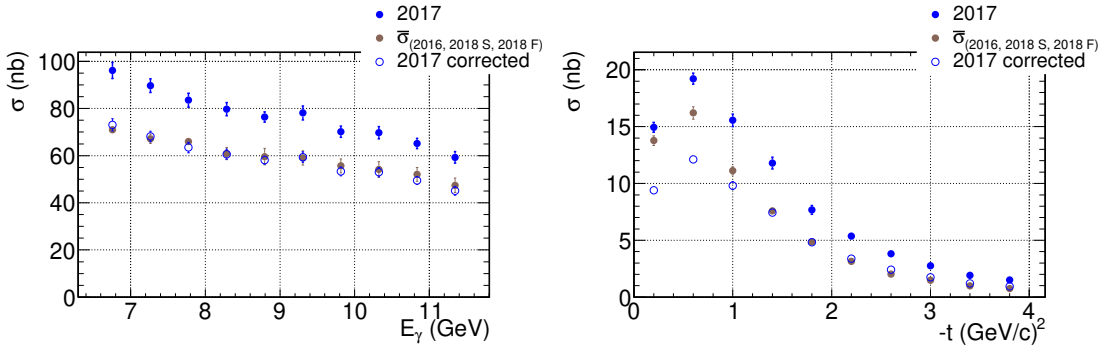


(a) (b)

Figure 4.22: $\gamma p \to \phi\pi^+\pi^- p$ average cross section (Brown) for the 2016, Spring and Fall 2018 datasets, versus (a) $E_\gamma$ and (b) -$t$. The 2017 results before (blue full circles) and after correction (open circles) cross sections are shown.

Table 4.4: $\phi\pi^+\pi^-$ yields in MC ($N_{MC}$) and data ($N_{Data}$), efficiencies ($\varepsilon$) and cross sections ($\sigma$) in $E_\gamma$ for 2016 dataset.

| $E_\gamma$ (GeV) | $N_{MC}$ | $N_{Data}$ | $\varepsilon$ (%) | $\sigma$ (nb) |
|---|---|---|---|---|
| 6.50 - 7.01 | 1839 ± 51 | 588 ± 40 | 6.90 ± 0.19 | 65.63 ± 4.48 ± 2.14 |
| 7.01 - 7.52 | 3406 ± 69 | 590 ± 40 | 6.88 ± 0.14 | 60.48 ± 4.12 ± 4.34 |
| 7.52 - 8.03 | 5952 ± 98 | 1049 ± 54 | 7.31 ± 0.12 | 67.24 ± 3.45 ± 2.97 |
| 8.03 - 8.54 | 23186 ± 183 | 2229 ± 80 | 7.98 ± 0.06 | 55.12 ± 1.98 ± 1.72 |
| 8.54 - 9.05 | 47841 ± 247 | 3830 ± 100 | 8.17 ± 0.04 | 51.02 ± 1.34 ± 2.15 |
| 9.05 - 9.56 | 9415 ± 125 | 828 ± 51 | 8.03 ± 0.11 | 52.50 ± 3.23 ± 1.51 |
| 9.56 - 10.07 | 11060 ± 127 | 1067 ± 54 | 8.18 ± 0.09 | 51.33 ± 2.59 ± 1.35 |
| 10.07 - 10.58 | 12474 ± 132 | 1116 ± 55 | 7.97 ± 0.08 | 51.77 ± 2.54 ± 1.61 |
| 10.58 - 11.09 | 10958 ± 124 | 935 ± 50 | 7.96 ± 0.09 | 53.20 ± 2.84 ± 2.32 |
| 11.09 - 11.60 | 15368 ± 141 | 1007 ± 54 | 8.02 ± 0.07 | 41.92 ± 2.23 ± 1.65 |

Table 4.5: $\phi\pi^+\pi^-$ yields in MC ($N_{MC}$) and data ($N_{Data}$), efficiencies ($\varepsilon$) and cross sections ($\sigma$) in -$t$ for 2016 dataset.

| -t $(GeV/c)^2$ | $N_{MC}$ | $N_{Data}$ | $\varepsilon$ (%) | $\sigma$ (nb) |
|---|---|---|---|---|
| 0.00 - 0.40 | 26291 ± 192 | 2593 ± 96 | 5.57 ± 0.04 | 14.77 ± 0.55 ± 0.53 |
| 0.40 - 0.80 | 40108 ± 239 | 4758 ± 110 | 8.88 ± 0.05 | 17.00 ± 0.39 ± 0.41 |
| 0.80 - 1.20 | 28242 ± 197 | 3255 ± 87 | 9.23 ± 0.06 | 11.19 ± 0.30 ± 0.44 |
| 1.20 - 1.60 | 17977 ± 159 | 2186 ± 70 | 9.04 ± 0.08 | 7.67 ± 0.25 ± 0.19 |
| 1.60 - 2.00 | 11562 ± 126 | 1320 ± 55 | 9.06 ± 0.10 | 4.62 ± 0.19 ± 0.17 |
| 2.00 - 2.40 | 6855 ± 97 | 751 ± 43 | 8.51 ± 0.12 | 2.80 ± 0.16 ± 0.14 |
| 2.40 - 2.80 | 4248 ± 74 | 468 ± 35 | 8.34 ± 0.15 | 1.78 ± 0.13 ± 0.11 |
| 2.80 - 3.20 | 2510 ± 59 | 312 ± 30 | 7.93 ± 0.19 | 1.25 ± 0.12 ± 0.06 |
| 3.20 - 3.60 | 1623 ± 46 | 159 ± 22 | 8.09 ± 0.23 | 0.63 ± 0.09 ± 0.06 |
| 3.60 - 4.00 | 891 ± 34 | 128 ± 21 | 7.29 ± 0.28 | 0.56 ± 0.09 ± 0.09 |

Table 4.6: $\phi\pi^+\pi^-$ yields in MC ($N_{MC}$) and data ($N_{Data}$), efficiencies ($\varepsilon$) and cross sections ($\sigma$) in $E_\gamma$ for 2017 dataset.

| $E_\gamma$ (GeV) | $N_{MC}$ | $N_{Data}$ | $\varepsilon$ (%) | $\sigma$ (nb) |
|---|---|---|---|---|
| 6.50 - 7.01 | 7469 ± 101 | 4791 ± 112 | 2.90 ± 0.04 | 96.14 ± 2.25 ± 2.59 |
| 7.01 - 7.52 | 9877 ± 121 | 5505 ± 124 | 3.24 ± 0.04 | 89.69 ± 2.02 ± 2.14 |
| 7.52 - 8.03 | 34681 ± 239 | 15112 ± 210 | 3.49 ± 0.02 | 83.52 ± 1.16 ± 2.68 |
| 8.03 - 8.54 | 71072 ± 322 | 24142 ± 261 | 3.80 ± 0.02 | 79.73 ± 0.86 ± 2.67 |
| 8.54 - 9.05 | 65893 ± 301 | 19915 ± 237 | 3.93 ± 0.02 | 76.39 ± 0.91 ± 1.98 |
| 9.05 - 9.56 | 24954 ± 194 | 8237 ± 154 | 4.02 ± 0.03 | 78.13 ± 1.46 ± 2.56 |
| 9.56 - 10.07 | 33567 ± 217 | 9743 ± 167 | 4.08 ± 0.03 | 70.16 ± 1.20 ± 2.11 |
| 10.07 - 10.58 | 32601 ± 215 | 8299 ± 157 | 4.19 ± 0.03 | 69.73 ± 1.32 ± 2.28 |
| 10.58 - 11.09 | 40464 ± 236 | 9631 ± 167 | 4.28 ± 0.02 | 65.15 ± 1.13 ± 1.88 |
| 11.09 - 11.60 | 18492 ± 154 | 3101 ± 95 | 4.40 ± 0.04 | 59.28 ± 1.82 ± 1.66 |

Table 4.7: $\phi\pi^+\pi^-$ yields in MC ($N_{MC}$) and data ($N_{Data}$), efficiencies ($\varepsilon$) and cross sections ($\sigma$) in -$t$ for 2017 dataset.

| -t $(GeV/c)^2$ | $N_{MC}$ | $N_{Data}$ | $\varepsilon$ (%) | $\sigma$ (nb) |
|---|---|---|---|---|
| 0.00 - 0.40 | 81182 ± 351 | 19995 ± 273 | 3.63 ± 0.02 | 14.94 ± 0.20 ± 0.38 |
| 0.40 - 0.80 | 109014 ± 393 | 35122 ± 309 | 4.95 ± 0.02 | 19.22 ± 0.17 ± 0.46 |
| 0.80 - 1.20 | 65924 ± 304 | 24860 ± 245 | 4.33 ± 0.02 | 15.56 ± 0.15 ± 0.52 |
| 1.20 - 1.60 | 36291 ± 229 | 15695 ± 192 | 3.60 ± 0.02 | 11.79 ± 0.14 ± 0.50 |
| 1.60 - 2.00 | 21377 ± 174 | 9238 ± 151 | 3.26 ± 0.03 | 7.67 ± 0.13 ± 0.36 |
| 2.00 - 2.40 | 12172 ± 132 | 5702 ± 122 | 2.87 ± 0.03 | 5.38 ± 0.11 ± 0.30 |
| 2.40 - 2.80 | 6790 ± 99 | 3543 ± 98 | 2.51 ± 0.04 | 3.82 ± 0.11 ± 0.16 |
| 2.80 - 3.20 | 3953 ± 76 | 2330 ± 82 | 2.28 ± 0.04 | 2.76 ± 0.10 ± 0.18 |
| 3.20 - 3.60 | 2304 ± 56 | 1476 ± 67 | 2.10 ± 0.05 | 1.91 ± 0.09 ± 0.15 |
| 3.60 - 4.00 | 1347 ± 44 | 1063 ± 58 | 1.91 ± 0.06 | 1.51 ± 0.08 ± 0.10 |

Table 4.8: $\phi\pi^+\pi^-$ yields in MC ($N_{MC}$) and data ($N_{Data}$), efficiencies ($\varepsilon$) and cross sections ($\sigma$) in $E_\gamma$ for Spring 2018 dataset.

| $E_\gamma$ (GeV) | $N_{MC}$ | $N_{Data}$ | $\varepsilon$ (%) | $\sigma$ (nb) |
|---|---|---|---|---|
| 6.50 - 7.01 | 5512 ± 89 | 8203 ± 160 | 2.28 ± 0.04 | 72.20 ± 1.41 ± 1.69 |
| 7.01 - 7.52 | 7441 ± 105 | 9221 ± 173 | 2.58 ± 0.04 | 65.15 ± 1.22 ± 1.25 |
| 7.52 - 8.03 | 26267 ± 208 | 26104 ± 292 | 2.74 ± 0.02 | 64.71 ± 0.72 ± 1.26 |
| 8.03 - 8.54 | 56031 ± 281 | 38176 ± 347 | 3.05 ± 0.02 | 57.99 ± 0.53 ± 1.48 |
| 8.54 - 9.05 | 56863 ± 283 | 35720 ± 333 | 3.25 ± 0.02 | 55.50 ± 0.52 ± 1.47 |
| 9.05 - 9.56 | 18752 ± 173 | 13843 ± 215 | 3.33 ± 0.03 | 54.50 ± 0.85 ± 1.65 |
| 9.56 - 10.07 | 26379 ± 199 | 17460 ± 235 | 3.47 ± 0.03 | 50.93 ± 0.69 ± 1.58 |
| 10.07 - 10.58 | 25829 ± 198 | 14090 ± 216 | 3.59 ± 0.03 | 47.40 ± 0.73 ± 1.91 |
| 10.58 - 11.09 | 33036 ± 213 | 17359 ± 234 | 3.78 ± 0.02 | 44.68 ± 0.60 ± 2.07 |
| 11.09 - 11.60 | 14387 ± 137 | 5906 ± 135 | 3.87 ± 0.04 | 43.80 ± 1.00 ± 1.78 |

Table 4.9: $\phi\pi^+\pi^-$ yields in MC ($N_{MC}$) and data ($N_{Data}$), efficiencies ($\varepsilon$) and cross sections ($\sigma$) in -$t$ for Spring 2018 dataset.

| -t $(GeV/c)^2$ | $N_{MC}$ | $N_{Data}$ | $\varepsilon$ (%) | $\sigma$ (nb) |
|---|---|---|---|---|
| 0.00 - 0.40 | 75845 ± 334 | 44569 ± 424 | 3.24 ± 0.01 | 12.97 ± 0.12 ± 0.50 |
| 0.40 - 0.80 | 86033 ± 350 | 60630 ± 418 | 3.87 ± 0.02 | 14.78 ± 0.10 ± 0.43 |
| 0.80 - 1.20 | 49379 ± 263 | 37272 ± 311 | 3.35 ± 0.02 | 10.49 ± 0.09 ± 0.25 |
| 1.20 - 1.60 | 27246 ± 197 | 22620 ± 241 | 2.92 ± 0.02 | 7.29 ± 0.08 ± 0.16 |
| 1.60 - 2.00 | 15196 ± 147 | 13324 ± 188 | 2.62 ± 0.03 | 4.78 ± 0.07 ± 0.12 |
| 2.00 - 2.40 | 8339 ± 108 | 8164 ± 151 | 2.35 ± 0.03 | 3.27 ± 0.06 ± 0.08 |
| 2.40 - 2.80 | 4656 ± 81 | 4771 ± 123 | 2.14 ± 0.04 | 2.11 ± 0.05 ± 0.06 |
| 2.80 - 3.20 | 2453 ± 58 | 3156 ± 103 | 1.85 ± 0.04 | 1.61 ± 0.05 ± 0.06 |
| 3.20 - 3.60 | 1322 ± 42 | 1918 ± 86 | 1.65 ± 0.05 | 1.10 ± 0.05 ± 0.04 |
| 3.60 - 4.00 | 719 ± 31 | 1179 ± 76 | 1.49 ± 0.06 | 0.75 ± 0.05 ± 0.05 |

Table 4.10: $\phi\pi^+\pi^-$ yields in MC ($N_{MC}$) and data ($N_{Data}$), efficiencies ($\varepsilon$) and cross sections ($\sigma$) in $E_\gamma$ for Fall 2018 dataset.

| $E_\gamma$ (GeV) | $N_{MC}$ | $N_{Data}$ | $\varepsilon$ (%) | $\sigma$ (nb) |
|---|---|---|---|---|
| 6.50 - 7.01 | 14531 ± 144 | 12668 ± 189 | 4.91 ± 0.05 | 70.88 ± 1.06 ± 1.99 |
| 7.01 - 7.52 | 16340 ± 157 | 13202 ± 194 | 5.33 ± 0.05 | 70.10 ± 1.03 ± 1.57 |
| 7.52 - 8.03 | 52390 ± 282 | 36354 ± 329 | 5.70 ± 0.03 | 67.51 ± 0.61 ± 1.49 |
| 8.03 - 8.54 | 102113 ± 384 | 57786 ± 412 | 6.10 ± 0.02 | 64.29 ± 0.46 ± 1.22 |
| 8.54 - 9.05 | 101185 ± 369 | 48509 ± 369 | 6.28 ± 0.02 | 63.72 ± 0.48 ± 1.06 |
| 9.05 - 9.56 | 35097 ± 232 | 19732 ± 239 | 6.57 ± 0.04 | 62.69 ± 0.76 ± 1.19 |
| 9.56 - 10.07 | 48747 ± 261 | 25116 ± 263 | 6.66 ± 0.04 | 59.46 ± 0.62 ± 1.18 |
| 10.07 - 10.58 | 45465 ± 252 | 20185 ± 239 | 6.84 ± 0.04 | 57.91 ± 0.69 ± 1.24 |
| 10.58 - 11.09 | 55880 ± 272 | 24692 ± 258 | 6.97 ± 0.03 | 54.52 ± 0.57 ± 1.15 |
| 11.09 - 11.60 | 27397 ± 186 | 8996 ± 155 | 7.24 ± 0.05 | 51.79 ± 0.89 ± 1.41 |

Table 4.11: $\phi\pi^+\pi^-$ yields in MC ($N_{MC}$) and data ($N_{Data}$), efficiencies ($\varepsilon$) and cross sections ($\sigma$) in -$t$ for Fall 2018 dataset.

| -t $(GeV/c)^2$ | $N_{MC}$ | $N_{Data}$ | $\varepsilon$ (%) | $\sigma$ (nb) |
|---|---|---|---|---|
| 0.00 - 0.40 | 115135 ± 411 | 51942 ± 430 | 5.42 ± 0.02 | 13.96 ± 0.12 ± 0.36 |
| 0.40 - 0.80 | 149523 ± 460 | 80765 ± 463 | 7.12 ± 0.02 | 16.52 ± 0.09 ± 0.23 |
| 0.80 - 1.20 | 94271 ± 368 | 55187 ± 363 | 6.97 ± 0.03 | 11.54 ± 0.08 ± 0.21 |
| 1.20 - 1.60 | 56537 ± 279 | 34861 ± 288 | 6.49 ± 0.03 | 7.83 ± 0.06 ± 0.16 |
| 1.60 - 2.00 | 34580 ± 220 | 21177 ± 228 | 6.18 ± 0.04 | 5.00 ± 0.05 ± 0.11 |
| 2.00 - 2.40 | 21262 ± 171 | 12579 ± 182 | 5.90 ± 0.05 | 3.11 ± 0.04 ± 0.09 |
| 2.40 - 2.80 | 13154 ± 135 | 7804 ± 148 | 5.64 ± 0.06 | 2.02 ± 0.04 ± 0.06 |
| 2.80 - 3.20 | 7799 ± 104 | 5224 ± 125 | 5.19 ± 0.07 | 1.47 ± 0.04 ± 0.06 |
| 3.20 - 3.60 | 4662 ± 81 | 3324 ± 106 | 4.78 ± 0.08 | 1.01 ± 0.03 ± 0.05 |
| 3.60 - 4.00 | 2800 ± 62 | 2383 ± 92 | 4.50 ± 0.10 | 0.77 ± 0.03 ± 0.04 |

### 4.4.2 Upper Limit for $\gamma p \to Y(2175)p \to \phi\pi^+\pi^- p$

In the following, we will study the resonant mode of the previous reaction, with the $Y(2175) \to \phi\pi^+\pi^-$ being produced as an intermediate resonance. First, we select $\phi\pi^+\pi^-$ signal, by subtracting non-$\phi(1020)$ background. To achieve this, we study the invariant mass correlation between $K^+K^-$ and $K^+K^-\pi^+\pi^-$, seen in Fig. 4.23. Next to the clear horizontal band of the $\phi(1020)$, we see another diagonal band of correlated events. The latter is investigated by performing a one dimensional projection of 50 intervals of $K^+K^-\pi^+\pi^-$ on the $K^+K^-$ invariant mass. The yields of $\phi\pi^+\pi^-$ are then extracted after fitting the signal and background shapes as shown in Fig. 4.24. The resulting $K^+K^-\pi^+\pi^-$ invariant mass after background subtraction (Fig. 4.25) shows no enhancement around 2175 GeV/c$^2$, leading to the non observation of $Y(2175)$ resonance in the $\phi\pi^+\pi^-$ channel.

In the absence of a signal, limits can be set on the the $\gamma p \to Y(2175)p \to \phi\pi^+\pi^- p$ production cross section. We define an upper limit at 90% Confidence Level (CL) using the maximum likelihood method. For $n$ independent measurements of the cross section $\sigma_i$, following a probability density function $f(\sigma_i;\sigma)$ with the cross section ($\sigma$) as a parameter, the likelihood function is obtained from the probability of the data under assumption of the parameters defined as

$$\mathcal{L}(\sigma) = \prod_{n}^{i=1} f(\sigma_i;\sigma) \ . \tag{4.12}$$

The maximum likelihood estimator for $\sigma$ is defined as the values that give the maximum of $\mathcal{L}(\sigma)$. The upper limit ($UL_{90}$) is the cross section at 90% of the profile likelihood distribution, with

$$\int_0^{UL_{90}} \mathcal{L}(\sigma)\ d\sigma = 0.9 \tag{4.13}$$

In this case, the Bayesian approach is used, for which a prior knowledge on the

signal cross section is expressed in the sense that a probability for a negative cross section is negligible for real physics processes.

After fixing the $Y(2175)$ signal shape from MC simulation as shown in Fig. 4.26, we use the same fit parameters to fit the data, see Fig. 4.27. The negative yield extracted from these plots are due to the dips around the Y(2175) mass, which may be due to simple statistical fluctuations or even destructive interference between the resonances participating in this process. We perform multiple fits, varying the signal amplitude parameter around the nominal value by five times the statistical uncertainty on the yield, and extract the profile likelihoods for each variation, as displayed in Fig 4.28. In this case, the Likelihood profiles essentially follow Gaussian distributions, so that the mean can be taken as the nominal cross section that maximizes the likelihood, and the standard deviation as the error on the cross section measurement. To take into account the effect of the cross section systematic errors on the upper limit determination, discussed in Sec. 4.5, we convolute the obtained likelihood profile distribution with a gaussian function of the same mean and the standard deviation corresponding to the systematic uncertainty. The resulting convolution (Fig 4.29) is a gaussian with the nominal cross section given by the mean and the total error (quadratic sum of the statistical and systematic error) given by the standard deviation. The CL corresponds to 90th percentile of the convoluted distribution above zero. The constructed Bayesian Confidence interval should represent a 90% probability to cover the true value of the cross section. This technique is applied for the different datasets, and the results are summarized in the Tab. 4.12.

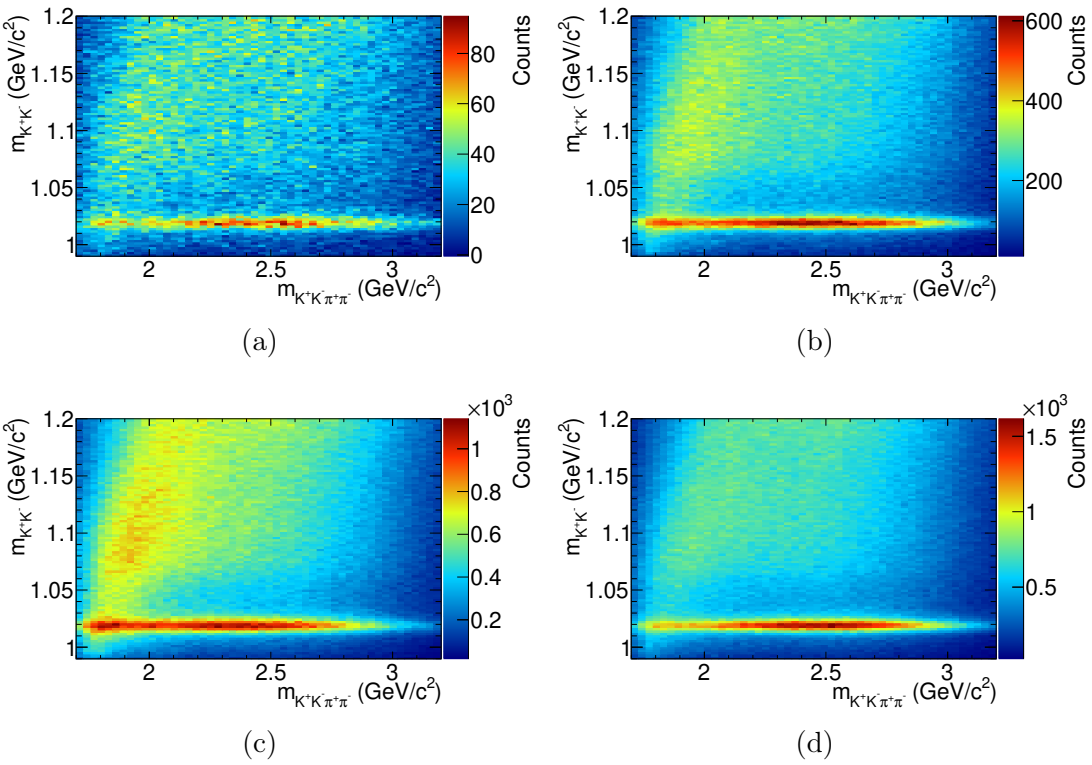


Figure 4.23: $K^+K^-$ versus $K^+K^-\pi^+\pi^-$ invariant mass for (a) 2016, (b) 2017, (c) Spring 2018 and (d) Fall 2018 datasets.

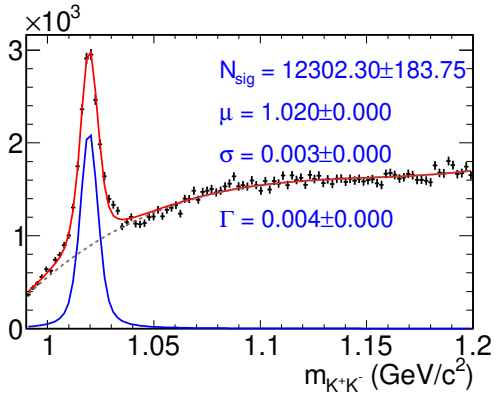


Figure 4.24: Invariant mass of $K^+K^-$ of one projection of $K^+K^-\pi^+\pi^-$ invariant mass. The total fit (red) is composed of signal shape (blue) described by Eq. 4.5 and background (dashed) by polynomial of $4^{th}$ degree.

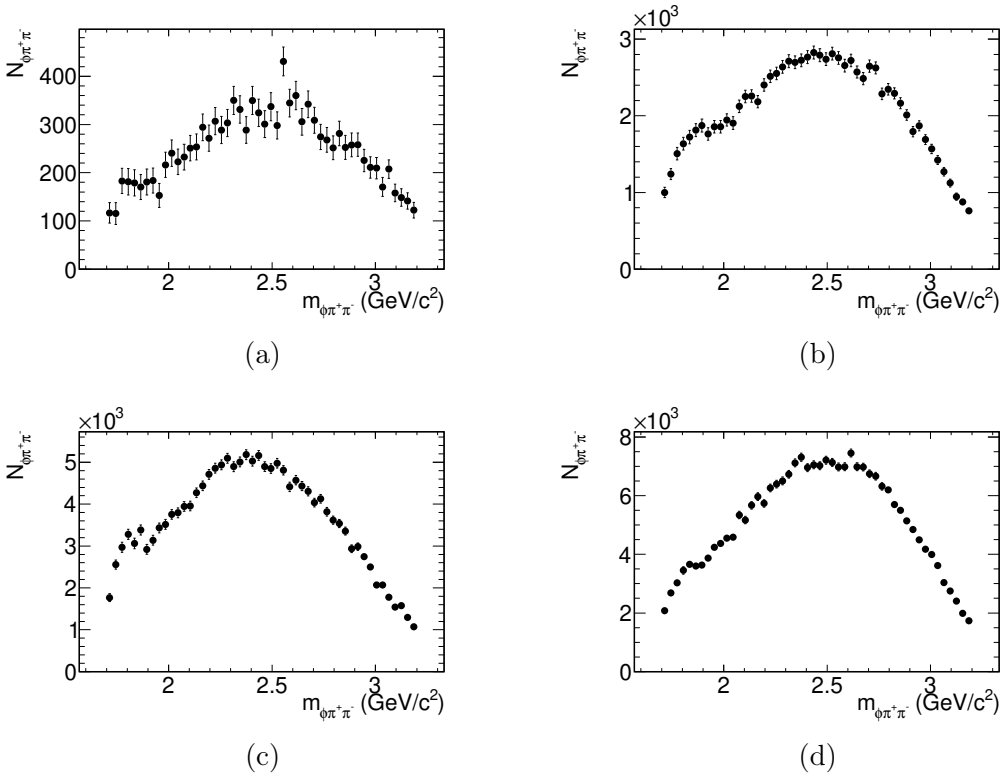


Figure 4.25: The yields $\phi\pi^+\pi^-$ versus $K^+K^-\pi^+\pi^-$ invariant mass for (a) 2016, (b) 2017, (c) Spring 2018 and (d) Fall 2018 datasets. No observation of the $Y(2175)$ in all the four datasets.

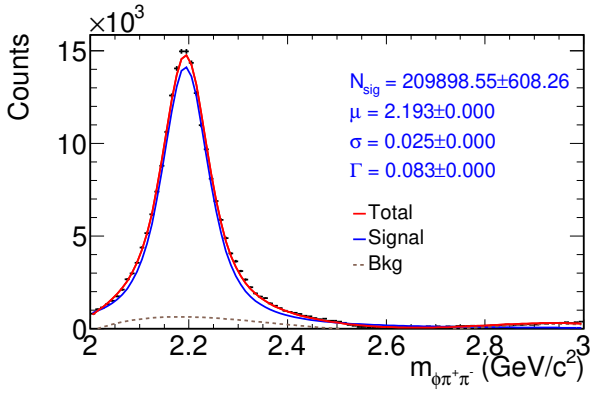


Figure 4.26: Invariant mass of $\phi\pi^+\pi^-$ in MC simulation. The total fit (red) is composed of signal shape (blue) described by Eq. 4.5 and background (dashed) by polynomial of $4^{th}$ degree.

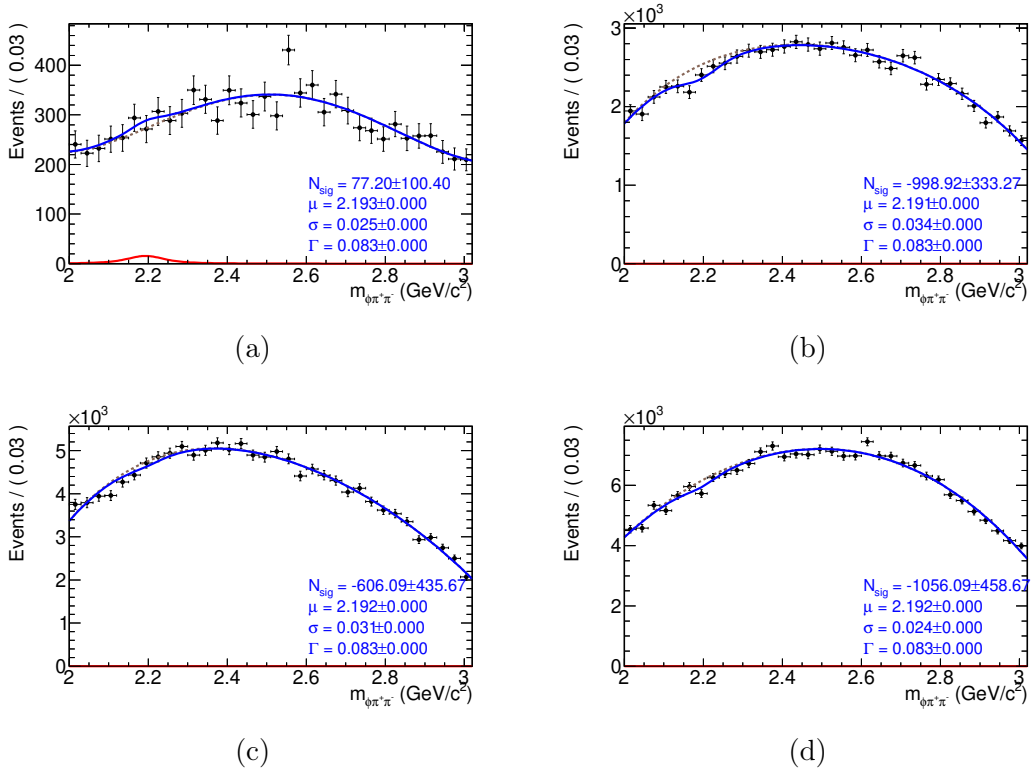


Figure 4.27: The yields of $\phi\pi^+\pi^-$ versus $K^+K^-\pi^+\pi^-$ invariant mass for (a) 2016, (b) 2017, (c) Spring 2018 and (d) Fall 2018 datasets. The fit models and parameters are obtained from Fig. 4.26.

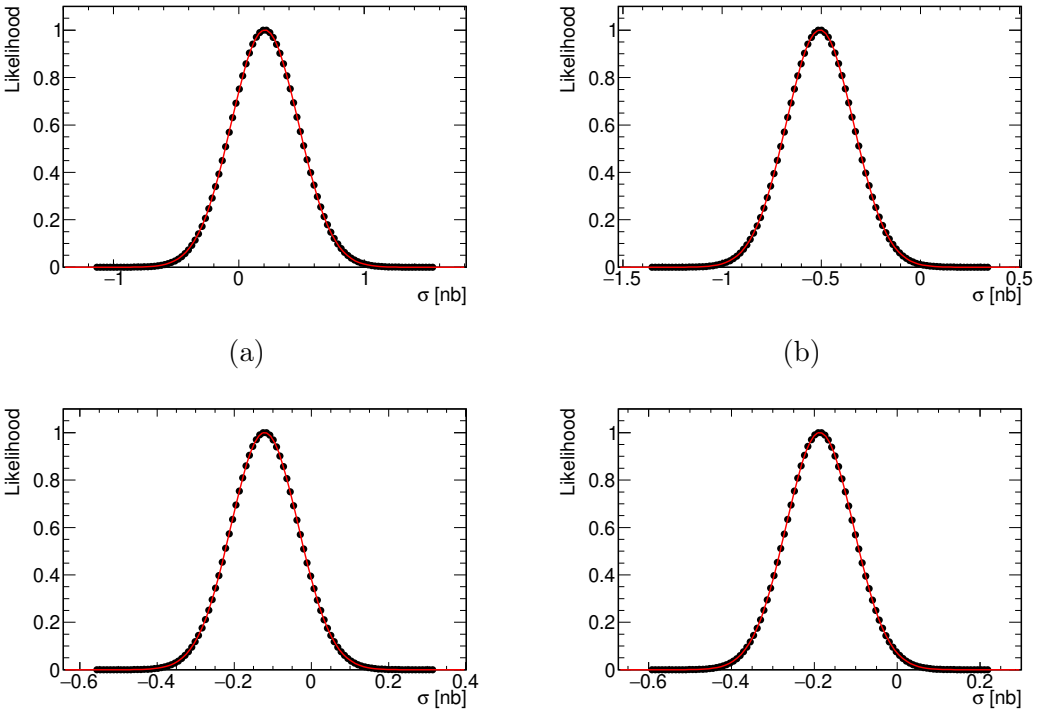


Figure 4.28: Profile likelihood versus total cross section for (a) 2016, (b) 2017, (c) Spring 2018 and (d) Fall 2018 datasets.

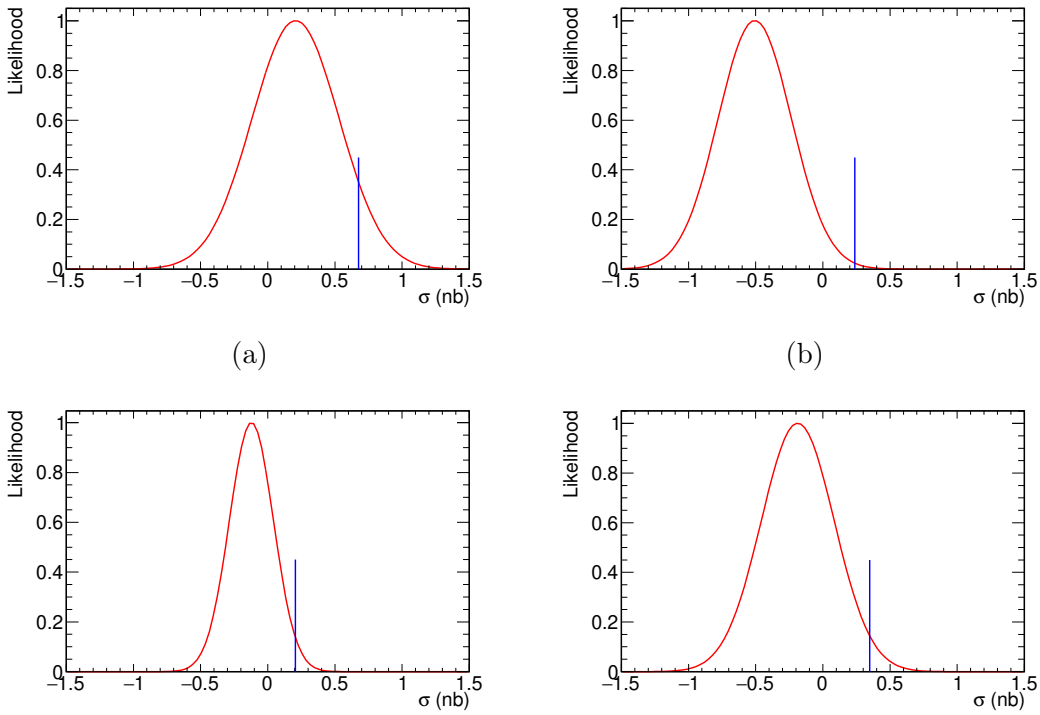


(a) (b)

(c) (d)

Figure 4.29: Convoluted profile likelihood and a gaussian with the nominal cross section as mean and total errors as standard deviation versus total cross section for (a) 2016, (b) 2017, (c) Spring 2018 and (d) Fall 2018 datasets. The vertical blue lines are indicating the cross section upper limit at 90% CL.

Table 4.12: Total cross sections and upper limits for $\gamma p \to Y(2175)p \to \phi\pi^+\pi^- p$.

| Dataset | $N_{measured}$ | $\varepsilon$ (%) | $\sigma$ (nb) x BR$[Y(2175) \to \phi\pi^+\pi^-]$ | Upper Limit 90% CL (nb) |
|---|---|---|---|---|
| 2016 | 77 ± 100 | 11.89 ± 0.034 | 0.21 ± 0.27 ± 0.18 | 0.68 |
| 2017 | -999 ± 333 | 5.33 ± 0.013 | -0.51 ± 0.17 ± 0.21 | 0.24 |
| Spring 2018 | -606 ± 436 | 4.72 ± 0.012 | -0.12 ± 0.09 ± 0.14 | 0.21 |
| Fall 2018 | -1056 ± 459 | 8.24 ± 0.014 | -0.19 ± 0.08 ± 0.26 | 0.35 |

### 4.4.3 Cross Section for $\gamma p \to \phi f_0 p$

This section summarizes the study of the non-resonant (*i.e.* without the $Y(2175)$) production of the $\phi f_0 p$ final state. The $\phi(1020)\pi^+\pi^-$ signal yields are extracted by fitting the $K^+K^-$ invariant-mass projections in each 0.018 GeV/c$^2$ interval of $\pi^+\pi^-$ invariant mass. The invariant mass correlation between the $K^+K^-$ and the $\pi^+\pi^-$ pairs is shown in Fig. 4.30. The $f_0(980)$ signal shape is well described by the Breit-Wigner model in MC simulation (Fig. 4.31), and the signal yield obtained is used for the reconstruction efficiency calculation.

An observation of the $f_0(980)$ resonance is clearly seen in the data (Fig. 4.32), with the parameters consistent with the PDG data values for this meson. Furthermore, an enhancement near the $\rho(770)$ and $K_s^0$ mesons are seen near the nominal masses. The $K_s^0$ is produced in a displaced vertex, leading to yield reductions due to the primary vertex constraint in the kinematic fitting procedure. The cross section of the $\gamma p \to \phi f_0 p$ is calculated using Eq. 4.8, and the results are summarized in Tab. 4.13. The cross sections for all the datasets are consistent within errors.

Table 4.13: A summary of the total cross section and efficiency for $\gamma p \to \phi f_0 p$. The statistical and systematics errors are displayed for the cross section. The systematic uncertainties will be discussed in Sec. 4.5

| Dataset | $N_{measured}$ | $\varepsilon$ (%) | $\sigma \times$ BR$[f_0(980) \to \pi^+\pi^-]$ (nb) |
|---|---|---|---|
| 2016 | 596 $\pm$ 125 | 0.72 $\pm$ 0.01 | 26.18 $\pm$ 5.51 $\pm$ 3.22 |
| 2017 | 2188 $\pm$ 695 | 0.26 $\pm$ 0.01 | 22.67 $\pm$ 7.20 $\pm$ 3.18 |
| Spring 2018 | 5023 $\pm$ 1384 | 0.23 $\pm$ 0.02 | 20.61 $\pm$ 5.68 $\pm$ 1.05 |
| Fall 2018 | 4400 $\pm$ 859 | 0.48 $\pm$ 0.01 | 12.51 $\pm$ 2.44 $\pm$ 1.44 |

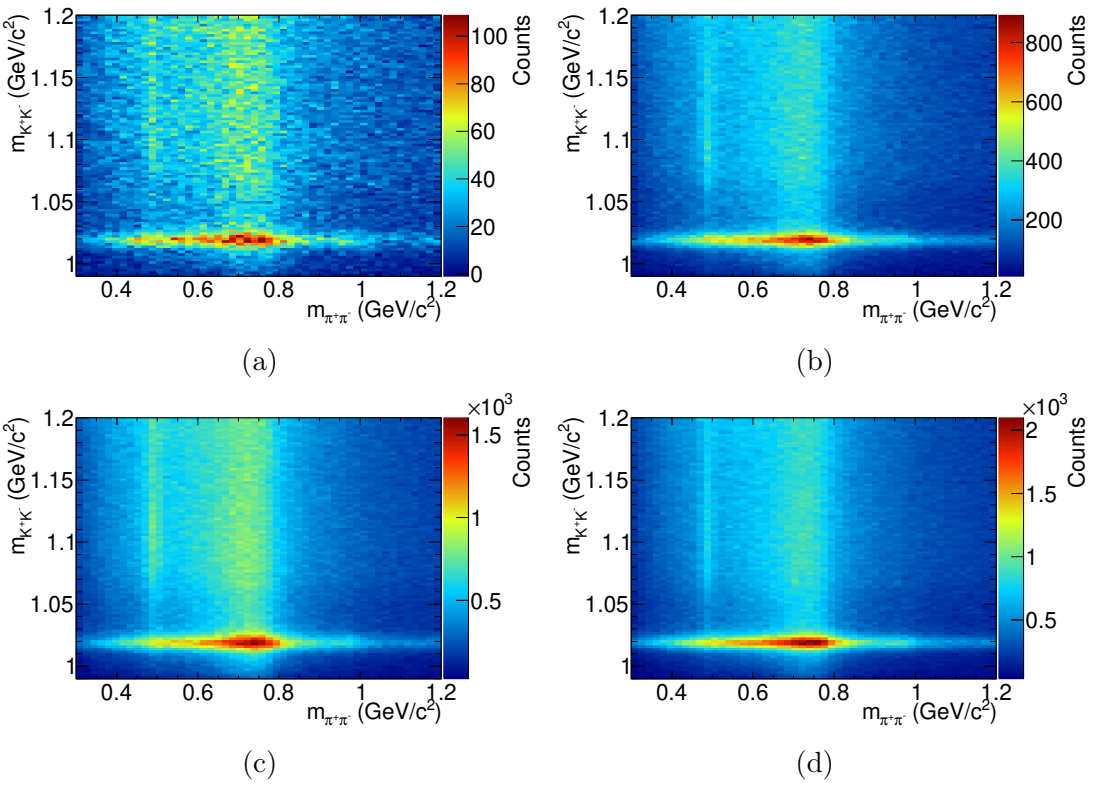


Figure 4.30: $K^+K^-$ versus $\pi^+\pi^-$ invariant mass for (a) 2016, (b) 2017, (c) Spring 2018 and (d) Fall 2018 datasets. The horizontal band corresponds to the $\phi(1020)$ and the vertical two bands to the $\rho(770)$ and $K^0_s$.

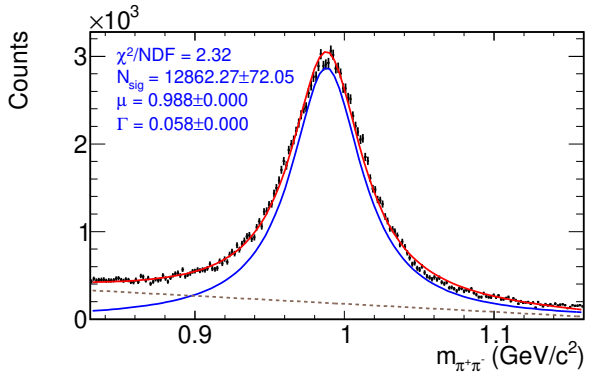


Figure 4.31: Invariant mass of $\pi^+\pi^-$ in MC simulation. The total fit (red) is composed of signal shape (blue) described by a Breit-Wigner and a background (dashed) by polynomial of first degree.

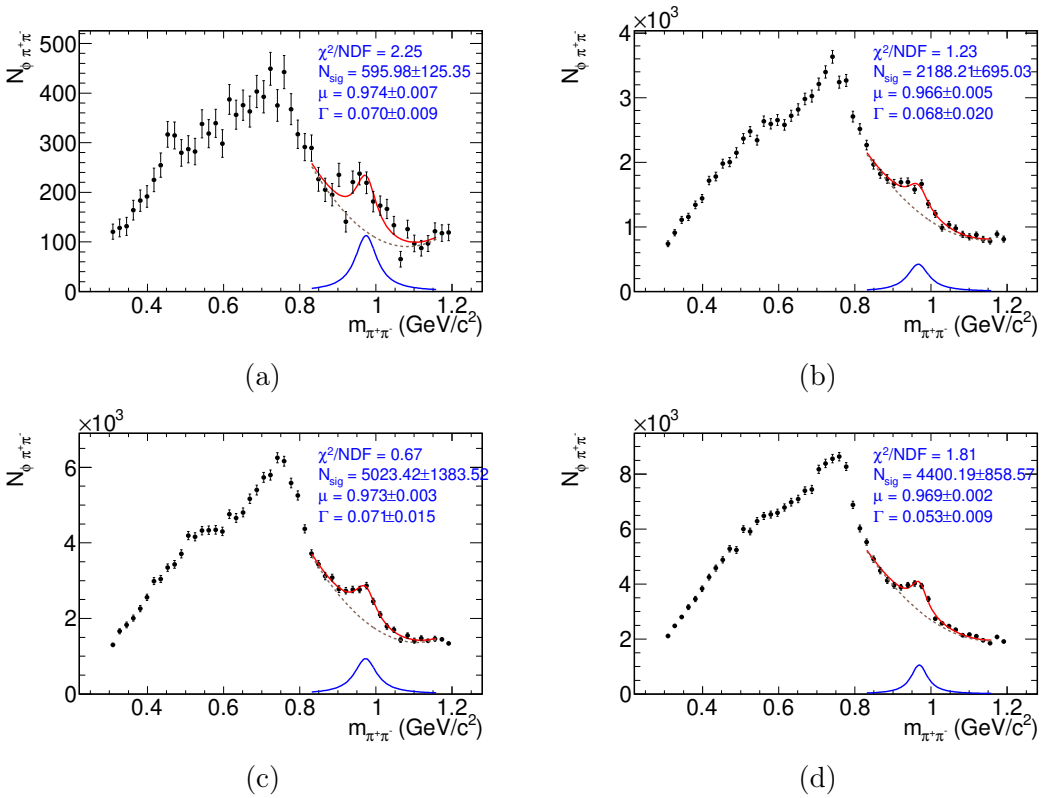


Figure 4.32: The yields of $\phi\pi^+\pi^-$ versus $\pi^+\pi^-$ invariant mass for (a) 2016, (b) 2017, (c) Spring 2018 and (d) Fall 2018 datasets. The total fit (blue) is composed of the signal (red) described by a Breit-Wigner and the background (dashed) described by a second order polynomial.

### 4.4.4 Upper Limit for $\gamma p \to Y(2175)p \to \phi f_0 p$

Following a similar procedure as in Sec. 4.4.2 to reduce the non-$\phi(1020)$ background, we obtain the $\phi f_0$ yields by fitting the $K^+K^-$ invariant-mass projections in each 0.02 GeV/c$^2$ interval of $K^+K^-\pi^+\pi^-$ invariant mass, while requiring the di-pion mass pair within 2.5 times the PDG average mass error of $f_0(980)$. The resulting $K^+K^-\pi^+\pi^-$ invariant-mass distribution for $\phi f_0$ candidate events is shown in Fig. 4.33. To estimate the $Y(2175)$ contribution within multiple fluctuations in the invariant mass distribution, the likelihood ratio test [46] is used to determine the significance of the $Y(2175)$ signal. The binned maximum likelihood fits are used for this test.

We define the null hypothesis $H_0$ as the condition, in which only the background is observed in the data, and the alternative hypotheses $H_1$, in which both signal and background are modeled in data. According to Wilks theorem [47], the significance ($Z$) adopted as the test statistics is asymptotically distributed according to the $\chi^2$ function, with degrees of freedom equal to the difference between the number of fit parameters. The goal of the profile likelihood ratio in this study is to quantify degree of compatibility (or not) of the data with the hypothesis of the $Y(2175)$ signal being present, which would lead to an observation ($Z \geq 5\sigma$), evidence ($3\sigma < Z < 5\sigma$) or none of both ($Z < 3\sigma$). In the case of one degree of freedom difference between the two hypothesis, the significance is defined as

$$Z = \sqrt{-2\ ln\left(\frac{\mathcal{L}(H_0)}{\mathcal{L}(H_1)}\right)}\ , \tag{4.14}$$

After describing the $Y(2175)$ signal shape in MC simulation, the same parameters are fixed in the data and the signal amplitude is set as a free parameter, once with the signal and background fit to obtain the likelihood $\mathcal{L}(H_1)$, and the second with only the background to obtain $\mathcal{L}(H_0)$. The significance is then calculated

using Eq. 4.14; it is displayed next to the fit parameterization in Fig. 4.33. To estimate the goodness of the fit model to the data, we use the pull distribution, which is defined as the difference between the data and the fit values divided by the data errors. The pull histogram is distributed as a standard Gaussian with a mean of zero and a unit width. If the mean is not centered at zero than there is a bias in the fit model (Fig. 4.33). An enhancement around 2.191 GeV/c$^2$ is observed, with mean and width consistent with the PDG data for the $Y(2175)$. This resonance is seen in both, the largest data samples of Spring and Fall 2018 datasets, with a significance above $3\sigma$. Despite the enhancement around the mass of interest, we could not claim an observation of the $Y(2175)$ due to systematic and statistical limitations, and to the strong bias in the fits especially at the region of interest. For this reason, we set a 90% CL upper limit on the $\gamma p \to Y(2175)p \to \phi f_0 p$ cross section, using the method in Sec. 4.4.2. The resulting profile likelihoods indicating the upper limits are shown in Fig. 4.34. The summary of the efficiency, cross section and the upper limit values are listed in Tab.4.14.

Table 4.14: Summary of efficiency, cross section, and upper limit for different datasets.

| Data set | $N_{measured}$ | $\varepsilon$ [%] | $\sigma \times BR_{f_0\to\pi^+\pi^-} \times BR_{Y\to\phi f_0}$ [nb] | Upper Limit 90% CL (nb) |
|---|---|---|---|---|
| 2016 | $8 \pm 40$ | 12.70 | $0.02 \pm 0.10 \pm 0.16$ | 0.33 |
| 2017 | $112 \pm 116$ | 5.25 | $0.06 \pm 0.06 \pm 0.26$ | 0.48 |
| Spring 2018 | $773 \pm 156$ | 4.90 | $0.15 \pm 0.03 \pm 0.19$ | 0.43 |
| Fall 2018 | $573 \pm 175$ | 9.23 | $0.09 \pm 0.03 \pm 0.20$ | 0.39 |

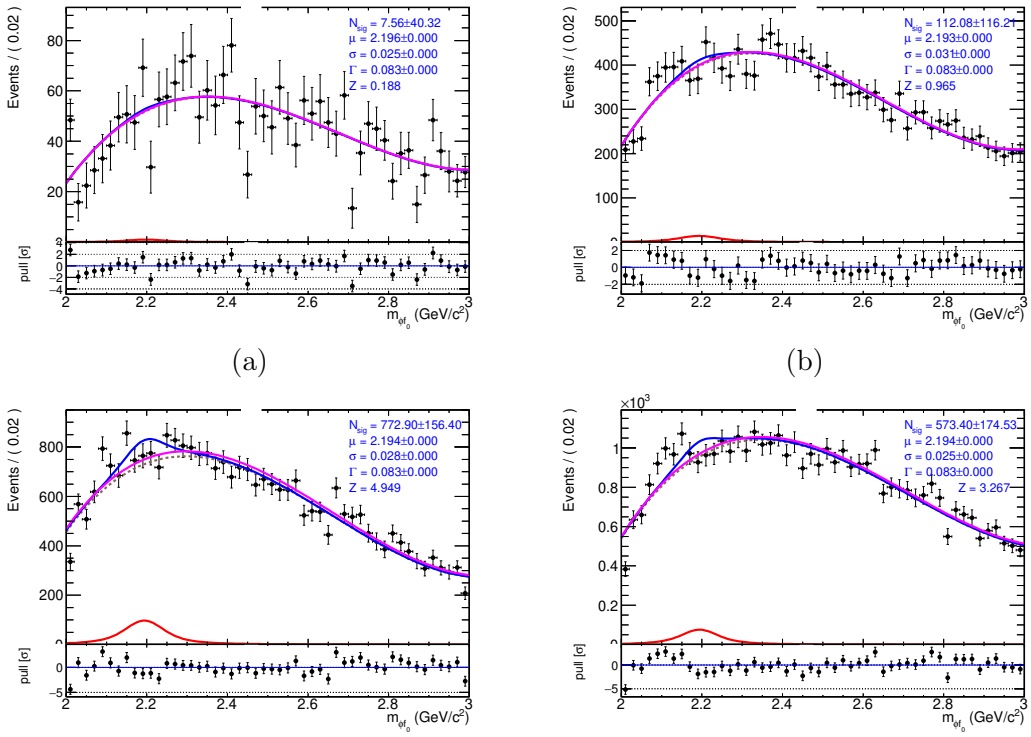


Figure 4.33: The invariant mass distribution for $\phi f_0$ candidates for (a) 2016, (b) 2017, (c) Spring 2018 and (d) Fall 2018 datasets. The total fit (blue) is composed of the signal (red) described by a Voigtian and the background (dashed) with a third degree Chebyshev polynomial. The total fit (magenta) is performed with only the background. A pull distribution is shown in the bottom of each plot.

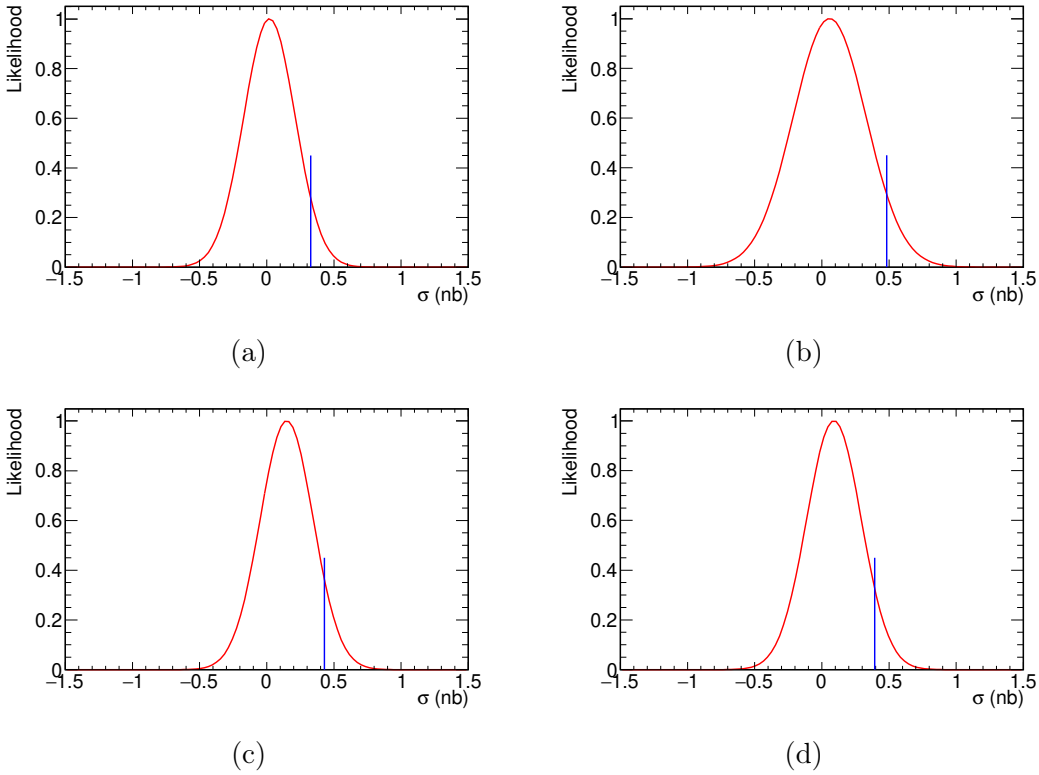


Figure 4.34: Convoluted profile likelihood and a gaussian with the nominal cross section as mean and total errors as standard deviation versus total cross section for (a) 2016, (b) 2017, (c) Spring 2018 and (d) Fall 2018 datasets. The vertical blue lines are indicating the cross section upper limit at 90% CL.

## 4.5 Systematic Uncertainties

In order to determine the systematic errors, multiple variations in the analysis chain are tested, resulting in a different cross section measurements around the nominal value. The relative amount of deviation from the nominal cross section measurement are identified using the sample standard deviation defined as

$$\delta_i = \frac{1}{\sigma_{nom}} \sqrt{\frac{\sum_{i=1}^{N} (\sigma_i - \sigma_{mean})^2}{N-1}} \,, \tag{4.15}$$

where $N$ is the total number of variations of the measured cross section ($\sigma_i$), with respect to the mean value ($\sigma_{mean}$), and $\sigma_{nom}$ is the nominal cross section. The main sources of systematic errors associated with the cross section measurements in Sec. 4.4, and their estimation are discussed in this section.

### 4.5.1 Signal width and Mean

Alterations in the signal resonance shape could be introduced by the detector resolution and calibration effects. To account for this effect, variations in the signal shape are allowed around the nominal parameters. The $Y(2175)$ signal mean and width are allowed to vary around their nominal value by the PDG average errors, $\pm 0.01$ GeV/c$^2$ and $\pm 0.012$ GeV/c$^2$, respectively. The relative errors for the mean and width uncertainties are estimated and summarized in Tab. 4.26.

### 4.5.2 Background Polynomial Order

The background model described by the Chebyshev polynomial of degree $n$ as defined in Eq. 4.6, is varied around the nominal degree by $n$-1 and $n$+1 in order to estimate the uncertainty due to background parameterization. Similar variations are also allowed for the other background polynomials. The cross section measured

for every background order is then used as input to Eq. 4.15, and the resulting relative errors are listed in Tab. 4.15 - 4.25.

### 4.5.3 Fitting region

To study the impact of the fit window on the cross section measurement, the $\phi(1020)$, $f_0(980)$, and the $Y(2175)$ resonances fit regions are varied around their nominal range of [0.99, 1.2 GeV/c$^2$], [0.83, 1.14 GeV/c$^2$], and [2, 3 GeV/c$^2$], respectively. The $\phi(1020)$ fit range was varied to [0.99, 1.15 GeV/c$^2$] and [0.99, 1.25 GeV/c$^2$], the $f_0(980)$ was varied to [0.83, 1.12 GeV/c$^2$] and [0.83, 1.16 GeV/c$^2$], and finally the $Y(2175)$ fit range to [2.0, 2.9 GeV/c$^2$] and [2.0, 3.1 GeV/c$^2$]. The cross section is measured for each range, and the estimated relative errors are summarized in Tab. 4.15 - 4.25.

### 4.5.4 Finite binning

To study the impact of number of data point on the quality of the $\phi(1020)$ model fit, the number of bins in the $K^+K^-$ invariant mass are varied from the nominal value of 100, to 90 and 110 bins. The effect of these modifications on the nominal cross section is then estimated by Eq. 4.15, and summarized in Tab. 4.15 - 4.25.

### 4.5.5 Event Selection Variation

The variables with stronger effect on the event selection are varied around their nominal cut, to estimate the errors on the final measured cross section.

The accidental subtraction using four out-of-time beam bunches on each sides of the prompt beam bunch for the nominal cut is varied to two and one beam bunches. The symmetric timing cut used to select protons in the TOF detector is also varied from $\pm$0.3 ns to $\pm$0.2 and $\pm$0.4 ns. The $\chi^2$ of the kinematic fit as

well was varied from $\chi^2 < 55$ to $\chi^2 < 45$ and $\chi^2 < 65$. Finally, the missing mass squared symmetric cut was varied from $\pm 0.035$ to $\pm 0.025$ and $\pm 0.045$. The cross section is measured after every variation and the relative errors for each source is estimated and summarized in Tab. 4.15 - 4.25.

Finally, the above potential systematic errors, treated independently from each other, are added in quadrature to calculate the total systematic errors. The latter is quoted in the cross section measurements in Sec. 4.4. The individual systematic uncertainties for the non-resonant $\phi\pi^+\pi^-$ and $\phi f_0$ final states are reasonably small, and the total systematic uncertainties are comparable and in some cases smaller than the statistical ones. We conclude that the cross section measurements for the non-resonant channels are statistically limited and a collection of a larger data sample in the future will improve the measurements precision. However, the statistic and systematic uncertainties in the resonant modes $Y(2175) \to \phi\pi^+\pi^-$ and $Y(2175) \to \phi f_0$ are large, due to the multiple fluctuations around the $Y(2175)$ and a bigger sensitivity to the small parameter variations. Therefore, these measurements are considered statistically and systematically limited, and a carefully detailed analysis of a larger data sample is required to improve theses measurements.

Table 4.15: Summary of systematic uncertainties for the $\gamma p \to \phi\pi^+\pi^- p$ cross section measurements for the 2016 dataset in $E_\gamma$.

| $E_\gamma$ (GeV) | Bkg deg (%) | Fit range (%) | binning (%) | Accidental Subtraction (%) | Timing Cut (%) | Kinematic Fit $\chi^2$(%) | $MM^2$ (%) |
|---|---|---|---|---|---|---|---|
| 6.50 - 7.01 | 0.81 | 0.58 | 0.58 | 1.17 | 1.46 | 2.03 | 0.80 |
| 7.01 - 7.52 | 2.52 | 2.09 | 0.92 | 1.13 | 1.47 | 5.91 | 0.73 |
| 7.52 - 8.03 | 1.87 | 0.80 | 0.03 | 1.58 | 1.88 | 2.83 | 0.50 |
| 8.03 - 8.54 | 1.92 | 1.18 | 0.33 | 1.09 | 0.56 | 1.12 | 0.89 |
| 8.54 - 9.05 | 0.18 | 1.28 | 0.20 | 0.45 | 1.16 | 3.64 | 0.43 |
| 9.05 - 9.56 | 1.93 | 0.57 | 0.88 | 0.60 | 0.21 | 0.37 | 1.38 |
| 9.56 - 10.07 | 0.23 | 1.72 | 0.23 | 0.67 | 1.28 | 0.79 | 0.29 |
| 10.07 - 10.58 | 2.40 | 1.42 | 0.43 | 0.19 | 0.30 | 0.24 | 0.70 |
| 10.58 - 11.09 | 2.41 | 1.61 | 0.66 | 1.12 | 0.24 | 2.65 | 0.88 |
| 11.09 - 11.60 | 0.30 | 3.08 | 0.74 | 0.43 | 0.24 | 2.04 | 0.09 |

Table 4.16: Summary of systematic uncertainties for the $\gamma p \to \phi\pi^+\pi^- p$ cross section measurements for the 2016 dataset in -$t$.

| -$t$ $(GeV/c)^2$ | Bkg deg (%) | Fit range (%) | binning (%) | Accidental Subtraction (%) | Timing Cut (%) | Kinematic Fit $\chi^2$(%) | $MM^2$ (%) |
|---|---|---|---|---|---|---|---|
| 0.00 - 0.40 | 0.18 | 2.05 | 0.26 | 1.52 | 0.16 | 2.24 | 0.62 |
| 0.40 - 0.80 | 0.14 | 1.10 | 0.08 | 0.51 | 0.61 | 1.71 | 0.23 |
| 0.80 - 1.20 | 0.23 | 1.48 | 0.10 | 0.16 | 1.42 | 3.20 | 0.43 |
| 1.20 - 1.60 | 0.18 | 1.66 | 0.30 | 0.52 | 1.02 | 0.89 | 0.49 |
| 1.60 - 2.00 | 1.16 | 1.06 | 0.10 | 0.36 | 0.83 | 2.96 | 0.56 |
| 2.00 - 2.40 | 2.21 | 1.42 | 0.52 | 0.60 | 2.18 | 3.58 | 0.24 |
| 2.40 - 2.80 | 2.74 | 1.10 | 0.75 | 0.52 | 1.74 | 4.73 | 1.43 |
| 2.80 - 3.20 | 1.85 | 1.06 | 0.54 | 1.92 | 2.09 | 3.15 | 0.97 |
| 3.20 - 3.60 | 5.88 | 3.33 | 3.56 | 2.37 | 3.33 | 3.46 | 1.91 |
| 3.60 - 4.00 | 6.12 | 5.96 | 2.68 | 1.82 | 5.03 | 12.39 | 2.07 |

Table 4.17: Summary of systematic uncertainties for the $\gamma p \to \phi\pi^+\pi^- p$ cross section measurements for the 2017 dataset in $E_\gamma$.

| $E_\gamma$ (GeV) | Bkg deg (%) | Fit range (%) | binning (%) | Accidental Subtraction (%) | Timing Cut (%) | Kinematic Fit $\chi^2$(%) | $MM^2$ (%) |
|---|---|---|---|---|---|---|---|
| 6.50 - 7.01 | 0.17 | 0.83 | 0.38 | 0.80 | 1.33 | 1.69 | 0.30 |
| 7.01 - 7.52 | 0.13 | 0.96 | 0.02 | 0.28 | 1.26 | 1.41 | 0.22 |
| 7.52 - 8.03 | 0.25 | 1.31 | 0.17 | 0.15 | 1.20 | 2.43 | 0.33 |
| 8.03 - 8.54 | 0.11 | 1.13 | 0.06 | 0.52 | 1.25 | 2.62 | 0.44 |
| 8.54 - 9.05 | 0.09 | 0.98 | 0.25 | 0.43 | 1.13 | 1.79 | 0.17 |
| 9.05 - 9.56 | 0.32 | 1.23 | 0.08 | 0.55 | 0.85 | 2.63 | 0.40 |
| 9.56 - 10.07 | 0.14 | 1.78 | 0.10 | 0.52 | 0.83 | 1.84 | 0.70 |
| 10.07 - 10.58 | 0.09 | 1.65 | 0.03 | 0.18 | 0.92 | 2.40 | 0.59 |
| 10.58 - 11.09 | 0.35 | 2.25 | 0.32 | 0.55 | 0.92 | 0.79 | 0.45 |
| 11.09 - 11.60 | 0.12 | 1.99 | 0.39 | 0.57 | 1.38 | 0.62 | 0.21 |

Table 4.18: Summary of systematic uncertainties for the $\gamma p \to \phi\pi^+\pi^- p$ cross section measurements for the 2017 dataset in -$t$.

| -$t$ $(GeV/c)^2$ | Bkg deg (%) | Fit range (%) | binning (%) | Accidental Subtraction (%) | Timing Cut (%) | Kinematic Fit $\chi^2$(%) | $MM^2$ (%) |
|---|---|---|---|---|---|---|---|
| 0.00 - 0.40 | 0.26 | 2.06 | 0.18 | 0.10 | 0.23 | 0.76 | 0.71 |
| 0.40 - 0.80 | 0.11 | 1.03 | 0.02 | 0.30 | 0.96 | 1.59 | 0.04 |
| 0.80 - 1.20 | 0.09 | 1.12 | 0.10 | 0.12 | 1.25 | 2.70 | 0.09 |
| 1.20 - 1.60 | 0.23 | 1.12 | 0.27 | 0.26 | 1.05 | 3.76 | 0.28 |
| 1.60 - 2.00 | 0.31 | 1.66 | 0.10 | 0.22 | 1.65 | 3.96 | 0.46 |
| 2.00 - 2.40 | 0.33 | 0.82 | 0.25 | 0.45 | 2.12 | 4.84 | 0.32 |
| 2.40 - 2.80 | 0.81 | 1.02 | 0.32 | 0.08 | 2.75 | 2.28 | 1.22 |
| 2.80 - 3.20 | 1.77 | 2.12 | 0.49 | 0.87 | 2.05 | 5.01 | 1.54 |
| 3.20 - 3.60 | 1.11 | 0.89 | 0.37 | 0.79 | 4.85 | 5.73 | 1.20 |
| 3.60 - 4.00 | 1.90 | 1.20 | 0.71 | 1.30 | 2.62 | 4.71 | 2.32 |

Table 4.19: Summary of systematic uncertainties for the $\gamma p \to \phi\pi^+\pi^- p$ cross section measurements for the Spring 2018 dataset in $E_\gamma$.

| $E_\gamma$ (GeV) | Bkg deg (%) | Fit range (%) | binning (%) | Accidental Subtraction (%) | Timing Cut (%) | Kinematic Fit $\chi^2$(%) | $MM^2$ (%) |
|---|---|---|---|---|---|---|---|
| 6.50 - 7.01 | 0.19 | 0.61 | 0.28 | 0.14 | 0.92 | 1.76 | 0.14 |
| 7.01 - 7.52 | 0.17 | 0.81 | 0.34 | 0.57 | 0.76 | 0.95 | 0.22 |
| 7.52 - 8.03 | 0.18 | 0.75 | 0.08 | 0.24 | 0.88 | 1.10 | 0.32 |
| 8.03 - 8.54 | 0.31 | 0.97 | 0.20 | 0.52 | 0.81 | 1.85 | 0.16 |
| 8.54 - 9.05 | 0.22 | 0.53 | 0.18 | 0.60 | 0.76 | 2.16 | 0.17 |
| 9.05 - 9.56 | 0.19 | 0.73 | 0.09 | 0.10 | 0.78 | 2.62 | 0.10 |
| 9.56 - 10.07 | 0.37 | 1.36 | 0.09 | 0.10 | 0.66 | 2.43 | 0.47 |
| 10.07 - 10.58 | 0.37 | 1.48 | 0.11 | 0.54 | 0.70 | 3.48 | 0.21 |
| 10.58 - 11.09 | 0.30 | 1.49 | 0.12 | 0.06 | 0.58 | 4.21 | 0.04 |
| 11.09 - 11.60 | 0.47 | 2.30 | 0.16 | 0.28 | 0.59 | 3.09 | 0.21 |

Table 4.20: Summary of systematic uncertainties for the $\gamma p \to \phi\pi^+\pi^- p$ cross section measurements for the Spring 2018 dataset in -$t$.

| -$t$ $(GeV/c)^2$ | Bkg deg (%) | Fit range (%) | binning (%) | Accidental Subtraction (%) | Timing Cut (%) | Kinematic Fit $\chi^2$(%) | $MM^2$ (%) |
|---|---|---|---|---|---|---|---|
| 0.00 - 0.40 | 0.39 | 1.44 | 0.06 | 0.48 | 0.07 | 3.39 | 0.17 |
| 0.40 - 0.80 | 0.18 | 0.81 | 0.10 | 0.17 | 0.51 | 2.51 | 0.20 |
| 0.80 - 1.20 | 0.26 | 0.84 | 0.10 | 0.45 | 0.73 | 1.71 | 0.42 |
| 1.20 - 1.60 | 0.16 | 1.16 | 0.07 | 0.10 | 0.87 | 1.33 | 0.32 |
| 1.60 - 2.00 | 0.14 | 1.21 | 0.09 | 0.23 | 1.08 | 1.25 | 0.74 |
| 2.00 - 2.40 | 0.14 | 1.20 | 0.19 | 0.39 | 1.33 | 1.12 | 0.47 |
| 2.40 - 2.80 | 0.19 | 1.27 | 0.36 | 1.01 | 1.61 | 1.05 | 0.62 |
| 2.80 - 3.20 | 0.29 | 2.24 | 0.46 | 1.06 | 2.06 | 1.53 | 0.19 |
| 3.20 - 3.60 | 0.93 | 1.76 | 0.32 | 1.47 | 2.00 | 2.25 | 0.51 |
| 3.60 - 4.00 | 0.28 | 4.91 | 1.70 | 2.43 | 3.26 | 0.66 | 0.43 |

Table 4.21: Summary of systematic uncertainties for the $\gamma p \to \phi\pi^+\pi^- p$ cross section measurements for the Fall 2018 dataset in $E_\gamma$.

| $E_\gamma$ (GeV) | Bkg deg (%) | Fit range (%) | binning (%) | Accidental Subtraction (%) | Timing Cut (%) | Kinematic Fit $\chi^2$(%) | $MM^2$ (%) |
|---|---|---|---|---|---|---|---|
| 6.50 - 7.01 | 0.14 | 0.64 | 0.01 | 0.31 | 1.54 | 1.97 | 0.26 |
| 7.01 - 7.52 | 0.11 | 0.50 | 0.26 | 0.37 | 1.15 | 1.48 | 0.08 |
| 7.52 - 8.03 | 0.18 | 0.42 | 0.16 | 0.31 | 1.07 | 1.52 | 0.16 |
| 8.03 - 8.54 | 0.19 | 0.50 | 0.13 | 0.65 | 1.09 | 0.78 | 0.18 |
| 8.54 - 9.05 | 0.17 | 0.59 | 0.04 | 0.51 | 0.84 | 0.63 | 0.06 |
| 9.05 - 9.56 | 0.13 | 1.33 | 0.16 | 0.18 | 0.80 | 0.26 | 0.16 |
| 9.56 - 10.07 | 0.16 | 1.30 | 0.11 | 0.40 | 0.93 | 0.29 | 0.20 |
| 10.07 - 10.58 | 0.20 | 1.49 | 0.14 | 0.18 | 0.98 | 0.23 | 0.46 |
| 10.58 - 11.09 | 0.27 | 1.52 | 0.06 | 0.07 | 0.61 | 0.74 | 0.24 |
| 11.09 - 11.60 | 0.23 | 2.25 | 0.25 | 0.33 | 0.71 | 0.37 | 0.66 |

Table 4.22: Summary of systematic uncertainties for the $\gamma p \to \phi\pi^+\pi^- p$ cross section measurements for the Fall 2018 dataset in -$t$.

| -$t$ $(GeV/c)^2$ | Bkg deg (%) | Fit range (%) | binning (%) | Accidental Subtraction (%) | Timing Cut (%) | Kinematic Fit $\chi^2$(%) | $MM^2$ (%) |
|---|---|---|---|---|---|---|---|
| 0.00 - 0.40 | 0.25 | 1.83 | 0.13 | 0.25 | 0.14 | 1.45 | 0.35 |
| 0.40 - 0.80 | 0.17 | 0.55 | 0.08 | 0.40 | 0.66 | 0.09 | 0.13 |
| 0.80 - 1.20 | 0.15 | 0.58 | 0.05 | 0.33 | 0.77 | 1.05 | 0.08 |
| 1.20 - 1.60 | 0.13 | 0.59 | 0.04 | 0.13 | 0.98 | 1.28 | 0.08 |
| 1.60 - 2.00 | 0.16 | 0.56 | 0.04 | 0.21 | 1.05 | 1.39 | 0.02 |
| 2.00 - 2.40 | 0.08 | 1.17 | 0.04 | 0.34 | 1.45 | 2.08 | 0.34 |
| 2.40 - 2.80 | 0.12 | 0.50 | 0.09 | 0.13 | 1.56 | 1.89 | 0.46 |
| 2.80 - 3.20 | 0.14 | 1.52 | 0.14 | 0.04 | 2.25 | 2.93 | 0.25 |
| 3.20 - 3.60 | 0.21 | 1.86 | 0.34 | 0.44 | 2.58 | 3.70 | 0.51 |
| 3.60 - 4.00 | 0.15 | 1.73 | 0.64 | 1.40 | 3.31 | 3.55 | 0.47 |

Table 4.23: Summary of systematic uncertainties for the $\gamma p \to Y(2175)p \to \phi\pi^+\pi^- p$ cross section measurements.

| Dataset | Bkg deg (%) | Fit range (%) | binning (%) | Accidental Subtraction (%) | Timing Cut (%) | Kinematic Fit $\chi^2$(%) | $MM^2$ (%) |
|---|---|---|---|---|---|---|---|
| 2016 | 27.99 | 53.16 | 25.24 | 16.84 | 22.23 | 34.81 | 37.48 |
| 2017 | 25.38 | 21.20 | 9.89 | 17.07 | 3.28 | 4.55 | 5.21 |
| 2018 Spring | 47.24 | 31.86 | 49.63 | 7.03 | 18.17 | 30.22 | 5.86 |
| 2018 Fall | 53.79 | 71.75 | 5.67 | 7.51 | 26.80 | 55.23 | 82.87 |

Table 4.24: Summary of systematic uncertainties for the $\gamma p \to \phi f_0 p$ cross section measurements.

| Dataset | Bkg deg (%) | Fit range (%) | binning (%) | Accidental Subtraction (%) | Timing Cut (%) | Kinematic Fit $\chi^2$(%) | $MM^2$ (%) |
|---|---|---|---|---|---|---|---|
| 2016 | 7.86 | 5.59 | 0.96 | 2.16 | 4.17 | 3.46 | 4.70 |
| 2017 | 10.26 | 4.76 | 1.17 | 1.54 | 2.07 | 7.35 | 2.43 |
| 2018 Spring | 2.27 | 3.68 | 0.87 | 1.82 | 0.88 | 0.64 | 0.86 |
| 2018 Fall | 9.47 | 5.62 | 0.16 | 1.39 | 2.15 | 1.74 | 0.38 |

Table 4.25: Summary of systematic uncertainties for the $\gamma p \to Y(2175)p \to \phi f_0 p$ cross section measurements.

| Dataset | Bkg deg (%) | Fit range (%) | binning (%) | Accidental Subtraction (%) | Timing Cut (%) | Kinematic Fit $\chi^2$(%) | $MM^2$ (%) |
|---|---|---|---|---|---|---|---|
| 2016 | 534.68 | 169.65 | 560.01 | 162.14 | 219.87 | 227.61 | 80.38 |
| 2017 | 441.04 | 73.17 | 27.75 | 24.77 | 6.85 | 44.97 | 8.95 |
| 2018 Spring | 127.22 | 13.37 | 12.03 | 12.18 | 1.64 | 12.83 | 5.35 |
| 2018 Fall | 215.43 | 14.29 | 8.32 | 20.35 | 8.79 | 0.57 | 17.55 |

Table 4.26: Summary of systematic uncertainties on the cross section measurements due to resonance parameter variations.

| Dataset | $Y(2175) \to \phi\pi^+\pi^-$ | | $Y(2175) \to \phi f_0$ | |
|---|---|---|---|---|
| | $Y(2175)$ Mean (%) | $Y(2175)$ Width (%) | $Y(2175)$ Mean (%) | $Y(2175)$ Width (%) |
| 2016 | 4.68 | 12.86 | 32.16 | 31.58 |
| 2017 | 10.52 | 11.15 | 59.48 | 18.11 |
| 2018 Spring | 75.21 | 21.91 | 8.73 | 16.11 |
| 2018 Fall | 21.57 | 10.70 | 39.57 | 20.88 |

## 4.6 Conclusion

First preliminary measurements of the photoproduction cross section for exclusive $\phi(1020)\pi^+\pi^-$ and $\phi(1020)f_0(980)$ final states with the GlueX experiment for a photon beam energy range [6.5 - 11.6 GeV] are presented. The observed strong dependence of the $\phi\pi^+\pi^-$ cross section on the momentum transfer could be explained by the presence of intermediate sub-resonances, like the observed $\rho(770)$, or target fragmentation sources in the reaction, like $\Delta^{++} \to \pi^+ p$. These can lead to a different final state phase-space detector occupation, and given an asymmetric detector acceptance, this could be translated to different efficiencies and thus also cross section measurements.

In the absence of the $Y(2175)$ in the $\phi(1020)\pi^+\pi^-$ and $\phi(1020)f_0(980)$ channels, an upper limit on the measured cross section has been established. We obtain an upper limit at 90% CL of 0.67 nb, 0.24 nb, 0.20 nb and 0.35 nb for $Y(2175) \to \phi(1020)\pi^+\pi^-$, and 0.33 nb, 0.48 nb, 0.43 nb, and 0.39 nb for $Y(2175) \to \phi(1020)f_0($980, for the 2016, 2017, and Spring and Fall 2018 datasets, respectively. The non-observation of the $Y(2175)$ may be an indication for presence of other sources of background, such as *e.g.* $\Delta^{++}$ resonance in the reaction. The performed analysis is worth to be revisited with the improved PID capabilities and the higher statistics in GlueX Phase-II.

Detailed studies of the branching ratios of the $Y(2175)$ into different final states may then indicate the nature of this resonance. For instance, if the $\phi(1020)f_0(980)$ decay mode is the dominant one, then the tetraquark picture is favored, with the $Y(2175)$ as an $ss\overline{ss}$, $s\bar{s}s\bar{s}$ or $su\overline{su}$ depending on the structure considered for the $f_0(980)$.

# Chapter 5

# Summary and Outlook

The first phase of the GlueX experiment was completed successfully at the end of 2019, with more than 121 $pb^{-1}$ of data collected in the coherent photon beam region. Using the calibrated data sets, a search for the hybrid meson candidate, the $Y(2175)$, in both, the $\phi\pi^+\pi^-$ and the $\phi(1020)f_0(980)$ exclusive final states has been performed. A first measurement of the photoproduction cross section for both channels has been carried out, and an upper limit on the production cross section of the $Y(2175)$ has been determined for both, $\phi\pi^+\pi^-$ and $\phi(1020)f_0(980)$ final states.

For a better estimation of the energy loss in the CDC, an optimization of the truncated mean method was conducted, and a 20% hit-truncation at the high tale of the dE/dx distribution was concluded, which is meanwhile officially included in the GlueX reconstruction software.

The next phase of the GlueX program will start soon, with an additional detector system for Detection of Internally Reflected Cherenkov light (DIRC), currently being installed and commissioned. This upgrade will improve the particle identification system (Fig. 5.1), in order to cleanly select meson and baryon decay channels that include kaons in the final state. Once this detector has been installed

and commissioned, the plan is to collect a total of 200 days of physics analysis data at an average intensity of 5x$10^7/s$ tagged photons on target. This data sample will provide an order of magnitude statistical improvement over the initial GlueX data set. Together with the developed kaon identification system, the GlueX potential for contributing to the understanding of hybrid mesons, in particular on the nature of the $Y(2175)$, will significantly increase in the near future. It will be worth to repeat the analysis proposed, developed, and carried out as described in this thesis.

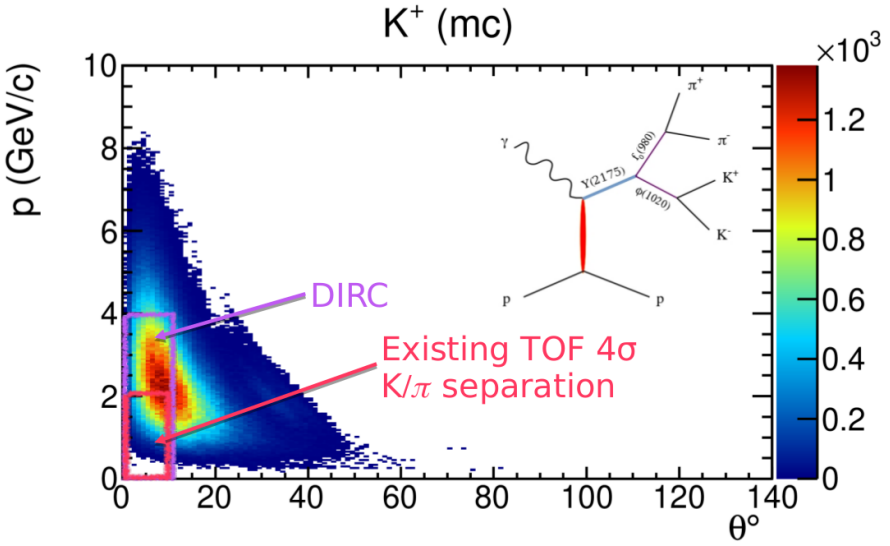


Figure 5.1: Kaon momentum versus the polar angle in MC, with kaon from the $\gamma p \to Y(2175)p \to \phi f_0 \to K^+K^-\pi^+\pi^-p$ reaction. The boxes show the TOF (red) and DIRC (purple) coverages.

# Chapter 6

# Zusammenfassung

Unser Verständnis der grundlegenden Bausteine der Materie hat in den letzten Jahrzehnten große Fortschritte gemacht. Vor fast einem halben Jahrhundert wurde die Quantenchromodynamik (QCD) entwickelt, eine revolutionäre Idee, dass Protonen, Neutronen und alle anderen stark wechselwirkenden Teilchen, die so genannten Hadronen, aus Quarks bestehen, die über den Austausch von Gluonen miteinander wechselwirken. Im Laufe der Jahre hat sich dieser Vorschlag fest etabliert, auch wenn wir freie Quarks aufgrund des Phänomens des Confinement nicht direkt beobachten konnten. Trotz jahrzehntelanger Forschung fehlt uns immer noch ein detailliertes quantitatives Verständnis der Art und Weise, wie die QCD das Spektrum der Hadronen erzeugt. Eine breit angelegte experimentelle Forschungskampagne wird durchgeführt, um ein neues Licht auf das Hadronen-Anregungsspektrum und die Dynamik von Hadronen zu werfen und dabei zu helfen, die theoretischen Modelle zu verbessern und zu testen. Ein wichtiger Akteur bei der Untersuchung dieser Eigenschaften ist das GlueX-Experiment, das darauf abzielt, die Eigenschaften des Beitrags des Gluonischen Feldes zu den Quantenzahlen des Quark-Antiquark gebundenen Systems, den hybriden Mesonen, zu entdecken und zu untersuchen.

Mesonen im Konstituentenquarkmodell sind farbsingletgebundene Zustände eines Quarks $q$ und eines Antiquarks $\overline{q}$, mit den Quantenzahlen $J^{PC} = 0^{-+}, 0^{++}, 1^{--}, 1^{+-}, 1^{++}, 2^{--}, 2^{-+}, 2^{++}, usw$, wobei $J$, $P$ und $C$ die Gesamtdrehimpuls-, Paritäts- bzw. Ladungskonjugation des Fermionensystems sind. Dieses einfache Bild hat erfolgreich viele beobachtete Zustände im Mesonenspektrum beschrieben. Die QCD lässt jedoch ein reichhaltigeres Spektrum zu, das die gluonischen Freiheitsgrade im Quark und Anti-Quark-System einschließt. Da das gluonische Feld verschiedene Quantenzahlen tragen kann, führt dies viele neue Zustände in das Spektrum ein, einschließlich solcher, die Quantenzahlen tragen: $J^{PC} = 0^{--}, 0^{+-}, 1^{-+}, 2^{+-}, usw$, die für konventionelle $q\overline{q}$-Mesonen nicht erlaubt sind. Letztere sind die (Spin-)exotischen Hybridmesonen, und ihre experimentelle Beobachtung wird ein Beweis für die Existenz solcher Zustände jenseits des Konstituentenquarkmodells sein. Die hybriden Mesonen werden von vielen phänomenologischen Modellen vorhergesagt, wobei die Gitter-QCD Vorhersagen für ihre Eigenschaften wie die Masse macht, die experimentell getestet werden kann.

Das GlueX-Experiment ist der Abbildung des Spektrums hybrider Mesonen gewidmet, wobei ein hochenergetischer, linear polarisierter Photonenstrahl verwendet wird, der von einem 12 GeV-Elektronenstrahl durch kohärente Bremsstrahlung auf einem Diamantstrahler erzeugt wird. Durch die Wahl der Kristallachsenorientierung des Diamanten erzeugten wir vier Datensätze mit 2 Sätzen paralleler (0°/90°) bzw. senkrechter (45°/135°) Polarisationsorientierungen. Die Energie und Intensität des Photonenstrahls werden mit einem Paar-Spektrometersystem (Dipolmagnet- und Szintillator-Arrays) überwacht, und zur Messung der Polarisation wird ein Triplett-Polarimeter ($\gamma e^- \to e^+e^-e^+$ Streuung an einer dünnen Be-Folie) verwendet. Der Photonenstrahl trifft auf ein 30 cm langes Flüssigwasserstoff-Target, das entlang der Mittelachse des Detektors positioniert ist (siehe Abb. 2.5). Der

zentrale Bereich des Detektors befindet sich in einem Solenoidmagneten mit einer Magnetfeldstärke von $\sim$ 2T auf seiner Mittelachse. Teilchen aus der primären Wechselwirkung durchlaufen zunächst den Startzähler (Szintillator-Detektor), mit dessen Hilfe der Strahlbecher, der das Ereignis erzeugt hat, identifiziert werden kann. Unmittelbar um den Startzähler herum befindet sich die zentrale Driftkammer (CDC) (Strohhalm Detektor), die Informationen zur Verfolgung und zum Energieverlust ($dE/dx$) liefert. Der CDC nachgeschaltet sind die vier Pakete der Forward Drift Chamber (FDC) (planare Driftkammern), die sowohl die Verfolgung als auch die $dE/dx$-Informationen liefern. Um die Spurdetektor herum befindet sich das Barrel Calorimeter (BCAL) (Bleiszintillatorfaser), das für Photonen zwischen Polarwinkeln von 11° und 126° empfindlich ist. Hinter der Magnetspule befindet sich das Forward Calorimeter (FCAL) (Blei-Glasblöcke), das Polarwinkel von 1° bis 11° abdeckt. Vor dem FCAL befindet sich die Time Of Flight-Wand (TOF) (Szintillatorbalken), die Zeitinformationen liefert.

Die erste Phase des GlueX-Experiments wurde Ende 2019 erfolgreich abgeschlossen, wobei im Bereich des kohärenten Photonenstrahls mehr als 121 $\mathrm{pb}^{-1}$ an Daten gesammelt wurden. Unter Verwendung der kalibrierten Datensätze wurde eine Suche nach dem $1^{--}$ Hybrid-Mesonenkandidaten, dem $Y(2175)$, sowohl in den $\phi\pi^+\pi^-$ als auch in den $\phi(1020)f_0(980)$ exklusiven Endzuständen durchgeführt. Ein mögliches Strangeonium-Pendant des $Y(4260)$ im Charmonium-Sektor, das bereits bei Positron-Elektronen-Experimenten beobachtet wurde. Trotz aller bisherigen experimentellen Bemühungen reicht unser Wissen über den $Y(2175)$ nicht aus, um eine der theoretischen Interpretationen zu bestätigen oder zu unterdrücken. Bis jetzt beschränken sich alle experimentellen Informationen über den $Y(2175)$ auf die $\mathrm{e}^+\mathrm{e}^-$ Vernichtung und den $J/\psi$ hadronischen Zerfall. Die $Y(2175)$-Produktion in anderen Prozessen wird zum Verständnis seiner Natur beitragen. Das GlueX-Experiment bietet eine neue Möglichkeit, diesen Zustand

zum ersten Mal in der Fotoproduktion zu suchen. Da der $Y(2175)$ in den Zuständen $\phi(1020)f_0(980)$ und $\phi(1020)\pi^+\pi^-$ gesehen wird, haben wir die exklusive Reaktion $\gamma p \to p\pi^+\pi^-K^+K^-$ untersucht. Die Rekonstruktion der Teilchen im Endzustand ist für die physikalische Analyse mit einer guten Kaon-, Pion- und Protonentrennung unerlässlich. Eines der entscheidenden GlueX-Spektrometer-Subsysteme für die Bereitstellung der PID-Informationen ist der CDC-Detektor durch die Messung des Energieverlustes, $dE/dx$. Für eine bessere Abschätzung des mittleren Energieverlustes im CDC wurde eine optimale Trunkierung des durchschnittlichen $dE/dx$ für Pionen und Protonen untersucht. Der Anteil der zurückzuweisenden Treffer wird durch die Optimierung von drei Gütezahlen bestimmt: die mittlere Energieverlustauflösung sowohl für Protonen als auch für Pionen, die Trennschärfe zwischen den Teilchenarten und die Fehlidentifizierungsfraktion (mis-PID) zwischen den Teilchen. Der Fehlidentifikationsanteil (mis-PID) ist der Anteil der Treffer aller rekonstruierten Spuren in der $dE/dx$-Verteilung, der zwischen den Partikelspezies gemischt wird. Durch die Optimierung des mis-PID, der Trennleistung und der $dE/dx$-Auflösung wird eine optimale Trunkierung erreicht, die auf $\sim$ 20% auf die hohen $dE/dx$-Werte geschätzt wird und inzwischen offiziell in der Rekonstruktionssoftware GlueX enthalten ist.

Um nach $Y(2175)$ in den Zerfallsmodi $\phi\pi^+\pi^-$ und $\phi f_0(980)$, mit $\phi \to K^+K^-$ und $f_0 \to \pi^+\pi^-$ zu suchen, haben wir die Reaktionen der Form $\gamma p \to K^+K^-\pi^+\pi^-p$ untersucht. Ein Ereignisauswahlverfahren wird angewandt, um die Hintergrundereignisse, die unser Signal nachahmen, so weit wie möglich zu subtrahieren und die Signalereignisse so weit wie möglich beizubehalten. Dies wird durch Schnitte auf verschiedene Variablen gefolgt von der Auswahl der exklusiven $\phi\pi^+\pi^-$-Ereignisse realisiert, da das $\phi f_0(980)$ eine Unterstichprobe des $\phi\pi^+\pi^-$ ist. Um den Untergrund unter dem $\phi(1020)$ in der $K^+K^-$-invarianten Masse zu entfernen, fügen wir ein $\phi(1020)$-Signal plus Untergrund in Abhängigkeit von den $\pi^+\pi^-$

und $K^+K^-\pi^+\pi^+\pi^-$-invarianten Massen ein und extrahieren auf diese Weise die massenabhängigen $\pi^+\pi^-$ und $K^+K^-\pi^+\pi^-$ invarianten $\phi(1020)$ Einträge. Eine erste Messung des Fotoproduktionsquerschnitts für die Kanäle $\phi\pi^+\pi^-\pi^-$ und $\phi(1020)f_0(980)$ wurde durchgeführt. Da die $Y(2175)$ in beiden Kanälen nicht gefunden wurden, wurde eine Obergrenze für den gemessenen Querschnitt festgelegt. Wir erhalten eine Obergrenze bei 90% CL von 0,67 nb, 0,24 nb, 0,20 nb und 0,35 nb für $Y(2175) \rightarrow \phi(1020)\pi^+\pi^-$, und 0,33 nb, 0. 48 nb, 0,43 nb und 0,39 nb für $Y(2175) \rightarrow \phi(1020)f_0(980$, für die Datensätze 2016, 2017 sowie Frühjahr und Herbst 2018. Darüber hinaus werden die potenziellen Quellen systematischer Fehler durch mehrere Variationen in der Analysekette geschätzt und in quadratisch zu den Gesamtfehlern bei den Querschnittsmessungen addiert.

Die nächste Phase des GlueX-Programms beginnt in Kürze mit einem zusätzlichen Detektorsystem, dem DIRC (detection of internally reflected Cherenkov radiation), das derzeit installiert und in Betrieb genommen wird. Dieses Upgrade wird die Teilchen-Identifikation (Abb. 5.1) verbessern, um Mesonen- und Baryon-Zerfallskanäle, die im Endzustand Kaonen enthalten, sauber zu identifizieren.

Sobald dieser Detektor installiert und in Betrieb genommen worden ist, folgt eine geplante Datennahme von 200 Tagen mit einer durchschnittlichen Intensität von $5\text{x}10^7/s$ Photonen, welches einer statistischen Verbesserung um eine Größenordnung gegenüber dem ursprünglichen GlueX-Datensatz entspricht. Damit sowie mit dem neu entwickelten Kaon-Identifikationssystem wird eine signifikante Steigerung des Potentials von GlueX erzielt, um in naher Zukunft entscheidend zu unserem Wissen über hybride Mesonen beizutragen. Die in dieser Arbeit beschriebene, entwickelte und durchgeführte Suche sowie Messungen sollten basierend auf den Daten der GlueX Phase-II wiederholt werden.

# Bibliography


[1] M. Gell-Mann H. Fritzsch and H. Leutwyler. "Advantages of the Color Octet Gluon Picture". *Phys. Lett.* 47 B (1973), p. 365.

[2] M. Gell-Mann. "A Schematic Model of Baryons and Mesons". *Phys.Lett.* 8 (1964), pp. 214–215.

[3] M. Gell-Mann. "Symmetries of baryons and mesons". *Phys.Rev.* 125 (1962), p. 1067.

[4] Y.Ne'eman. "Derivation of strong interactions from a gauge invariance". *Nucl.Phys.* 26 (1961), p. 1067.

[5] G. Zweig. "An $SU(3)$ model for strong interaction symmetry and its breaking". *CERN Preprint 8182/Th.* (1964).

[6] D. J. Gross. "The discovery of asymptotic freedom and the emergence of QCD". *Rev. Mod. Phys.* 77 (2005), p. 837.

[7] F. Wilczek. "Asymptotic freedom: From paradox to paradigm". *Rev. Mod. Phys.* 77 (2005), p. 857.

[8] M. Tanabashi et al. (Particle Data Group). "Review of Particle Physics". *Phys. Rev.* D 98 (2018), p. 030001.

[9] C. A. Meyer and E. S. Swanson. "Hybrid Mesons". *Progress in Particle and Nuclear Physics* B 82 (2015), p. 21.

[10] Mu-Lin Yann Gui-Jun Ding. "A candidate for $1^{--}$ strangeonium hybrid". *Phys. Lett.* B 650 (2007), p. 390.

[11] J. J. Dudek et al. "Toward the excited isoscalar meson spectrum from lattice QCD". *Phys. Rev.* 88 (2013), p. 094505.

[12] R. Kokoski N. Isgur and J. Paton. "Gluonic excitations of mesons: Why they are missing and where to find them". *Phys. Rev. Lett.* 54 (1985), p. 869.

[13] M. Swat. A. P. Szczepaniak. "Role of Photoproduction in Exotic Meson Searches". *Phys.Lett.* B 516 (2001), p. 72.

[14] D. R. Yennie T. H. Bauer R. D. Spital and F. M. Pipkin. "The hadronic properties of the photon in high-energy interactions". *Rev. Mod.Phys.* 50 (1978), p. 261.

[15] H. Al Ghoul et al. (GlueX Collaboration). "Measurement of the beam asymmetry $\Sigma$ for $\pi^0$ and $\eta$ photoproduction on the proton at $E_\gamma = 9$ GeV". *Phys.Rev.* C 95 (2017), 042201(R).

[16] B. Aubert et al. (BaBar Collaboration). "Structure at 2175 MeV in $e^+e^- \to \phi f_0(980)$ observed via initial-state radiation". *Phys. Rev.* D 74 (2006), 091103(R).

[17] B. Aubert et al. (BaBar Collaboration). "Cross sections for the reactions $e^+e^- \to K^+K^-\pi^+\pi^-$, $K^+K^-\pi^0\pi^0$ and $K^+K^-K^+K^-$ measured using initial-state radiation events". *Phys. Rev.* D 86 (2012), p. 012008.

[18] C. P. Shen et al. (Belle). "Observation of the $\phi(1680)$ and the $Y(2175)$ in $e^+e^- \to \phi\pi^+\pi^-$". *Phys. Rev.* D 80 (2009), p. 031101.

[19] M. Ablikim et al. (BES). "Observation of $Y(2175)$ in $e^+e^- \to \eta\phi f_0(980)$". *Phys. Rev. Lett.* 100 (2008), p. 102003.

[20] M. Ablikim et al. (BESIII). "Study of $J/\psi \to \eta\phi\pi^+\pi^-$". *Phys. Rev.* D 91 (2015), p. 052017.

[21] M. Ablikim et al. (BESIII). "Observation of $e^+e^- \to \eta Y(2175)$ at center-of-mass energies above 3.7 GeV". *Phys. Rev.* D 99 (2019), p. 012014.

[22] H. X. Chen et al. "$Y(2175)$ state in the QCD sum rule". *Phys. Rev.* D 78 (2008), p. 034012.

[23] E. Klempt and A. Zaitsev. "Glueballs, hybrids, multiquarks: Experimental facts versus QCD inspired concepts". *Phys. Rept.* 454 (2007), p. 1.

[24] G. Rupp S. Coito and E. van Beveren. "Multichannel calculation of excited vector $\phi$ resonances and the $\phi(2170)$". *Phys.Rev.* D 80 (2009), p. 094011.

[25] J.M. Alarcon L. Alvarez-Ruso J.A. Oller. "$\phi(1020)f_0(980)$ $S$-wave scattering and the $Y(2175)$ resonance". *Phys.Rev.* D 80 (2009), p. 054011.

[26] S. Godfrey and N. Isgur. "Mesons in a relativized quark model with chromodynamics". *Phys.Rev.* D 32 (1985), p. 189.

[27] T. Barnes et al. "Higher quarkonia". *Phys.Rev.* D 55 (1997), p. 4157.

[28] N. Black T. Barnes and P. R. Page. "Strong decays of strange quarkonia". *Phys.Rev.* D 68 (2003), p. 054014.

[29] M.-L. Yan G.-J. Ding. "$Y(2175)$: Distinguish Hybrid State from Higher Quarkonium". *Phys.Rev.* B 657 (2007), p. 49.

[30] Charles E. Reece. "Continuous wave superconducting radio frequency electron linac for nuclear physics research". *Phys. Rev. Accel.* Beams 19 (2016), p. 124801.

[31] The GlueX Collaboration. *Hall D / GlueX Technical Design Report* (1997).

[32] M. Dugger et al. "Design and construction of a high-energy photon polarimeter". *Nucl.Instrum.Meth.* A 867 (2017), p. 115.

[33] H. Al Ghoul et al (The GlueX Collaboration). "First Results from The GlueX Experiment". *AIP Conf. Proc.* 1735 (2016), p. 020001.

[34] Y. Van Haarlem et al. (The GlueX Collaboration). "The Central Drift Chamber for GlueX". *Nucl. Instrum. Meth.* A 662 (2010), p. 142.

[35] N. S. Jarvis et al. "The Central Drift Chamber for GlueX". *Nucl. Instrum. Meth.* 962 (2020), p. 163727.

[36] W. R. Leo. "Techniques for Nuclear and Particle Physics Experiments: A How-to Approach". *Second Revised Edition, Springer-Verlag* (1994), p. 24.

[37] W. Riegler Wa. Blum and L. Rolandi. "Particle Detection with Drift Chambers". *Springer-Verlag* (2008), p. 331.

[38] Xue-Xiang Cao et al. "Studies of dE/dx measurements with the BESIII". *Chin.Phys.* C 34 (2010), p. 1852.

[39] M. Hauschild. "Progress in $dE/dx$ techniques used for particle identification". *Nucl. Instrum. Meth.* A 379 (1996), p. 436.

[40] J. Ballam et al. "$\gamma - p$ Total Hadronic Cross Sections at 7.5 GeV". *Phys. Rev. Lett.* 21 (1968), p. 1544.

[41] H. Meyer et al. "Total cross section for photoproduction of hadrons on hydrogen and deuterium between 1.0 and 6.4 GeV". *Phys. Lett.* B 33 (1970), pp. 189–192.

[42] J. J. Xie E. Wang and J. Nieves. "Regge signatures from CLAS $\Lambda(1520)$ photoproduction data at forward angles". *Phys. Rev.* C 90 (2014), p. 065203.

[43] Y. Y. Wang et al. "Study on the reaction of $\gamma p \to f1(1285)p$ in Regge-effective Lagrangian approach". *Phys. Rev.* D 95 (2017), p. 096015.

[44] T. Mibe et al. [LEPS Collaboration]. "Diffractive $\phi$-meson photoproduction on proton near threshold". *Phys. Rev. Lett.* 95 (2005), p. 182001.

[45] D. Aston et al. “Evidence for a High Mass Enhancement in $K^+K^-$ Photoproduction”. *Phys. Lett.* B 104 (1981), p. 231.

[46] Glen Cowan et al. “Asymptotic formulae for likelihood-based tests of new physics”. *Eur. Phys. J. C* 71 (2011), p. 1554.

[47] S.S. Wilks. “The large-sample distribution of the likelihood ratio for testing composite hypotheses”. *Ann. Math. Stat.* 9 (1938), pp. 60–62.